

**PHOTOPRODUCTION OF $\Phi(1020)$
MESON IN NEUTRAL DECAY MODE**
 $\gamma p \rightarrow \phi p \rightarrow p K_S K_L$

by

Heghine Seraydaryan

August 10, 2010

TABLE OF CONTENTS

	Page
List of Tables	iv
List of Figures	viii
 CHAPTERS	
1 Introduction	1
2 Theory	4
2.1 Introduction to Theory	4
2.2 Kinematical Variables	6
2.3 The diffractive amplitudes	10
2.3.1 Pomeron exchange amplitudes	10
2.3.2 Pseudoscalar meson exchange amplitudes	13
2.3.3 f'_2 meson and glueball exchange	14
2.4 Baryon and baryon resonance exchange	15
2.4.1 Baryon resonance exchange	15
2.4.2 Direct ϕ meson Radiation	15
2.5 Theoretical results and expectations	16
2.5.1 Unpolarised cross section	16
2.5.2 Spin observables	18
2.6 Summary	21
3 Data Analysis	22
3.1 Data selection	24
3.2 Energy and Momentum Corrections	24
3.2.1 Tagger Energy Corrections	24
3.2.2 Energy Loss Correction	28
3.2.3 Momentum Corrections	28
3.3 Detector Efficiency Corrections	33
3.4 Fiducial Cuts	38
3.5 Vertex Cut	42
3.6 Particle Identification	42
3.7 Background Separation	48
3.8 Acceptance Correction and Normalization	49
3.8.1 Monte Carlo generator	49
3.8.2 Acceptance	50
3.8.3 Energy Loss Momentum Corrections (for Monte Carlo)	52
3.8.4 Target Density	65
3.8.5 Normalization to Flux	65
4 Physics Results	68
4.1 Differential Cross Sections	68

4.2	Angular Distribution Functions and Spin Observables	74
4.3	Systematic Uncertainties	78
4.4	Summary	84

LIST OF TABLES

	Page
I	Removed dead scintillator paddles.
II	Coefficients for energy loss momentum corrections for MC.
III	The parameter values, used to calculate liquid hydrogen target density [46].
IV	Summary of systematic errors.

LIST OF FIGURES

	Page
1 Experimental results for the energy dependence of $(d\sigma/dt)_{t=- t _{min}}$ measured by different collaborations [2].	2
2 Phase-space overlap of $\phi(1020)$ meson and $\Lambda(1520)$ baryon [11]. . . .	2
3 Feynman diagrams of two γp processes producing the same K^+K^-p final state: via the ϕ resonance (left) and via the Λ resonance (right). . . .	3
4 Diagrams of ϕ meson production mechanisms by A.I. Titov [12]	5
5 The schematic pictures of the $\gamma N \rightarrow \phi N \rightarrow K_SK_L$ reaction in c.m.s. .	6
6 Diagrammatic representation of GJ, H and A reference systems in ϕ meson rest frame.	7
7 Pomeron exchange models for ϕ meson production: (a) VDM model, (b) DL model [12].	10
8 Two gluon exchange mechanism for vector meson photoproduction [13]. .	12
9 The total cross section as a function of photon energy: (a) modeels A,B and C indicated by dashed, long-dashed and dot-dashed curves, (b) hybrid model [13].	17
10 (a) The differential cross section as a function of $-t$ at $E_\gamma = 2.2$ GeV for PS exchange (long-dashed), diffractive channels (dot-dashed), resonance excitation (dashed) and the total amplitude (solid). (b) The differential cross section as a function of ϕ production angle at $E_\gamma = 1.7, 2.0$ and 3.6 GeV. The data are from [35, 36]. [13].	18
11 The spin-density matrix elements as a function of $-t$ at $E_\gamma = 2.2$ GeV: (a) for the Pomeron exchange amplitude, (b) for the full model [13]. .	19
12 Angular distribution function at $E_\gamma = 2.2$ GeV and $ t =0.2, 0.5$ and 1.8 GeV^2 as a function of: (a) $\cos \Theta$, (b) Φ . [13]	20
13 Spin-density matrix elements as a function of E_γ at $ t =0.4$ GeV^2 for: (a) Pomeron exchange amplitude, (b) full model. [13]	21
14 Integrated Luminosity of the g11 experiment.	22
15 (a) The missing mass shift in the reaction $\gamma p \rightarrow K^+K^-X$, $\Delta M = M_X - M_{proton}$, (b) Beam energy correction factor $R = E_{corrected}/E_\gamma$ as a function of run number. [40]	25
16 Tagger energy correction $R = E_\gamma/E_{\gamma 0}$ as a function of tagger ID. [40]	26
17 The difference of the missing mass of the reaction $\gamma p \rightarrow \pi^+\pi^-X$ and proton mass $\Delta M = M_X - M_p$ as a function of tagger ID after the tagger energy correction. [40]	27
18 Momentum corrections for positive particles (π^+, K^+ , protons) $R = P_{corrected}/P_{measured} - 1$ estimated from the missing mass distributions in: (a,b,c) $\gamma p \rightarrow \pi^+\pi^-p$, (d) for the protons from the reaction $\gamma p \rightarrow K^+K^-p$. [40]	29

19	Momentum corrections for negative particles (π^-, K^-) $R = P_{corrected}/P_{measured} - 1$ [40]	30
20	The mass distributions of missed protons before and after the corrections were applied in two reactions:(a) $\gamma p \rightarrow \pi^+ \pi^- X$, (b) $\gamma p \rightarrow K^+ K^- X$. [40]	31
21	Invariant and missing masses after all corrections were applied. [40]	32
22	The calculation of efficiency coefficients for the protons. (a) The missing protons θ angle vs ϕ angle; (b) The detected protons θ angle vs ϕ ; (c) The 3D plots of efficiency coefficients for the protons plotted versus θ and ϕ angles in different momentum ranges.	35
23	The calculation of efficiency coefficients for the positive pions. (a) The missing π^+ θ angle vs ϕ angle; (b) The detected π^+ θ angle vs ϕ ; (c) The 3D plots of efficiency coefficients for the positive pions plotted versus θ and ϕ angles in different momentum ranges.	36
24	The calculation of efficiency coefficients for the negative pions. (a) The missing π^- θ angle vs ϕ angle; (b) The detected π^- θ angle vs ϕ ; (c) The 3D plots of efficiency coefficients for the negative pions plotted versus θ and ϕ angles in different momentum ranges.	37
25	Proton angular distributions:(a),(b) before efficiency corrections, (c),(d) after efficiency corrections.	39
26	π^+ meson angular distributions:(a),(b) before efficiency corrections, (c),(d) after efficiency corrections.	40
27	π^- meson angular distributions:(a),(b) before efficiency corrections, (c),(d) after efficiency corrections.	41
28	Invariant mass of $\pi^+ \pi^-$ system with a cut on mass of missing K_L from $\gamma p \rightarrow p\pi^+ \pi^- (X)$ reaction: $\Delta M(K_L) = 30 MeV/c^2$	43
29	Missing mass of $\gamma p \rightarrow p\pi^+ \pi^- (X)$ reaction, with a cut on invariant mass of $\pi^+ \pi^-$: $M(\pi^+ \pi^-) < 0.015 GeV/c^2$	44
30	Missing mass of $\gamma p \rightarrow p\pi^+ \pi^- (X)$ reaction in $0.45-0.55 GeV/c^2$ range, with cuts: $\Delta M(K_S) = 16 MeV/c^2$ and $M(K_S K_L) < 1.07 GeV/c^2$	45
31	Invariant mass of $K_S K_L$ with very broad cuts: $\Delta M(K_S) = 70 MeV/c^2$ and $\Delta M(K_L) = 200 MeV/c^2$	46
32	Invariant mass of $K_S K_L$ with cuts: $\Delta M(K_S) = 16 MeV/c^2$ and $\Delta M(K_L) = 30 MeV/c^2$	47
33	50
34	Calculated acceptances for different $t - t_{min}$ bins and different photon energy regions.	53
35	Calculated acceptances for different $t - t_{min}$ bins and different photon energy regions.	54
36	Calculated acceptances for different $\cos\Theta$ bins in Helicity frame and different photon energy regions.	55

37	Calculated acceptances for different $\cos\Theta$ bins in Helicity frame and different photon energy regions.	56
38	Calculated acceptances for different $\cos\Theta$ bins in Gottfried-Jackson frame and different photon energy regions.	57
39	Calculated acceptances for different $\cos\Theta$ bins in Gottfried-Jackson frame and different photon energy regions.	58
40	Calculated acceptances for different azimuthal angle Φ bins in Helicity frame and different photon energy regions.	59
41	Calculated acceptances for different azimuthal angle Φ bins in Gottfried-Jackson frame and different photon energy regions.	60
42	$\frac{P_g - P_r}{P_r}$ versus P_r histograms for protons, π^+ and π^- mesons. (a),(b) and (c) histograms correspond to momenta dependencies before the corrections. (d),(e) and (f) are the histograms after applying the momentum corrections.	61
43	Fits for protons' $P_g - P_r/P_r$ distributions in different P_r intervals by Gaussian function.	62
44	Fits for π^+ mesons' $P_g - P_r/P_r$ distributions in different P_r intervals by Gaussian function.	63
45	Fits for π^- mesons' $P_g - P_r/P_r$ distributions in different P_r intervals by Gaussian function	64
46	Photon flux as a function of photon beam energy.	67
47	The $ t - t_{min} $ dependence of the ϕ meson differential cross section $d\sigma/dt$ in different photon beam energy bins of 1.6-3.6 GeV energy range.	70
48	The $\cos\theta_{c.m.}^\phi$ dependence of the ϕ meson differential cross section $d\sigma/d\cos\theta_{c.m.}$ for different photon beam energy bins of 1.6-3.6 GeV energy range.	71
49	The \sqrt{s} dependence of the ϕ meson differential cross section $d\sigma/dt$ in different $\cos\theta_{c.m.}$ bins for $-0.55 < \cos\theta_{c.m.} < 0.25$ range.	72
50	The \sqrt{s} dependence of the ϕ meson differential cross section $d\sigma/dt$ in different $\cos\theta_{c.m.}$ bins for $0.25 < \cos\theta_{c.m.} < 0.95$ range.	73
51	Differential cross section $d\sigma/dt$ at $t = t_{min}$ (a) and ϕ meson photoproduction slope β (b) for the Neutral decay channel plotted as functions of photon beam energy E_γ in 1.6-3.6 GeV energy range. The error bars represent the statistical errors, errors of the flux calculation, efficiency error at 40% efficiency cut, acceptance errors. The systematic errors are included as dashed pink regions at horizontal axis.	75
52	The decay distribution of ϕ meson as a function of polar angle Θ in Helicity frame for the 'neutral' decay channel of $\phi(1020)$ meson.	76
53	The decay distribution of ϕ meson as a function of polar angle Θ in Gottfried-Jackson frame for the 'neutral' decay channel of $\phi(1020)$ meson.	77

54	The decay distribution of ϕ meson as a function of azimuthal angle Φ in Helicity frame for the 'neutral' decay channel of $\phi(1020)$ meson.	79
55	The decay distribution of ϕ meson as a function of azimuthal angle Φ in Gottfried-Jackson frame for the 'neutral' decay channel of $\phi(1020)$ meson.	80
56	Spin-density matrix element components ρ_{00}^0 (blue) and ρ_{1-1}^0 (red) for different photon beam energies in 1.6-3.6 GeV range in Helicity frame.	81
57	Spin-density matrix element components ρ_{00}^0 (blue) and ρ_{1-1}^0 (red) for different photon beam energies in 1.6-3.6 GeV range in Gottfried-Jackson frame.	82

CHAPTER 1

INTRODUCTION

The ϕ meson photoproduction mechanisms are not well understood yet. In "diffractive" regime the Pomeron exchange mechanism is dominant. Thus, ϕ meson photoproduction is an important tool to study the gluonic interactions, considering the gluonic structure of pomerons. Aslo, ϕ photoproduction process can be used to study the strangeness content of nucleons, using OZI rule violations, when the ϕ -nucleon interactions are taking place through the vector mesons exchanges. At high momentum transfers or high t , the ϕ photoproduction process is a good channel to study a nucleon resonance. This domain has not been studied very well until now. Experimental data for ϕ meson photoproduction are in a very limited kinematic range until now [1, 2, 5, 3, 4, 6, 7, 8]. Almost in all measurements the differential cross sections showed some unexprected local enhancement in approximately 1.8-2.4 GeV photon beam energy range (see Fig. 1). All the measurements were done without any cuts on $\Lambda(1520)$, which is a strong resonance that can coexist with $\phi(1020)$ (Fig. 3) . Moreover, the phase-spaces of the two resonances overlap nearly in the same photon energy region, where the local "structure" is observed in cross section plots of ϕ meson (Fig. 2). The inteferece between the resonances can have some noticeable effects in particle production processes [9, 10]. Therefore, ϕ meson cross section behavior could be due to coexistence of $\Lambda(1520)$ baryon and the interference between the Λ and ϕ .

Different collaborations have studied only the "charged" decay mode $\gamma p \rightarrow p\phi \rightarrow pK^+K^-$ of ϕ photoproduction. The current analysis is the first time measurement of the ϕ photoproduction in the "neutral" decay channel $\gamma p \rightarrow p\phi \rightarrow pK_SK_L$. In the "neutral" case there is no known coexisting prominent resonance as $\Lambda(1520)$ in "charged" channel. So this analysis gives a convenient possibility to check the ϕ meson photoproduction cross section and s-dependence of the t slope and compare the results of two decay modes. The high statistics data of g11 experiment allows not only measure a new decay mode, but also extend it into much wider kinematic range.

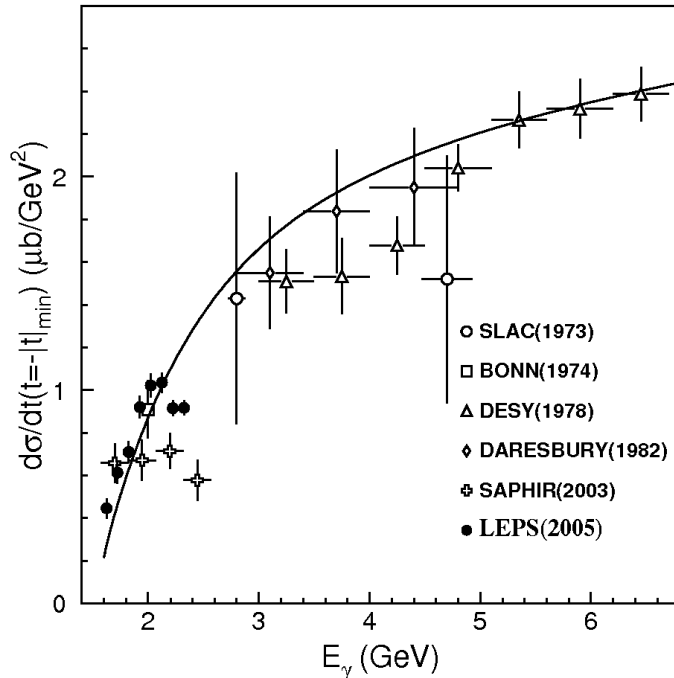


FIG. 1. Experimental results for the energy dependence of $(d\sigma/dt)_{t=-|t|_{min}}$ measured by different collaborations [2].

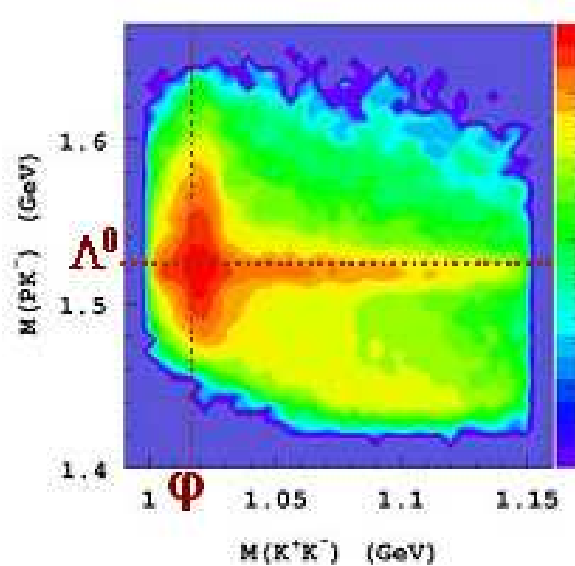


FIG. 2. Phase-space overlap of $\phi(1020)$ meson and $\Lambda(1520)$ baryon [11].

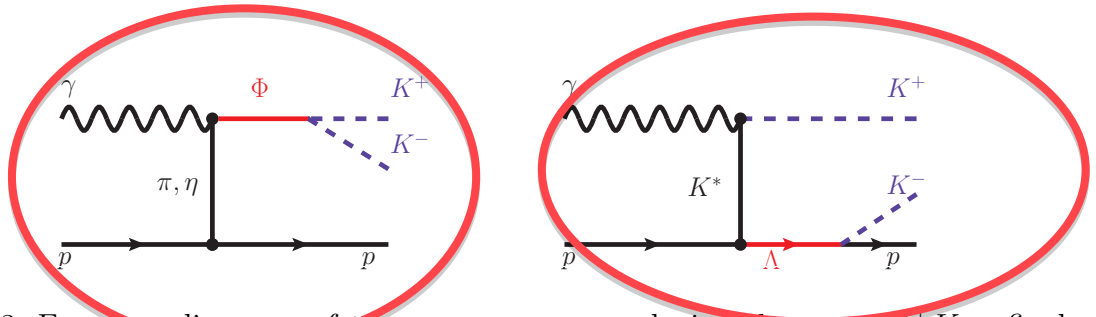


FIG. 3. Feynman diagrams of two γp processes producing the same K^+K^-p final state: via the ϕ resonance (left) and via the Λ resonance (right).

CHAPTER 2

THEORY

2.1 INTRODUCTION TO THEORY

The study of $\gamma p \rightarrow \phi p$ is important for many reasons. At high energy regime ($W \geq 10$ GeV) it is used to study the Pomeron exchange dynamics. But at relatively low energies ($W < 5$ GeV) only Pomeron exchange mechanism is not enough to describe the data. Here other mechanisms, such as meson exchange, must be considered in addition to the first, to obtain theory and data agreement. At low energies this process can be used to study the structure of baryon resonances and to search for missing resonances.

The ϕ meson mostly consists of strange quarks, i.e. $s\bar{s}$. By OZI rule [14] its production must be suppressed if the entrance channel does not have strange quarks. But there was observed a significant violation of this rule in some experiments with nucleons. So the ϕ photoproduction is also a good process to study the strange content of the nucleons.

According to [12],[13], in diffractive region, the main contribution in nonstrange amplitude of ϕ photoproduction is from Pomeron exchange amplitude (Figure 4(a)) and π and η pseudoscalar meson exchange amplitudes (Figure 4(b)). At high momentum transfers the main contribution is from excitation of nucleon resonances.

In diffractive amplitude there can also be some contribution from other trajectories associated with a scalar meson and f'_2 -meson, glueball or some other exotic channels. The small contributions from these channels can be determined only from comparisons with data and are not so well understood yet.

The $g_{\eta NN}$ and $g_{\phi NN}$ coupling constants are determined differently in different analysis. In Ref. [15] the parameters of Pomeron exchange, pseudoscalar η meson exchange and ϕ radiation mechanism are varied to fit the data.

In Titov's works ([12],[13]) the coupling constants are estimated theoretically. The analysis includes the $f'_2(1525)$ meson exchange and glueball exchange mechanism too. The photoproduction of ϕ meson is studied by analyzing three models:

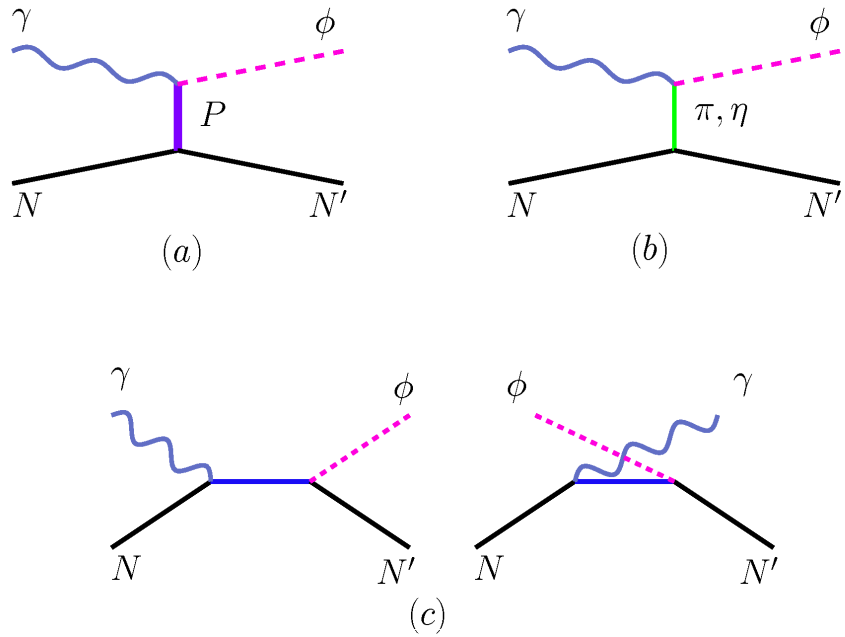


FIG. 4. Diagrams of ϕ meson production mechanisms by A.I. Titov [12]: (a) Pomeron exchange, (b) meson exchange, (c) ϕ meson radiation from nucleons.

- (model A) π, η exchange amplitude and the standard Pomeron (P_1) exchange
- (model B) model A + f'_2 meson exchange
- (model C) model A + the second Pomeron exchange (P_2) inspired by the ($J^\pi=0^+$, $M_b^2 \sim 3\text{GeV}^2$) glueball

2.2 KINEMATICAL VARIABLES

For the $\gamma N \rightarrow \phi N$ reaction S matrix ($S = \frac{1}{2}\sigma$) is related to the scattering amplitude T by

$$S_{fi} = \delta_{fi} - i(2\pi)^4 \delta^4(k + p - q - p') T_{fi} \quad (1)$$

where k , q , p and p' are the four momenta of the incoming photon, outgoing meson, initial and final nucleon, respectively. In the center-of-mass system (c.m.s.): $k=(\nu,\mathbf{k})$, $q=(E_\phi,\mathbf{q})$, $p=(E_p,-\mathbf{k})$, $p'=(E_{p'},-\mathbf{q})$.

The angle θ is the ϕ meson production angle in c.m.s. and is defined as : $\cos \theta \equiv \frac{\mathbf{k} \cdot \mathbf{q}}{|\mathbf{k}| |\mathbf{q}|}$
 $t=(p-p')^2 = (q-k)^2$ and $s=W^2=(p+k)^2$, $u=(p-q)^2=(k-p')^2$ are the standard Mandelstam variables.

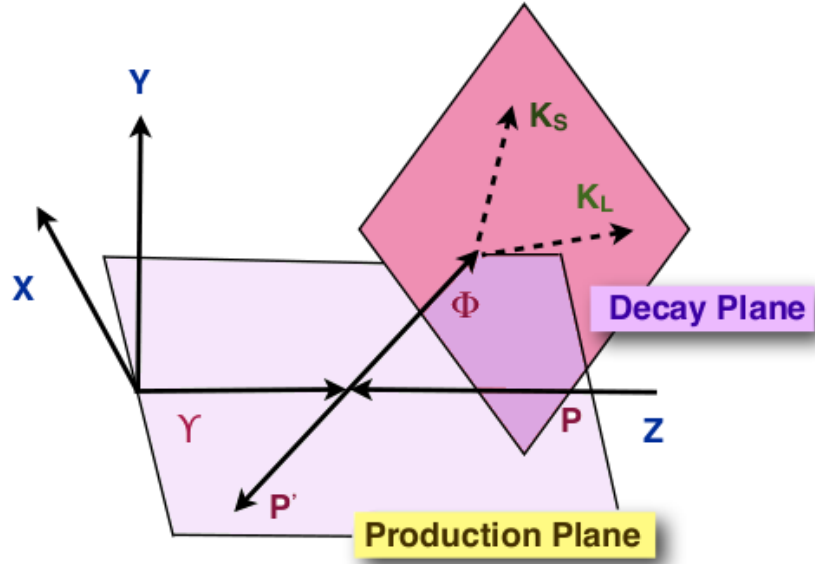


FIG. 5. The schematic pictures of the $\gamma N \rightarrow \phi N \rightarrow K_S K_L$ reaction in c.m.s.

The relation between the scattering amplitude T and the invariant amplitude I is

$$T_{fi} = \frac{I_{fi}}{(2\pi)^6 \sqrt{2E_\phi(\mathbf{q})2|\mathbf{k}|2E_p(\mathbf{p})2E_p(\mathbf{p}')}} \quad (2)$$

In the c.m.s. frame the cross section depends on invariant amplitude in the following way

$$d\sigma_{fi} = \frac{M_N^2}{2\pi^2(W^2 - M_N^2)} |I_{fi}|^2 \frac{dp'}{2E_{p'}} \frac{d\mathbf{q}}{2E_\phi} \delta^4(p + k - p' - q) \quad (3)$$

The differential cross section is

$$\frac{d\sigma_{fi}}{dt} = \frac{M_N^2}{16\pi(W^2 - M_N^2)^2} \sum_{m_i, m_f, \lambda_\gamma, \lambda_\phi} |I_{m_f, \lambda_\phi; m_i, \lambda_\gamma}|^2 \quad (4)$$

where m_i, m_f are the proton spin projections in the initial and final state, and $\lambda_\gamma, \lambda_\phi$ are the helicities of the incoming photon and outgoing meson.

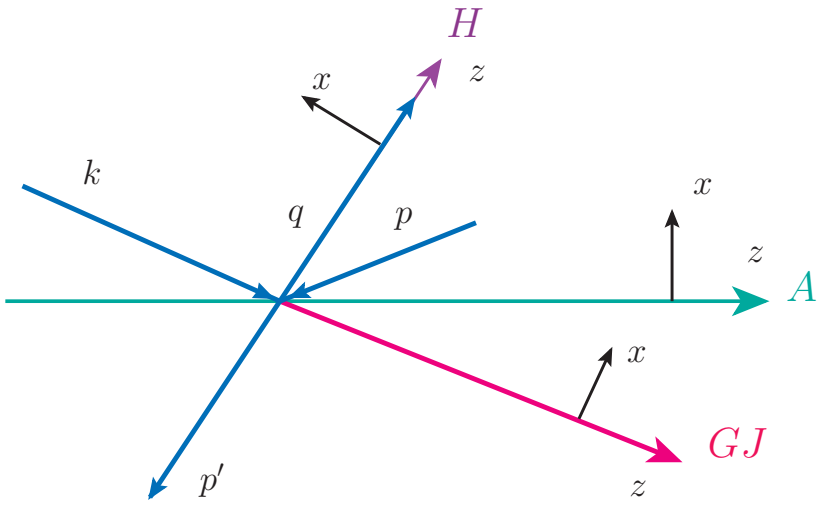


FIG. 6. Diagrammatic representation of GJ, H and A reference systems in ϕ meson rest frame.

Depending on the choice of the quantization axis z , the following three reference systems can be considered (Fig.6):

- Gottfried-Jackson system (GJ) where Z is in the direction of photon in the rest frame of ϕ .
- Helicity system (H) where Z point into the direction of ϕ in the total c.m.s. or opposite to the direction of the recoiling nucleon in the rest frame of ϕ .

- Adair system (A) with Z parallel with to the photon momentum in c.m.s.

The choice of the reference system is a matter of convenience and one can change one system by another one with a rotation. The GJ system is the most common for the theoretical calculations (also used in [12]), because certain amplitudes in this frame take a simple helicity conserving form for an arbitrary production angle θ .

The decay angles Θ and Φ are defined as the polar and azimuthal angles of the direction of one of the ϕ decay particles in ϕ meson rest frame.

The vector meson decay distributions in its rest frame are determined by spin-density matrices ρ_{ij}

$$\rho_{\lambda\lambda'}^0 = \frac{1}{N} \sum_{\alpha\lambda_\gamma} I_{\alpha;\lambda,\lambda_\gamma} I_{\alpha;\lambda',\lambda_\gamma}^\dagger \quad (5)$$

$$\rho_{\lambda\lambda'}^1 = \frac{1}{N} \sum_{\alpha\lambda_\gamma} I_{\alpha;\lambda,-\lambda_\gamma} I_{\alpha;\lambda',\lambda_\gamma}^\dagger \quad (6)$$

$$\rho_{\lambda\lambda'}^2 = \frac{i}{N} \sum_{\alpha\lambda_\gamma} \lambda_\gamma I_{\alpha;\lambda,-\lambda_\gamma} I_{\alpha;\lambda',\lambda_\gamma}^\dagger \quad (7)$$

$$\rho_{\lambda\lambda'}^3 = \frac{1}{N} \sum_{\alpha\lambda_\gamma} \lambda_\gamma I_{\alpha;\lambda,\lambda_\gamma} I_{\alpha;\lambda',\lambda_\gamma}^\dagger \quad (8)$$

where α includes the polarizations of the initial and final baryons and N is the normalization factor

$$N = \frac{1}{N} \sum_{\alpha\lambda_\gamma} |I_{\alpha;\lambda,\lambda_\gamma}|^2 \quad (9)$$

The $\phi \rightarrow a + b$ decay angular distribution W is defined as

$$\frac{dN}{d\cos\Theta d\Phi} = W(\cos\Theta, \Phi) = \frac{3}{4\pi} \sum_{\lambda,\lambda'} D_{\lambda,\lambda_{ab}}^{1*}(\Phi, \Theta, -\Phi) \rho_{\lambda\lambda'} D_{\lambda',\lambda_{ab}}^1(\Phi, \Theta, -\Phi) \quad (10)$$

In $\phi \rightarrow K_S K_L$, $\lambda_{ab} = \lambda_a - \lambda_b = 0$ and

$$W(\cos\Theta, \Phi) = \frac{3}{4\pi} \sum_{\lambda,\lambda'} D_{\lambda,0}^{1*}(\Phi, \Theta, -\Phi) \rho_{\lambda\lambda'} D_{\lambda',0}^1(\Phi, \Theta, -\Phi) \quad (11)$$

where Wigner rotation functions are

$$D_{l0}^1(\Phi, \Theta, -\Phi) = \frac{-l}{\sqrt{2}} \sin \Theta e^{-il\Phi} \quad (12)$$

$$D_{0l}^1(\Phi, \Theta, -\Phi) = \frac{l}{\sqrt{2}} \sin \Theta e^{il\Phi} \quad (13)$$

$$D_{00}^1(\Phi, \Theta, -\Phi) = \cos \Theta \quad (14)$$

$$D_{ll'}^1(\Phi, \Theta, -\Phi) = \frac{l}{2}(1 + ll' \cos \Theta) e^{-i(l-l')\Phi} \quad (15)$$

for $l, l' = \pm 1$.

$$\begin{aligned} W(\cos \Theta, \Phi) = & \frac{3}{4\pi} \left(\frac{1}{2}(\rho_{11} + \rho_{-1-1}) \sin^2 \Theta + \rho_{00} \cos^2 \Theta \right. \\ & + \frac{1}{\sqrt{2}}(-\Re \rho_{10} + \Re \rho_{-10}) \sin 2\Theta \cos \Phi \\ & + \frac{1}{\sqrt{2}}(\Im \rho_{10} + \Im \rho_{-10}) \sin 2\Theta \sin \Phi \\ & \left. - \Re \rho_{1-1} \sin^2 \Theta \cos 2\Phi + \Im \rho_{1-1} \sin^2 \Theta \sin 2\Phi \right) \end{aligned} \quad (16)$$

In the case of unpolarized photon beam

$$\begin{aligned} W^0(\cos \Theta, \Phi) = & \frac{3}{4\pi} \left(\frac{1}{2}(1 - \rho_{00}^0) + \frac{1}{2}(3\rho_{00}^0 - 1) \cos^2 \Theta \right. \\ & \left. - \sqrt{2}\Re \rho_{10}^0 \sin 2\Theta \cos \Phi - \rho_{1-1}^0 \sin^2 \Theta \cos 2\Phi \right) \end{aligned} \quad (17)$$

Inregrating (17) over azimuthal angle Φ one obtains

$$W^0(\cos \Theta) = \frac{3}{2} \left(\frac{1}{2}(1 - \rho_{00}^0) \sin^2 \Theta + \rho_{00}^0 \cos^2 \Theta \right) \quad (18)$$

And if one integrates (17) over angle Θ

$$W^0(\Phi) = \frac{1}{2\pi} (1 - 2\Re \rho_{1-1}^0 \cos 2\Phi) \quad (19)$$

2.3 THE DIFFRACTIVE AMPLITUDES

2.3.1 Pomeron exchange amplitudes

There are two models describing Pomeron exchange process in photoproduction of vector mesons. The vector meson dominance model (VDM) (Fig.7(a)) assumes that the incoming photon first converts into a vector meson which interacts to the nucleon by a Pomeron exchange [17, 18]. In [12, 13], Donnachie - Landshoff (DL) model [19] is used to find the Pomeron exchange amplitude. According to this model the incoming photon splits into quark and antiquark pair, interacts with the nucleon by a Pomeron and then combines into the final vector meson (Fig.7(b)). It is assumed that the pomeron behaves like a C=+1 isoscalar photon. The high energy data can be described by Pomeron trajectory with $\alpha(0) \sim 1.08$ intercept.

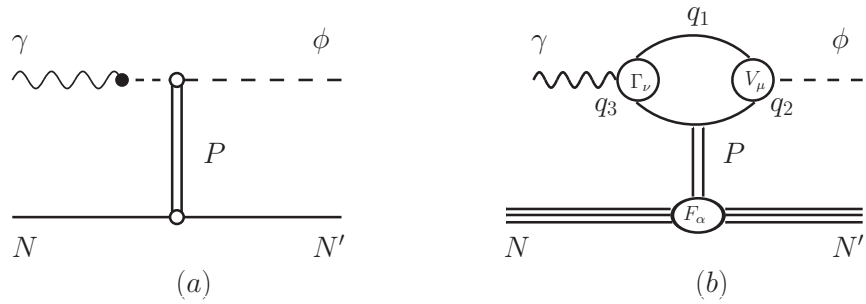


FIG. 7. Pomeron exchange models for ϕ meson production: (a) VDM model, (b) DL model [12].

In [13], using the factorized DL model, the invariant amplitude is expressed as

$$I_{fi}^P = -M_P(s, t)\varepsilon_\mu^\star(\lambda_\phi)\bar{u}_f h_P^{\mu\nu} u_i \varepsilon_\nu(\lambda_\gamma) \quad (20)$$

$u = u_m(p)$ – Dirac spinor of the nucleon,
 $\varepsilon_\nu(\gamma)$ – polarization vector of photon,
 $\varepsilon_\mu(\phi)$ – polarization vector of ϕ meson.

By Regge parametrization

$$M_P(s, t) = C_P F_1(t) F_\phi(t) \frac{1}{s} \left(\frac{s}{s_P} \right)^{\alpha_P(t)} e^{-i(\pi/2)\alpha_P(t)} \quad (21)$$

where $F_1(t)$ is the electromagnetic form factor of the nucleon and $F_\phi(t)$ is the form factor of the vector-meson-photon-Pomeron coupling. From [19] it follows that

$$F_1(t) = \frac{4M_N^2 - 2.8t}{(4M_N^2 - t)[1 - \frac{t}{0.7}]^2} \quad (22)$$

$$F_\phi(t) = \frac{2\mu_0^2}{(1 - \frac{t}{M_\phi^2})(2\mu_0^2 + M_\phi^2 t)} \quad (23)$$

$$\alpha_P(t) = 1.08 + 0.25t \quad (24)$$

$$C_P = \frac{6g^2\sqrt{4\pi\alpha_{em}}}{\gamma_\phi} \quad (25)$$

here γ_ϕ is the ϕ meson decay constant $2\gamma_\phi = 13.13$, $\alpha_{em} = \frac{e^2}{4\pi}$ and $g^2 \equiv g_{P_{ss}} \cdot g_{P_{qq}}$. $g_{P_{ss}}$ and $g_{P_{qq}}$ describe the Pomeron couplings with the strange quarks in ϕ meson and the light quarks in proton. Fitting the high energy data for vector mesons, parameters $\mu_0^2 = 1.1 GeV^2$, $s_P = 4 GeV^2$, $g_{P_{qq}} = 4.1$, $g_{P_{ss}} = 3.22$ were obtained.

From the Fig.7(b) follows

$$h_P^{\mu\nu} = k \left(g^{\mu\nu} - \frac{q^\mu q^\nu}{q^2} \right) - \gamma^\nu \left(k^\mu - \frac{q^\mu k \cdot q}{q^2} \right) - q^\nu \left(\gamma^\mu - \frac{q^\mu q^\nu}{q^2} \right) \quad (26)$$

In this equation the term that is proportional to k^ν does not have contribution, and the last term violates gauge invariance. To make it invariant the following gauge transformation is applied in [13]

$$q^\nu \rightarrow \bar{q}^\nu = q^\nu - \bar{p}^\nu \frac{k \cdot q}{\bar{p} \cdot k} \quad (27)$$

Using this transformation, the vertex has the following form

$$\Gamma_{fi}^P = \bar{u}_f \not{u}_i (\varepsilon_{\lambda_\phi}^\star \cdot \varepsilon_{\lambda_\gamma}) - \bar{u}_f \not{u}_{\lambda_\gamma} u_i (\varepsilon_{\lambda_\phi}^\star \cdot k) - \bar{u}_f \not{u}_{\lambda_\phi}^\star u_i \left(\varepsilon_{\lambda_\gamma} \cdot q - \frac{(\varepsilon_{\lambda_\gamma} \cdot \bar{p})(k \cdot q)}{\bar{p} \cdot k} \right) \quad (28)$$

Here \bar{p} must be fixed. It is done using Pomeron analogy to two gluons [22, 23, 24].

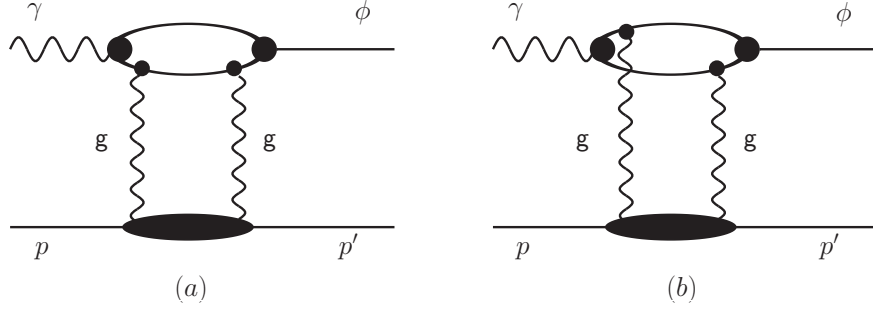


FIG. 8. Two gluon exchange mechanism for vector meson photoproduction [13].

To obtain gauge invariance, besides the two gluon interaction with the same quark (Fig.8(a)), must be taken into account the gluons interaction with different quarks (Fig.8(b)). In that case the amplitude obtains an additional term $\bar{u}(p') \not{u}_{\lambda_\gamma} u(p_1) \cdot \bar{u}(p_1) \not{u}_{\lambda_\phi}^\star u(p)$, where p_1 is the momentum of the quark in the intermediate state. At high energy limit and at small momentum transfers $p' \simeq p_1 \simeq p$, $\bar{u}(p') \gamma_\alpha u(p) \simeq 2p_\alpha$ and the vertex function is

$$\Gamma_{fi}^{2g} \sim (k \cdot p) (\varepsilon_{\lambda_{phi}}^\star \cdot \varepsilon_{\lambda_{gamma}}) - (\varepsilon_{\lambda_{gamma}} \cdot p) (\varepsilon_{\lambda_{phi}}^\star \cdot k) - (\varepsilon_{\lambda_{phi}}^\star \cdot p) \left(\varepsilon_{\lambda_{gamma}} \cdot q - \frac{(\varepsilon_{\lambda_{gamma}} \cdot p)(k \cdot q)}{p \cdot k} \right) \quad (29)$$

For low energies the choice for \bar{p} is $\frac{1}{2}(p + p')$.

2.3.2 Pseudoscalar meson exchange amplitudes

There are two models which can be used to find the pseudoscalar meson exchange amplitude:

1. one-boson-approximation (OBA) model [12, 13, 15, 26, 27]
2. Regge model [28, 29]

According to [13], using OBA model the effective Lagrangians are:

$$\mathcal{L}_{\phi\gamma\varphi} = \frac{eg_{\phi\gamma\varphi}}{M_\phi} \epsilon^{\mu\nu\alpha\beta} \partial_\mu \phi \partial_\nu A_\beta \varphi \quad (30)$$

$$\mathcal{L}_{\varphi NN} = -ig_{\pi NN} \bar{N} \gamma_5 \tau_3 N \pi^0 - ig_{\eta NN} \bar{N} \gamma_5 N \eta \quad (31)$$

where A_β is the photon field and φ is either π^0 or η meson. The invariant amplitude for the pseudoscalar meson exchange is

$$I_{fi}^{ps} = - \sum_{\varphi=\pi\eta} \frac{iF_{\varphi NN} F_{\phi\gamma\varphi}(t)}{t - M_\varphi^2} \frac{eg_{\phi\gamma\varphi} g_{\varphi NN}}{M_\phi} \bar{u}_{m_f}(p') \gamma_5 u_{m_i}(p) \epsilon^{\mu\nu\alpha\beta} q_\mu k_\alpha \varepsilon_\nu^\star(\phi) \varepsilon_\beta(\gamma) \quad (32)$$

According to Ref.[30]

$$F_{\varphi NN}(t) = \frac{\Lambda_\varphi^2 - M_\varphi^2}{\Lambda_\varphi^2 - t} \quad F_{\phi\gamma\varphi}(t) = \frac{\Lambda_{\phi\gamma\varphi}^2 - M_\varphi^2}{\Lambda_{\phi\gamma\varphi}^2 - t} \quad (33)$$

Here, from $NN\varphi$ vertex coupling constants $g_{\pi NN} = 13.26$ and $g_{\eta NN} = 3.527$, and from $\phi\gamma\varphi$ vertex, using the decay widths

$$\Gamma(\phi \rightarrow \gamma\pi^0) = (5.80 \pm 0.58) \times 10^{-6} GeV \quad (34)$$

$$\Gamma(\phi \rightarrow \gamma\eta) = (5.56 \pm 0.26) \times 10^{-5} GeV \quad (35)$$

where the coupling constants $g_{\phi\gamma\pi} = -0.141$, $g_{\phi\gamma\eta} = -0.707$.

The Λ parameters for π^0 exchange are obtained from ω photoproduction analysis [31, 30] : $\Lambda_\pi = 0.6 GeV^2$, $\Lambda_\eta = 0.9 GeV^2$, $\Lambda_{\phi\gamma\pi} = 0.6 GeV^2$ and $\Lambda_{\phi\gamma\eta} = 1.0 GeV^2$.

2.3.3 f'_2 meson and glueball exchange

Both f'_2 meson and glueball exchanges are possible in ϕ meson photoproduction, thus their contribution must be included in total amplitude. The effective lagrangians for this two trajectories are the following:

$$\mathcal{L}_{0+} = \frac{1}{4}g_{\alpha\beta}(\Lambda^{\alpha\beta} + \Lambda^{\beta\alpha})\xi \quad (36)$$

$$\mathcal{L}_{2+} = \frac{1}{4}g_{\alpha\beta}(\Lambda^{\alpha\beta} + \Lambda^{\beta\alpha})\xi_{\alpha\beta} + (\Lambda^{\alpha\beta} - \Lambda^{\beta\alpha})\xi_{\alpha\beta} \quad (37)$$

where

$$\Lambda^{\alpha\beta} = \partial_\mu\phi_1^\alpha\partial^\mu\phi_2^\beta + \partial^\alpha\phi_1^\mu\partial^\beta\phi_{2\mu} - \partial^\alpha\phi_1^\mu\partial_\mu\phi_2^\beta - \partial_\mu\phi_1^\alpha\partial^\beta\phi_2^\mu \quad (38)$$

The vertices are

$$h_{0+}^{\mu\nu} = g^{\mu\nu}k \cdot q - k^\mu q^\nu \quad (39)$$

$$h_{2+}^{\mu\nu} = h_{0+}^{\mu\nu} - 2i\sigma_{\alpha\beta}[g^{\alpha\mu}g^{\beta\nu}k \cdot q + q^\alpha k^\beta g^{\mu\nu} + g^{\alpha\nu}q^\beta k^\mu + g^{\beta\mu}k^\alpha q^\nu] \quad (40)$$

The scalar function for $R = (f'_2, \text{glueball})$ is

$$M_R(s, t) = C_R F_1(t) F_\phi(t) \frac{1}{N_R} \left(\frac{s}{s_R} \right)^{\alpha_R(t)} \frac{\eta_R(1 + e^{-i\pi\alpha_R(t)})\pi\alpha'_R}{2\sin(\pi\alpha_R)\Gamma(\alpha_R(t))} \quad (41)$$

Here in C_P instead of g_P is g_R . $N_{2+} \simeq 2sM_\phi$, $N_{0+} \simeq M_N M_\phi^2$. From [28] $\alpha_{f'_2} = 0.55 + 0.7t$ and $s_{f'_2} = 1\text{GeV}^2$. For the glueball trajectory, from [32] $\alpha_{gl} = -0.75 + 0.25t$ and $s_{gl} = 4$.

The η_R and g_R parameters are obtained making the theoretical models fit the existing data for unpolarized total cross section. $g_{f'_2} = 1.87$, $\eta_{f'_2} = +1$; $g_{gl} = 7.66$, $\eta_{gl} = -1$.

2.4 BARYON AND BARYON RESONANCE EXCHANGE

2.4.1 Baryon resonance exchange

The baryon resonance exchange is believed to be the main mechanism for the backward angle ϕ photoproduction. In [13] an effective Lagrangian approach is used, developed for ω -meson photoproduction, to describe this processes. It includes all known isospin $I=1/2$ nucleon resonances listed in PDG [33]: $P_{11}(1440), D_{13}(1520), S_{11}(1535), S_{11}(1650), D_{15}(1675), F_{15}(1680), D_{13}(1700), P_{11}(1710), P_{13}(1720), F_{17}(1990), D_{13}(2080), G_{17}(2190)$.

For N^* with $J^P = \frac{1}{2}^\pm, \frac{3}{2}^\pm, \frac{5}{2}^\pm, \frac{7}{2}^\pm$, the effective Lagrangians are

$$\mathcal{L}_{\gamma NN^*}^{\frac{1}{2}^\pm} = \frac{eg_{\gamma NN^*}}{2M_{N^*}} \bar{\psi}_{N^*} \Gamma^{(\pm)} \sigma_{\mu\nu} F^{\mu\nu} \psi_N + \text{h.c.} \quad (42)$$

$$\mathcal{L}_{\gamma NN^*}^{\frac{3}{2}^\pm} = i \frac{eg_{\gamma NN^*}}{M_{N^*}} \bar{\psi}_{N^*}^\mu \gamma_\lambda \Gamma^{(\mp)} F^{\lambda\mu} \psi_N + \text{h.c.} \quad (43)$$

$$\mathcal{L}_{\gamma NN^*}^{\frac{5}{2}^\pm} = \frac{eg_{\gamma NN^*}}{M_{N^*}^2} \bar{\psi}_{N^*}^{\mu\alpha} \gamma_\lambda \Gamma^{(\pm)} (\partial_\alpha F^{\lambda\mu}) \psi_N + \text{h.c.} \quad (44)$$

$$\mathcal{L}_{\gamma NN^*}^{\frac{7}{2}^\pm} = -i \frac{eg_{\gamma NN^*}}{M_{N^*}^3} \bar{\psi}_{N^*}^{\mu\alpha\beta} \gamma_\lambda \Gamma^{(\mp)} (\partial_\beta \partial_\alpha F^{\lambda\mu}) \psi_N + \text{h.c.} \quad (45)$$

where ψ_{N^*} , ψ_α , $\psi_{\alpha\beta}$ and $\psi_{\alpha\beta\gamma}$ are the Rarita-Schwinger spin $\frac{1}{2}, \frac{3}{2}, \frac{5}{2}$ and $\frac{7}{2}$ fields, A_μ is the photon field, and $F^{\mu\nu} = \partial^\nu A^\mu - \partial^\mu A^\nu$. $\Gamma^+ = 1(\Gamma^- = \gamma_5)$ defines the N^* excitations with different parity.

2.4.2 Direct ϕ meson Radiation

According to [12], the effective Lagrangians for the ϕNN and γNN interactions are

$$\begin{aligned}\mathcal{L}_{\phi NN} &= -g_{\phi NN} \left(\overline{N} \gamma_\mu N \phi^\mu - \frac{\kappa_\phi}{2M_N} \overline{N} \sigma^{\mu\nu} N \partial_\nu \phi_\mu \right) \\ \mathcal{L}_{\gamma NN} &= -e \left(\overline{N} \gamma_\mu N A^\mu - \frac{\kappa_N}{2M_N} \overline{N} \sigma^{\mu\nu} N \partial_\nu A_\mu \right)\end{aligned}\quad (46)$$

where $\kappa_p = 1.79$. The amplitude is

$$\begin{aligned}I_{fi}^C &= \overline{u}_{m_f}(p') M_{\mu\nu}^C \varepsilon_{\lambda_\phi}^{*\mu} \varepsilon_{\lambda_\gamma}^\nu u_{m_i}(p) \\ M_{\mu\nu}^C &= e g_{\phi NN} \left[\Gamma_\mu^\phi(q) \frac{p'_s + M_N}{p_s^2 - M_N^2} \Gamma_\nu^\gamma(k) + \Gamma_\nu^\gamma(k) \frac{p'_u + M_N}{p_u^2 - M_N^2} \Gamma_\mu^\phi(q) \right]\end{aligned}\quad (47)$$

where

$$\begin{aligned}\Gamma_\mu^\phi(q) &= \gamma_\mu - i \frac{\kappa_\phi}{2M_N} \sigma_{\mu\nu} q^\nu \\ \Gamma_\mu^\gamma(k) &= f_N \gamma_\mu + i \frac{\kappa_N}{2M_N} \sigma_{\mu\nu} k^\nu\end{aligned}\quad (48)$$

$f_p = 1$, $p_s = p + k$, $p_u = p - q$. It is theoretically estimated in [34] that $g_{\phi NN} = -0.24$, $\kappa_\phi = 0.2$

2.5 THEORETICAL RESULTS AND EXPECTATIONS

2.5.1 Unpolarised cross section

In the total cross section the main contribution is from the diffractive channels at small $|t| < 1 GeV^2$. The main contributing mechanisms are the Pomeron and pseudoscalar meson exchange mechanisms. Four models are considered:

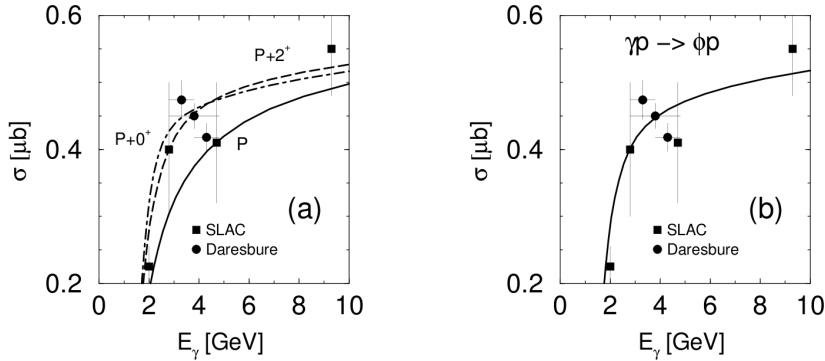


FIG. 9. The total cross section as a function of photon energy: (a) modeels A,B and C indicated by dashed, long-dashed and dot-dashed curves, (b) hybrid model [13].

- (model A) π, η exchange amplitude and the standard Pomeron (P_1) exchange
- (model B) model A + f'_2 meson exchange
- (model C) model A + the glueball trajectory
- (hybrid model) model A + small contribution from f'_2 and glueball with equal weights

In Fig.9 the theoretical results for the total cross section as a function of photon energy are plotted: (a) for the models A,B and C, and (b) for the hybrid model. Comparing the results with the existing data was found relatively good agreement for models B and C. But the precision of the data does not allow to choose which model fits the data the best, so for the further calculations was used the hybrid model, including both. The sum of the Pomeron, f'_2 and glueball amplitudes is denoted as 'diffractive'.

In Fig.10(a) the differential cross section is plotted as a function of $-t$ at $E_\gamma = 2.2$ GeV. In the calculation for the resonance channel the OZI-rule evading parameter is selected $x_{OZI}=4$. The diffractive part of the differential cross section is described by the hybrid model. It can be observed from the plot that the forward-angle photoproduction is completely defined by diffractive amplitude, the backward-angle photoproduction is well described by the resonant N^* -exchange mechanism and the central

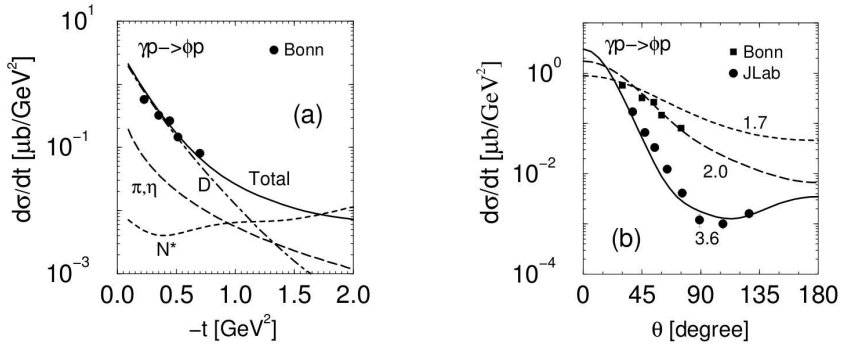


FIG. 10. (a) The differential cross section as a function of $-t$ at $E_\gamma = 2.2$ GeV for PS exchange (long-dashed), diffractive channels (dot-dashed), resonance excitation (dashed) and the total amplitude (solid). (b) The differential cross section as a function of ϕ production angle at $E_\gamma = 1.7, 2.0$ and 3.6 GeV. The data are from [35, 36]. [13].

region can be described only by the sum of all the processes. The (b) plot of the same figure shows the differential cross section - production angle in c.m.s. dependence at three different photon energies. There is a pretty good agreement between the theoretical results and the data.

2.5.2 Spin observables

All the calculations for the spin observables are done in Gottfried-Jackson system in [13]. The model applicability at $E_\gamma \sim 2 - 3$ GeV is limited by the forward and backward photoproduction with $|t_{min}| \leq |t| \leq |t_l|$ and $|t_l| \leq |t| \leq |t_{max}|$, respectively, where $|t_l| \simeq 0.5 - 0.7$ GeV^2 , depending on energy.

For the forward angle photoproduction the scalar and pseudoscalar meson exchange amplitudes are

$$I_{m_f m_i; \lambda_\phi \lambda_\gamma}^{U^N}(t) = \begin{pmatrix} 1 \\ 2m_i \lambda_\gamma \end{pmatrix} \delta_{m_i m_f} \delta_{\lambda_\gamma \lambda_\phi} I_0^{U^N}(t) \quad (49)$$

The Pomeron exchange amplitude in GJ system has the following form

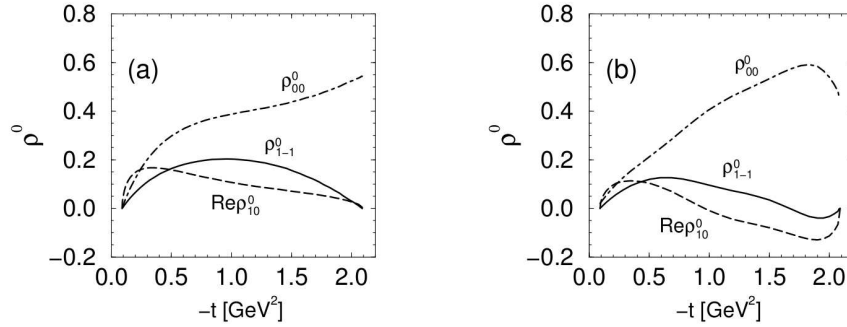


FIG. 11. The spin-density matrix elements as a function of $-t$ at $E_\gamma = 2.2$ GeV: (a) for the Pomeron exchange amplitude, (b) for the full model [13].

$$I_{fi}^P \equiv -\delta_{\lambda_\phi \lambda_\gamma} \bar{u}_f \not{k} u_i + \delta_{\lambda_\phi 0} k_\gamma \bar{u}_f \not{\gamma} u_i + \sqrt{2} \lambda_\gamma p_x \frac{k \cdot q}{2p \cdot k - k \cdot q} \bar{u}_f \not{\gamma}^\star \not{k} u_i \quad (50)$$

where k_γ and p_x are the photon momentum and x component of the proton momentum. The second term in (50) describes the interaction of the photon and nucleon spins and interaction of the ϕ meson spin and the orbital momentum in the initial state. The last term describes the ϕ meson and nucleon spins interaction and the interaction of the photon spin with the orbital momentum in the final state. So the second and the last terms are responsible for the spin-flip transitions $\lambda_\gamma \rightarrow \lambda_\phi = 0$. The most contribution is from the second term and it is estimated as

$$\rho_{00}^0 \simeq \frac{k_\gamma^2(|t| + 2p_x^2)}{\bar{s}^2} \quad (51)$$

$$\bar{s}^2 = (s - M_N^2)^2 \left(1 - \frac{M_\phi^2 + |t|}{s - M_N^2}\right)$$

The double spin-flip transition $\lambda_\gamma \rightarrow \lambda_\phi = -\lambda_\gamma$ is connected with the photon spin interaction with the orbital momentum. It generates ρ_{1-1}^0 , which is defined by the interference of the first and the last terms

$$\rho_{1-1}^0 \simeq \frac{p_x^2(M_\phi^2 + |t|)}{\bar{s}^2} \quad (52)$$

In Fig.11 the spin-density matrix ρ^0 elements are plotted as function of $-t$ for $E_\gamma = 2.2$ GeV. This matrix defines the ϕ meson decay product particles angular

distribution in reaction with unpolarized photons. At forward angle photoproduction the spin-density matrix elements are determined by Pomeron exchange processes, but at high momentum transfers mostly the resonance excitations are important.

In Fig.12 the angular distribution function for the unpolarized photons is plotted for three different $|t|$ values. At the small momentum transfers the ϕ mesons are produced with the spins aligned along the quantization axis z' . This is expressed in $W^0 = \sin^2 \Theta$ dependence. As the $|t|$ increases, the spin-flip processes make the produced ϕ mesons longitudinally polarized. At large momentum transfers $W^0 \simeq a + b \cos^2 \Theta$, where $a, b > 0$. The Φ dependence of the W^0 is determined only by spin-flip processes. The amplitude of the oscillations increases with increasing value of $|t|$, reaches the maximal value at $|t| \sim 0.6 \text{ GeV}^2$ and then again decreases. The spin-density matrix elements ρ_{1-1}^0 determined by the azimuthal angle dependences and mostly describe the gluon-exchange processes. At very high momentum transfers the resonant channels play the main role.

Fig.13 represents the ρ_{00}^0 and ρ_{1-1}^0 photon energy dependences at fixed $|t|=0.4 \text{ GeV}^2$ value for the Pomeron-exchange and full amplitudes. The value of ρ_{00}^0 increases with the energy, indicating the increase of longitudinally-polarized ϕ mesons with energy.

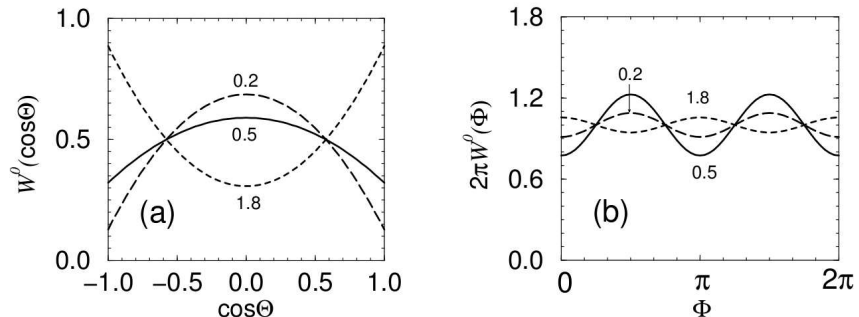


FIG. 12. Angular distribution function at $E_\gamma = 2.2 \text{ GeV}$ and $|t|=0.2, 0.5$ and 1.8 GeV^2 as a function of: (a) $\cos \Theta$, (b) Φ . [13]

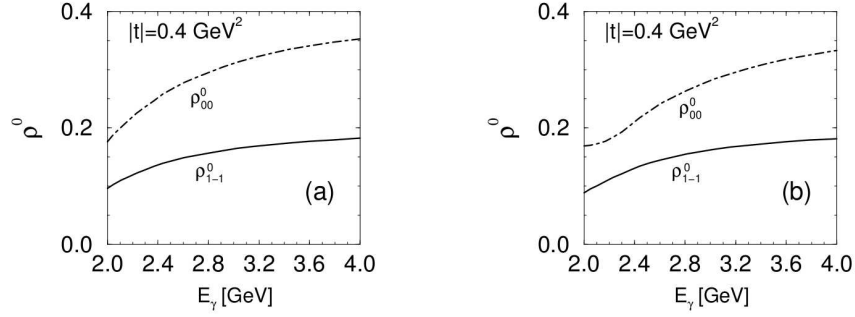


FIG. 13. Spin-density matrix elements as a function of E_γ at $|t|=0.4 \text{ GeV}^2$ for: (a) Pomeron exchange amplitude, (b) full model. [13]

2.6 SUMMARY

The ϕ meson photoproduction in diffractive regime is dominated by Pomeron exchange, π and η pseudoscalar meson exchange process and there is some contribution from exotic channels like f'_2 meson exchange, glueball exchange mechanisms. At high momentum transfers the nuclear resonance excitations start to play the dominant role and there is observed large deviation from OZI rule. The spin-dependent part in Pomeron exchange amplitude is responsible for the spin-flip transitions in ϕ photoproduction process. These transitions have large input in spin-density matrix elements and can be measured from the ϕ meson decay angular distribution data. The double spin-flip transitions are related to the ρ_{1-1}^0 spin-density matrix element and can be obtained from azimuthal angle dependence part of the angular distribution function. More available data and more precise measurements of the cross section and spin observable will allow to study the production mechanisms in more detail and give answers to some questions that are still open in this topic.

CHAPTER 3

DATA ANALYSIS

In this analysis is used the data set from g11 experiment. The experiment ran between May the 17th and July the 29th 2004 in Hall-B at the Thomas Jefferson National Accelerator Facility (TJNAF), in Newport News, VA. The average current during the experiment was 65nA, which provided luminosity on the order of 80 pb^{-1} (Fig.14). During the experiment the Bremsstrahlung photon beam(up to 4.016 GeV) was incident on 40cm liquid Hydrogen target as a source of protons, and the final charged particles were detected using the CEBAF Large Acceptance Spectrometer (CLAS). Photon tagger was used to distinguish between the photons. Though the main purpose of the experiment was to carry out search for exotic baryons, the high statistics data created a nice opportunity to study many other interesting channels, one of which is $p\phi$.

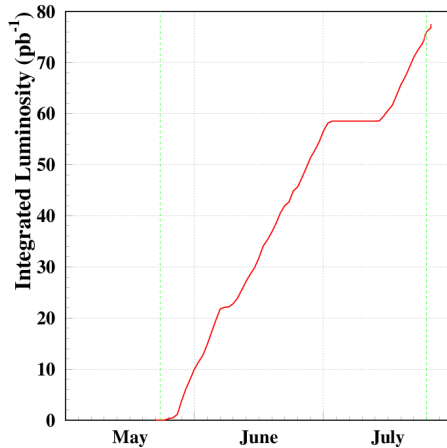


FIG. 14. Integrated Luminosity of the g11 experiment.

This analysis purpose was to study the ϕ meson production in neutral decay mode : $\gamma + p \rightarrow p + \phi \rightarrow p + K_S + K_L$. This channel has a branching fraction of approximtely 34% in the total ϕ meson production. The neutral K_S has $8.953 \times 10^{-11} \text{ s}$ mean lifetime and was identified using its decay into $\pi^+\pi^-$ or $\pi^0\pi^0$ pair. The final particles were detected in CLAS. In this chapter we will give a broad description of

the steps performed to select the data for the analysis and the cuts and corrections applied to the data for the current study of ϕ meson production.

3.1 DATA SELECTION

For the analysis three charged particle events were selected in the final state - proton, π^+ and π^- . The particles were identified using PART bank information. The GPART was selected to be equal to 3. There was also a requirement of no neutral particles in the final events set. To select the photons, there was a requirement to have only one photon present in the tagger within ± 2 ns time interval between the tagger and the CLAS - $|TAG_{time} - ST_{time}| < 2$. This cut helps to choose the right photon for event in the case of detecting more than one photon with time close to the event start time.

There were minimal momentum cuts on protons and pions: $P_\pi > 0.1(GeV/c)$, $P_p > 0.35(GeV/c)$.

Several other cuts and corrections were applied to data before the measurements. These cuts and corrections are discussed in detail in the following sections.

3.2 ENERGY AND MOMENTUM CORRECTIONS

The data for the analysis was corrected using the standard g11 energy and momentum correction packages. These corrections included the charged particle energy loss correction [41], tagger energy corrections, momentum correction of the particles [40]. In the following part of this work each correction will be discussed briefly.

3.2.1 Tagger Energy Corrections

It was observed that there is a deviation between the proton mass and the missing mass of the $\gamma p \rightarrow K^+ K^- X$ reaction $\Delta M = M_X - M_{proton}$. This deviation depended on run number (Fig.15(a)). To solve the problem, the electron energy was corrected on run-by-run bases. In average, the corection factor $R = E_{corrected}/E_{initial}$ was equal to 1.005, showing that the detected beam energy was about 0.5% less than the actual one. The correction factor R depending on run number is plotted on Fig.15(b). The

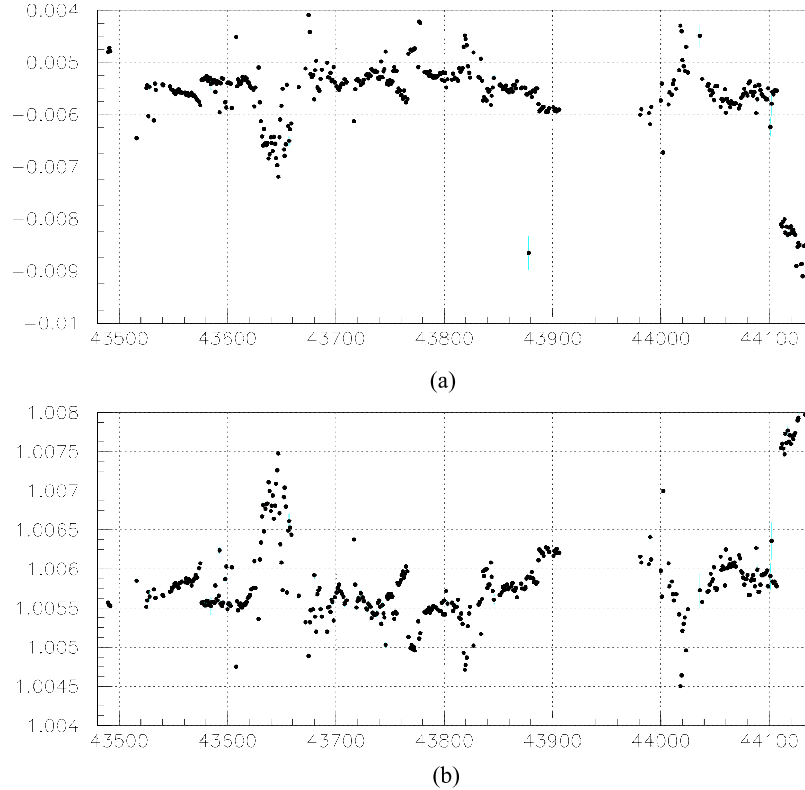


FIG. 15. (a) The missing mass shift in the reaction $\gamma p \rightarrow K^+K^-X$, $\Delta M = M_X - M_{proton}$, (b) Beam energy correction factor $R = E_{corrected}/E_\gamma$ as a function of run number. [40]

corrections were different for the run numbers grater than 44108, where the beam energy was higher.

The photon energy corrections were checked using $\gamma p \rightarrow \pi^+\pi^-X$ reaction. Tagger energy corrections as a function of tagger ID are plotted on Fig.16, where the red points are the corrections before electron energy corrections were applied, and the blue points correspond to the corrections after electron energies were corrected. The several shifted points correspond to the swept wires. This was taken into account during the correction. After these corrections were applied, the missing proton mass was shifted to its correct value. This can be seen from Fig.17, where the missing mass of the proton in $\gamma p \rightarrow \pi^+\pi^-X$ is plotted as a function of tagger ID.

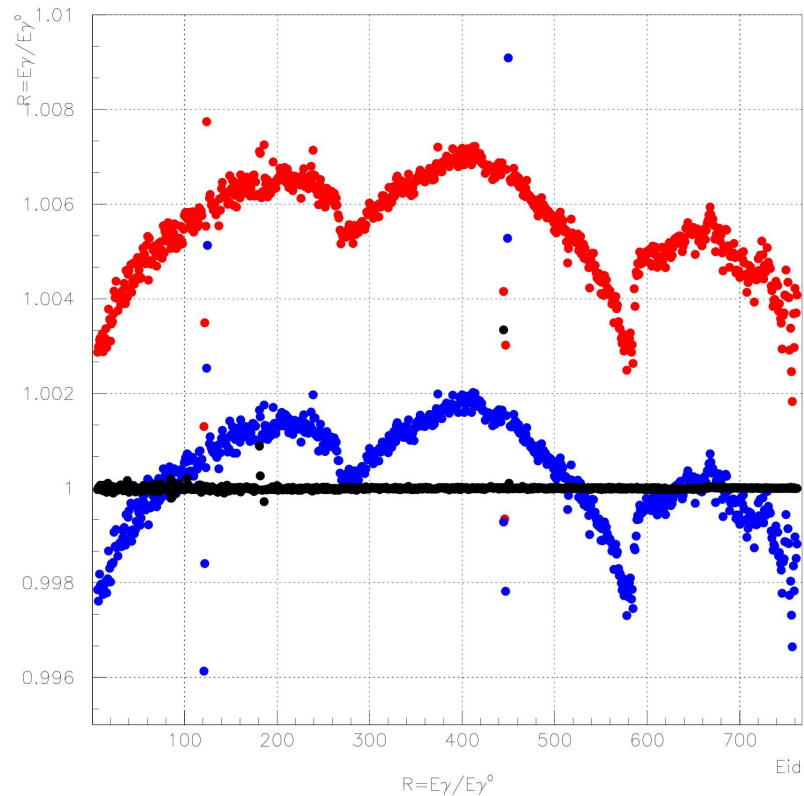


FIG. 16. Tagger energy correction $R = E_\gamma / E_{\gamma^0}$ as a function of tagger ID. [40]

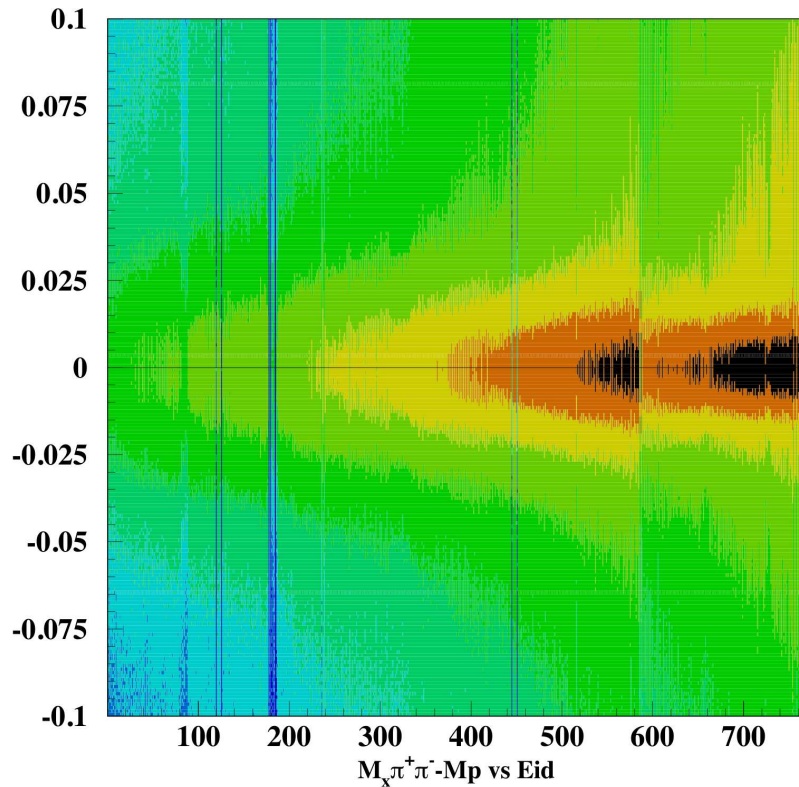


FIG. 17. The difference of the missing mass of the reaction $\gamma p \rightarrow \pi^+\pi^- X$ and proton mass $\Delta M = M_X - M_p$ as a function of tagger ID after the tagger energy correction. [40]

3.2.2 Energy Loss Correction

The charged particles during their interaction with matter lose energy because of ionization and atomic excitations. The momenta of the proton, π^+ and π^- were corrected for the energy loss using CLAS software eloss package written by E. Pasyuk [41]. This correction includes the energy loss in the target material and walls, the beam pipe, the start counter and the air between the start counter and the drift chambers in Region 1. The energy loss was estimated using the momenta and masses of the particles. This correction does not include the energy loss due to the fight of the particle in magnetic field.

3.2.3 Momentum Corrections

This momentum corrections, obtained by V. Kubarovskiy, were based on missing mass technique. Two reactions were used to find the corrections: $\gamma p \rightarrow \pi^+ \pi^- p$ and $\gamma p \rightarrow K^+ k^- p$. The missing masses of proton, pions and kaons were used to correct the momenta. In this procedure only one variable ϕ was involved, although it is possible to correct using θ, ϕ and P variables together. In this case the corrections for the θ and P variables were very small and could be neglected. The corrections were obtained for $p\pi^+$, γ^- , K^+ , K^- and protons. The corrections for the π^+ , K^+ and protons were obtained from their missing mass distributions in $\gamma p \rightarrow \pi^+ \pi^- p$ reaction and for the protons - from the $\gamma p \rightarrow K^+ K^- p$ reaction. The corrections $R = P_{corrected}/P_{measured} - 1$ for these particles are plotted in Fig.18.

The momentum corrections for the negative π^- and K^- were also obtained from the mentioned two reactions and they are plotted in Fig.19.

Using the data in these figures the momentum corrections were calculated using extrapolation method. As a function of ϕ the momentum corrections are on the order of about $\pm 1\%$. The missing mass distributions of the protons before and after the corrections are plotted in Fig.20. The missing and invariant masses of some other particles are plotted in Fig.21. The resolutions of the particles have somewhat improved, and the missing mass values are differing from their table values not more than 1MeV.

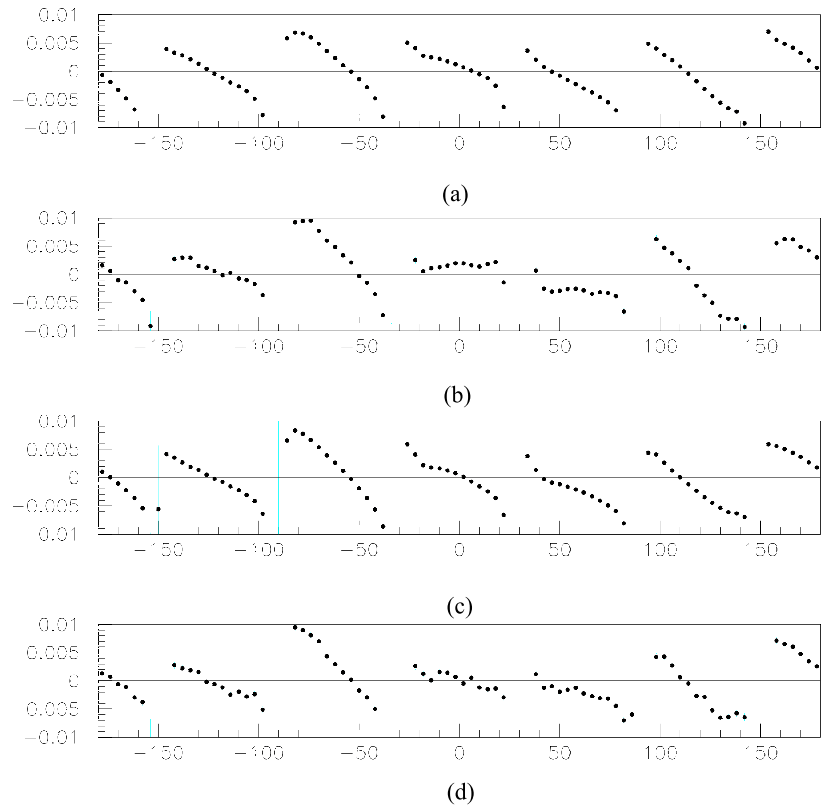


FIG. 18. Momentum corrections for positive particles (π^+, K^+ , protons) $R = P_{\text{corrected}}/P_{\text{measured}} - 1$ estimated from the missing mass distributions in: (a,b,c) $\gamma p \rightarrow \pi^+ \pi^- p$, (d) for the protons from the reaction $\gamma p \rightarrow K^+ K^- p$. [40]

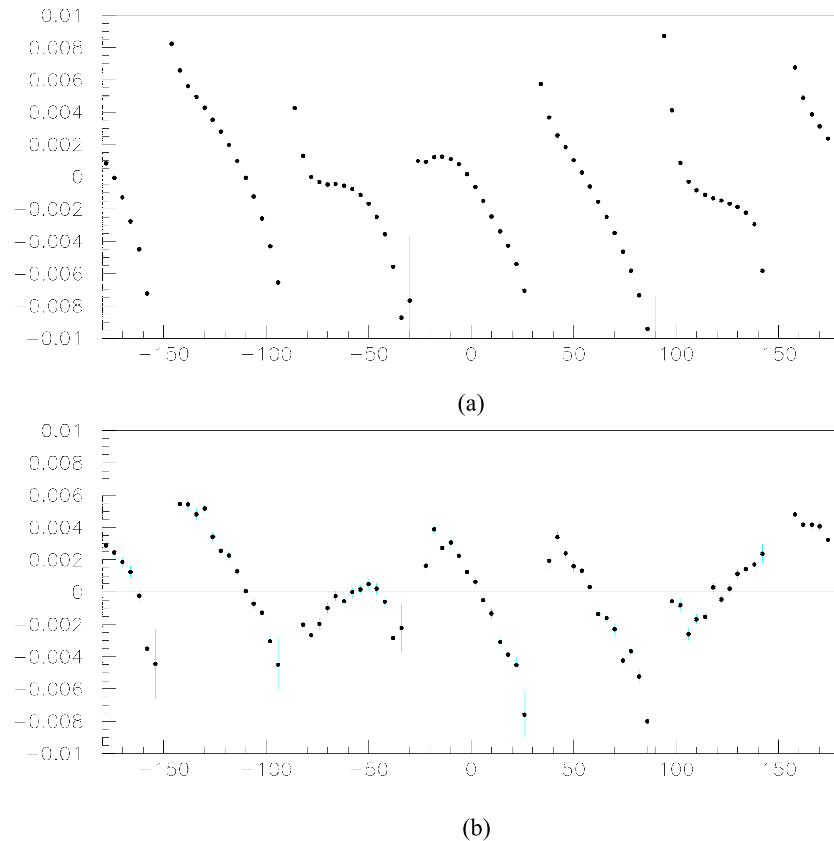


FIG. 19. Momentum corrections for negative particles (π^- , K^-)
 $R = P_{\text{corrected}}/P_{\text{measured}} - 1$. [40]

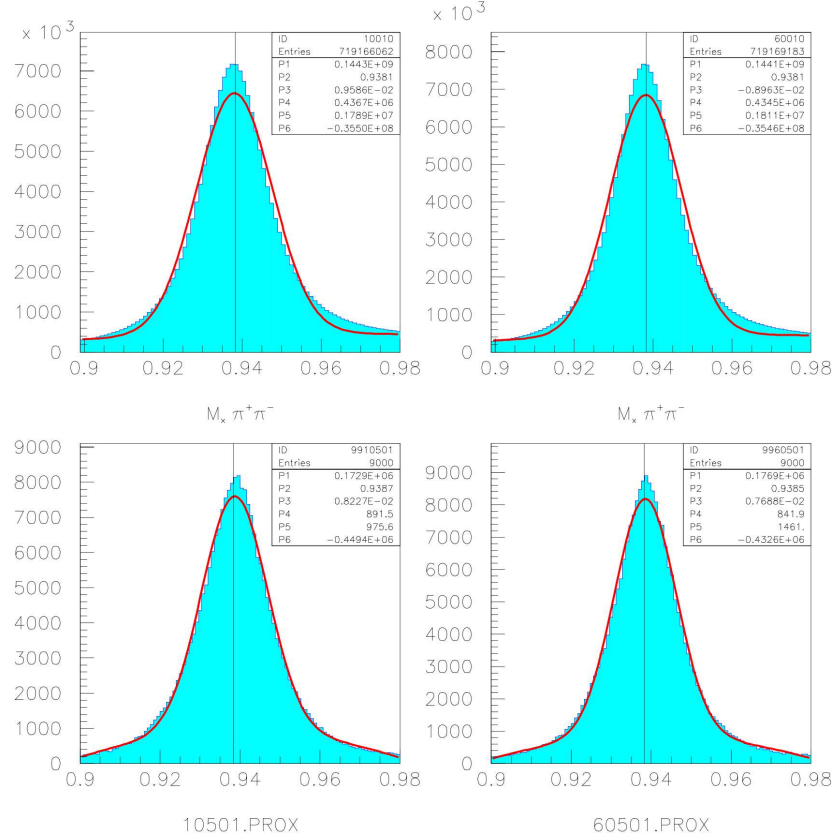


FIG. 20. The mass distributions of missed protons before and after the corrections were applied in two reactions:(a) $\gamma p \rightarrow \pi^+ \pi^- X$, (b) $\gamma p \rightarrow K^+ K^- X$. [40]

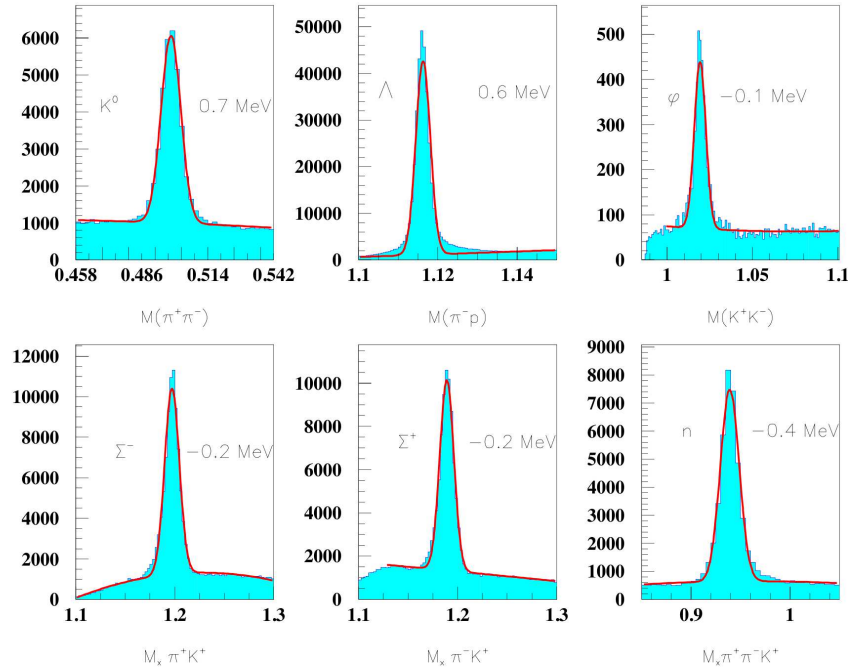


FIG. 21. Invariant and missing masses after all corrections were applied. [40]

3.3 DETECTOR EFFICIENCY CORRECTIONS

Due to missing wires in the drift chamber or gains in phototubes because of high voltages the detector can be less efficient in some regions. To correct the data for these effects we must obtain the detector efficiency for the particles . In this analyses the proton, π^+ and π^- detection efficiencies were obtained using two reactions: $\gamma p \rightarrow p\pi^+\pi^-$ and $\gamma p \rightarrow p\pi^+\pi^-\pi^+\pi^-$. The events were selected based on complete exclusivity and when one particle is missed but reconstructed by missing mass. The efficiencies were obtained for every θ and ϕ angle.

To obtain the efficiencies for the protons the available dataset was devided into the following four momentum bins: (0.35 - 0.4) GeV/c, (0.4 - 0.45) GeV/c, (0.45 - 0.55) GeV/c, > 0.55 GeV/c. For each momentum region the efficiencies were calculated using (53) and (54).

$$Ef_p = \frac{N(\gamma p \rightarrow \pi^+\pi^-p)}{N(\gamma p \rightarrow \pi^+\pi^-)p} \quad (53)$$

$$Ef_p = \frac{N(\gamma p \rightarrow \pi^+\pi^-\pi^+\pi^-p)}{N(\gamma p \rightarrow \pi^+\pi^-\pi^+\pi^-)p} \quad (54)$$

In equations (53) and (54) the protons in numerator correspond to detected proton events, and the protons in denominator are obtained from the missing mass of the reactions. In Fig.22 the θ angle is plotted versus the ϕ angle for the detected protons and for the missing protons in the two reactions $(\gamma p \rightarrow \pi^+\pi^-)p$ and $(\gamma p \rightarrow \pi^+\pi^-\pi^+\pi^-)p$. The efficiencies were obtained from the histogram ratios.

The efficiencies for the positively charged pions were obtained deviding the dataset into the following four momentum regions: (0.1 - 0.15) GeV/c, (0.15 - 0.2) GeV/c, (0.2 - 0.3) GeV/c, > 0.3 GeV/c. For each momentum region the efficiencies were calculated using (55) and (56).

$$Ef_{\pi^+} = \frac{N(\gamma p \rightarrow \pi^+\pi^-p)}{N(\gamma p \rightarrow \pi^-p)\pi^+} \quad (55)$$

$$Ef_{\pi^+} = \frac{N(\gamma p \rightarrow \pi^+ \pi^- \pi^+ \pi^- p)}{N(\gamma p \rightarrow \pi^+ \pi^- \pi^- p) \pi^+} \quad (56)$$

In equations (55) and (56) the positive pions in numerator correspond to detected π^+ events, and the positive pions in denominator are obtained from the missing mass of the reactions. In Fig.23 the θ angle is plotted versus the ϕ angle for the detected π^+ and for the missing π^+ in the two reactions $(\gamma p \rightarrow \pi^- p) \pi^+$ and $(\gamma p \rightarrow \pi^+ \pi^- \pi^- p) \pi^+$. The efficiencies were obtained from the histogram ratios.

The efficiencies for the negatively charged pions were calculated for the same momentum regions as for the positive pions: (0.1 - 0.15) GeV/c, (0.15 - 0.2) GeV/c, (0.2 - 0.3) GeV/c, > 0.3 GeV/c. For each momentum region the efficiencies were calculated using (57) and (58).

$$Ef_{\pi^-} = \frac{N(\gamma p \rightarrow \pi^+ \pi^- p)}{N(\gamma p \rightarrow \pi^+ p) \pi^-} \quad (57)$$

$$Ef_{\pi^-} = \frac{N(\gamma p \rightarrow \pi^+ \pi^- \pi^+ \pi^- p)}{N(\gamma p \rightarrow \pi^+ \pi^- \pi^+ p) \pi^-} \quad (58)$$

In equations (57) and (58) the negative pions in numerator correspond to detected π^- events, and the negative pions in denominators are obtained from the missing mass of the reactions. In Fig.24 the θ angle is plotted versus the ϕ angle for the detected π^- and for the missing π^- in the two reactions $(\gamma p \rightarrow \pi^+ p) \pi^-$ and $(\gamma p \rightarrow \pi^+ \pi^- \pi^+ p) \pi^-$. The efficiencies were obtained from the histogram ratios.

To include all angles there are 180 θ bins and 360 ϕ bins in all cases.

In Fig.25 (a) protons' polar Θ angles are plotted versus azimuthal angles Φ before the efficiency corrections were applied. The (b) histogram of the same figure is

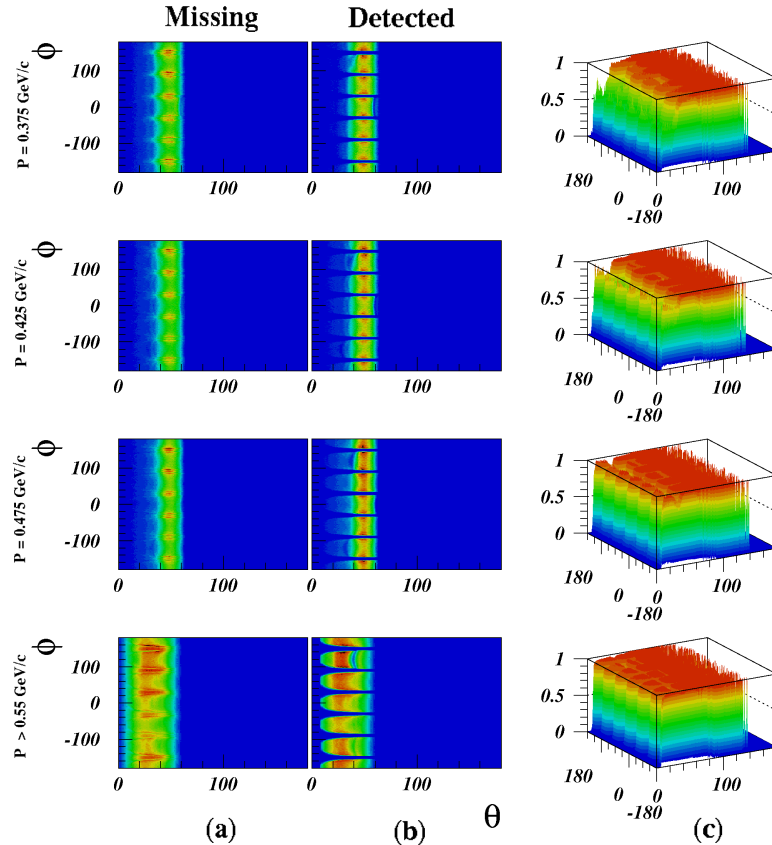


FIG. 22. The calculation of efficiency coefficients for the protons. (a) The missing protons θ angle vs ϕ angle; (b) The detected protons θ angle vs ϕ ; (c) The 3D plots of efficiency coefficients for the protons plotted versus θ and ϕ angles in different momentum ranges.

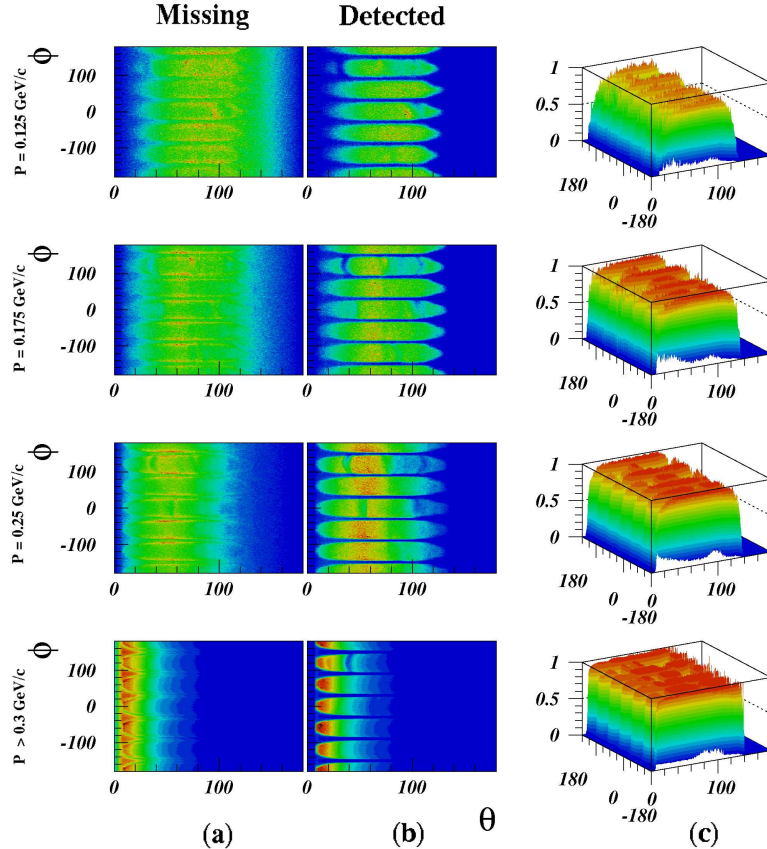


FIG. 23. The calculation of efficiency coefficients for the positive pions. (a) The missing π^+ θ angle vs ϕ angle; (b) The detected π^+ θ angle vs ϕ ; (c) The 3D plots of efficiency coefficients for the positive pions plotted versus θ and ϕ angles in different momentum ranges.

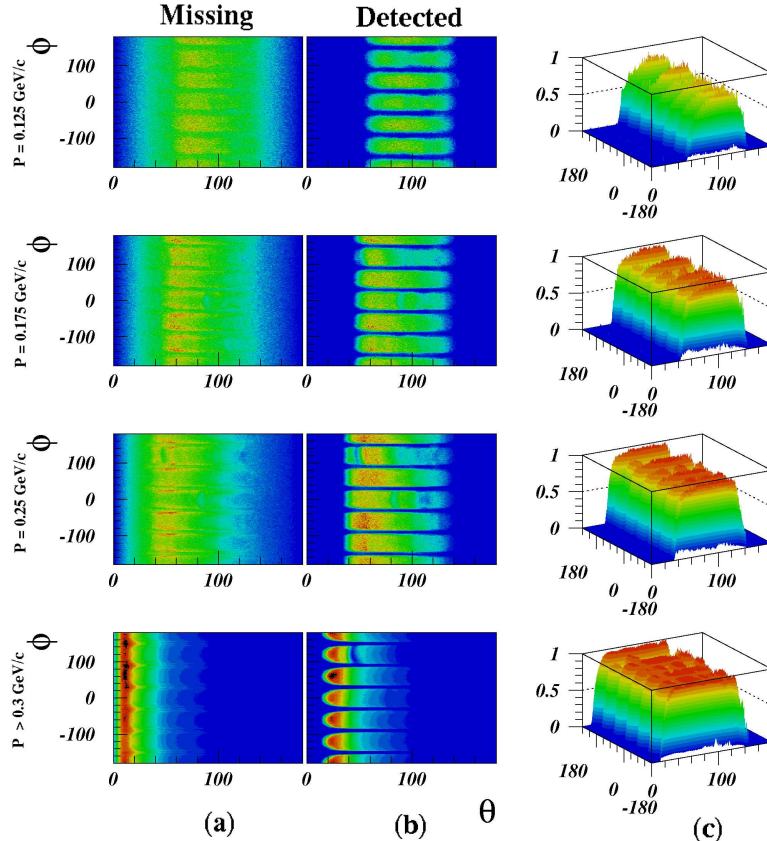


FIG. 24. The calculation of efficiency coefficients for the negative pions. (a) The missing $\pi^- \theta$ angle vs ϕ angle; (b) The detected $\pi^- \theta$ angle vs ϕ ; (c) The 3D plots of efficiency coefficients for the protons plotted versus θ and ϕ angles in different momentum ranges.

the vertical projection of the histogram in (a). Fig.25 (c) is the proton angular distributions plot after the efficiency corrections were applied, and (d) is projection of (c).

In Fig.26 (a) π^+ mesons' polar Θ angles are plotted versus azimuthal angles Φ before the efficiency corrections were applied. The (b) histogram of the same figure is the vertical projection of the histogram in (a). Fig.26 (c) is the positive pion angular distributions plot after the efficiency corrections were applied, and (d) is projection of (c).

In Fig.27 (a) π^- mesons' polar Θ angles are plotted versus azimuthal angles Φ before the efficiency corrections were applied. The (b) histogram of the same figure is the vertical projection of the histogram in (a). Fig.27 (c) is the negative pion angular distributions plot after the efficiency corrections were applied, and (d) is projection of (c).

The holes at $\Phi = 300$ degrees (Sector 6) is because of dead drift chamber wires and scintillators, which significantly decrease the efficiency. These bad paddles were cut both in data and during the acceptance calculations.

3.4 FIDUCIAL CUTS

The fiducial cuts were applied to eliminate the detector bad regions, where the efficiency changes rapidly. For this reason an efficiency cut of 40% was applied both to data and generated events. Also we put cuts on dead scintillator paddles during the acceptance calculation. The following paddles were eliminated:

Sect	SPID
1	33
3	11
5	23

TABLE I. Removed dead scintillator paddles.

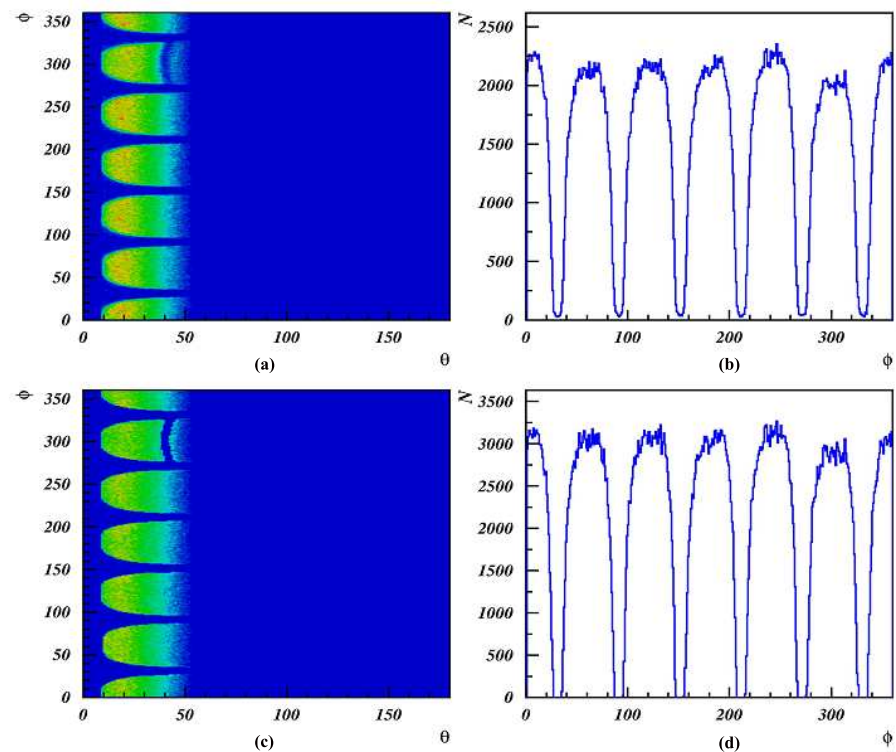


FIG. 25. Proton angular distributions:(a),(b) before efficiency corrections, (c),(d) after efficiency corrections.

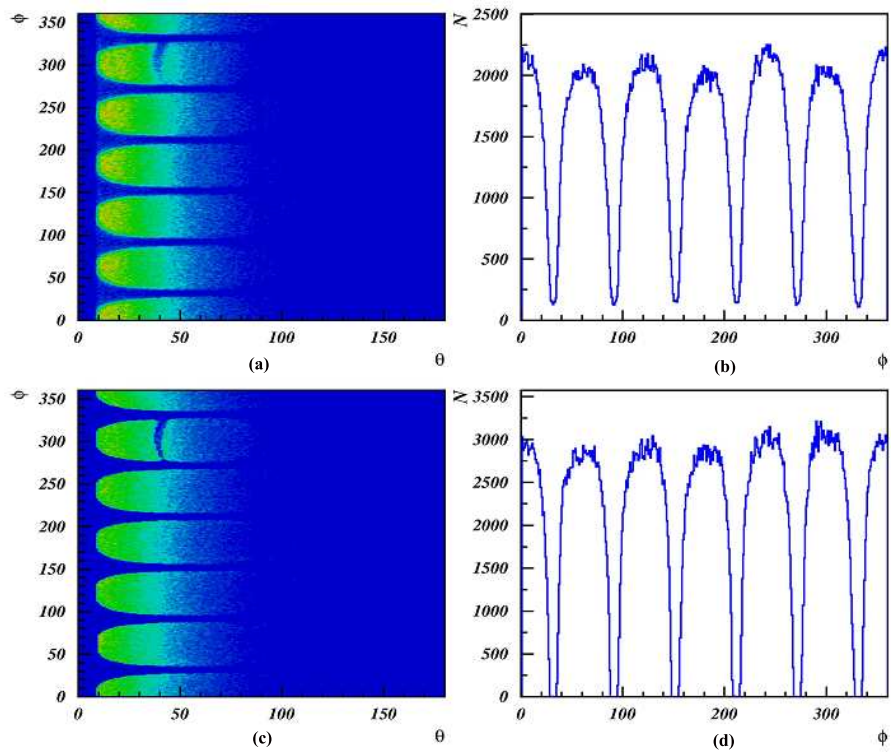


FIG. 26. π^+ meson angular distributions:(a),(b) before efficiency corrections, (c),(d) after efficiency corrections.

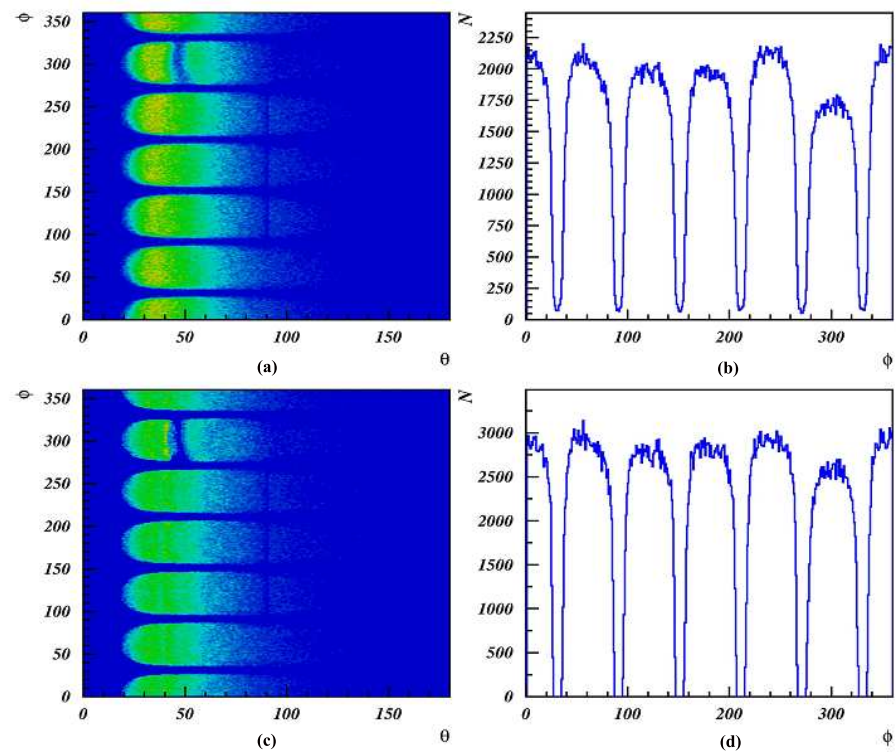


FIG. 27. π^- meson angular distributions: (a),(b) before efficiency corrections, (c),(d) after efficiency corrections.

3.5 VERTEX CUT

Some detected events could come from interactions on the target aluminium walls. To eliminate these events, 2cm vertex cut was applied to Z components of the target proton vertices from left and right. So only the region $Z \in [-8 : 28]$ of the interaction vertex was kept in the analysis. This cut was applied also to the generated events during the acceptance calculation.

3.6 PARTICLE IDENTIFICATION

To reconstruct ϕ mesons for the analyses the neutral kaons K_S and K_L should be identified. The K_s particle was identified through its $\pi^+\pi^-$ decay mode ($\sim 68.6\%$ b.r.). The invariant mass of π^+ and π^- was taken to be the mass of $K_s \pm 3\sigma$ ($M(K_S) = 0.49765 \pm 0.008(GeV/c^2)$). The missing mass of $\gamma p \rightarrow p'\pi^+\pi^-X$ was required to be the mass of $K_L \pm 3\sigma$ ($M(K_L) = 0.49765 \pm 0.015(GeV/c^2)$). The ϕ mesons were reconstructed as the invariant mass of K_SK_L system.

In Fig.28 the invariant mass of $\pi^+\pi^-$ system is plotted, requiring the missing mass of $\gamma p \rightarrow \pi^+\pi^-p(X)$ to be within $30MeV/c^2$ interval around K_L mass. One can see a nice K_S peak with some small background. In Fig.29 the missing mass of $\gamma p \rightarrow \pi^+\pi^-p(X)$ is plotted, requiring the invariant mass of $p\pi^+\pi^-$ be the mass of K_S . The peaks of several possible final particles can be identified from this histogram, including the K_L mesons. Figure 30 shows the missing mass of $\gamma p \rightarrow \pi^+\pi^-p(X)$ plotted in mass range $0.45 - 0.55GeV/c^2$. There are two cuts applied: invariant mass of $\pi^+\pi^-$ to be within $16MeV/c^2$ interval around K_S mass, and the invariant mass of K_SK_L be less than $1.07GeV/c^2$. The invariant mass of K_SK_L is plotted in Fig.31 with very broad cuts on K_s and K_L masses. The peak of ϕ meson is visible with a very large background. The signal-to-background ratio was significantly improved after 3σ cuts were applied to K_S and K_L masses. The invariant mass of K_SK_L system after the cuts is plotted on Fig.32.

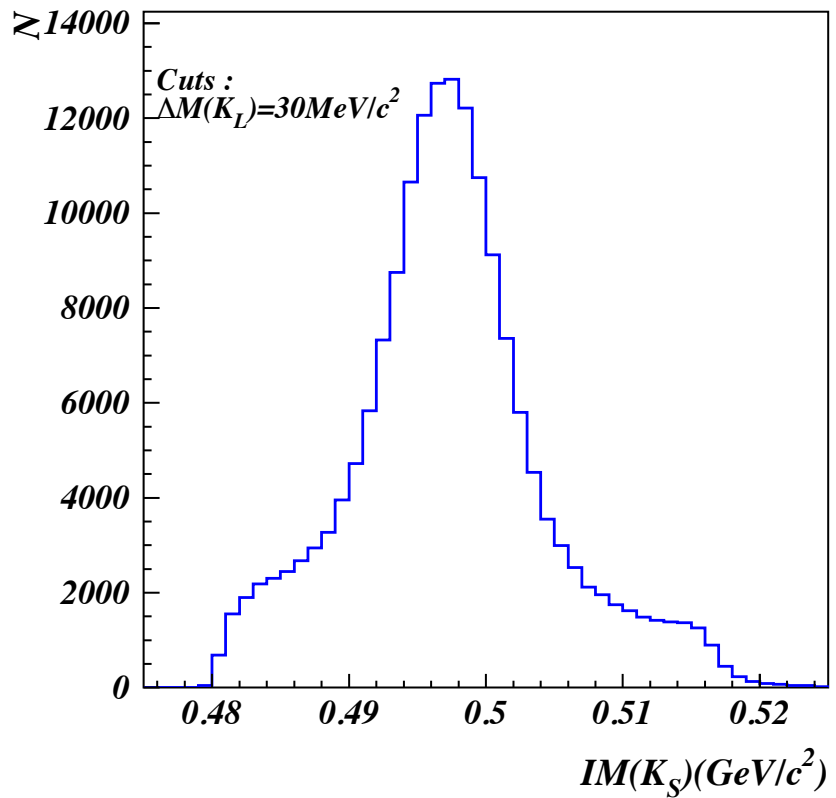


FIG. 28. Invariant mass of $\pi^+\pi^-$ system with a cut on mass of missing K_L from $\gamma p \rightarrow p\pi^+\pi^-(X)$ reaction: $\Delta M(K_L) = 30 MeV/c^2$.

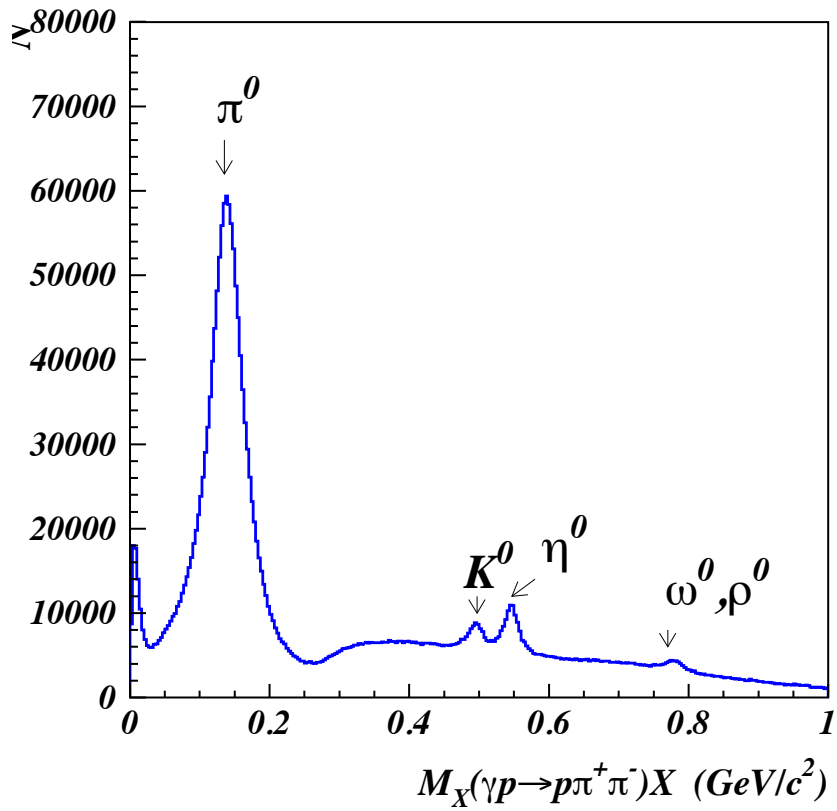


FIG. 29. Missing mass of $\gamma p \rightarrow p\pi^+\pi^-X$ reaction, with a cut on invariant mass of $\pi^+\pi^-$: $M(\pi^+\pi^-) < 0.015 GeV/c^2$.

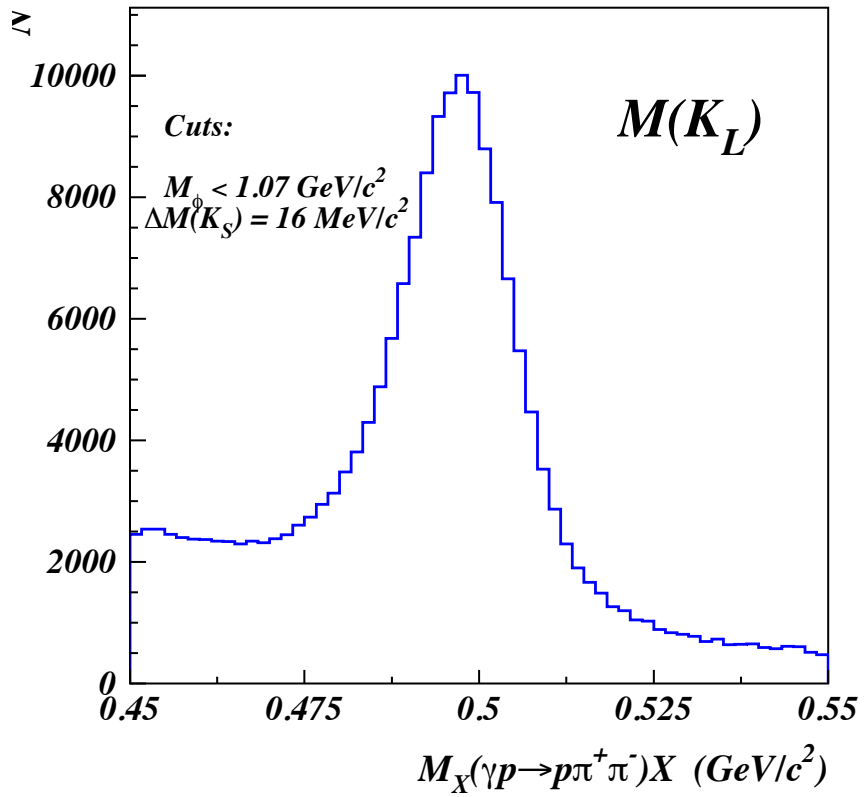


FIG. 30. Missing mass of $\gamma p \rightarrow p\pi^+\pi^-(X)$ reaction in $0.45-0.55$ GeV/c^2 range, with cuts: $\Delta M(K_S) = 16 MeV/c^2$ and $M(K_SK_L) < 1.07 GeV/c^2$.

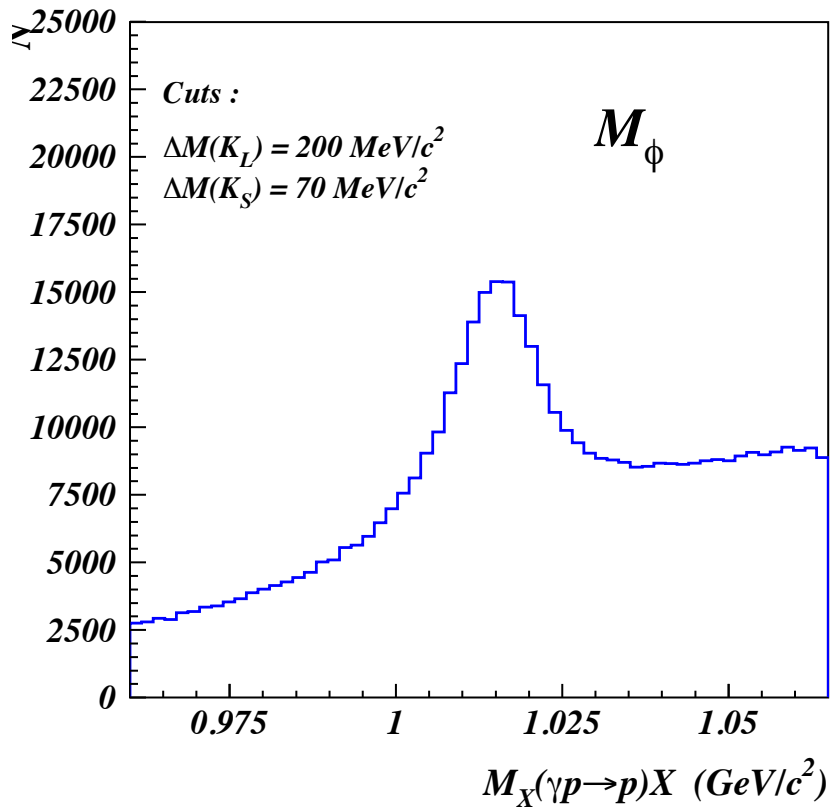


FIG. 31. Invariant mass of K_SK_L with very broad cuts: $\Delta M(K_S) = 70 MeV/c^2$ and $\Delta M(K_L) = 200 MeV/c^2$.

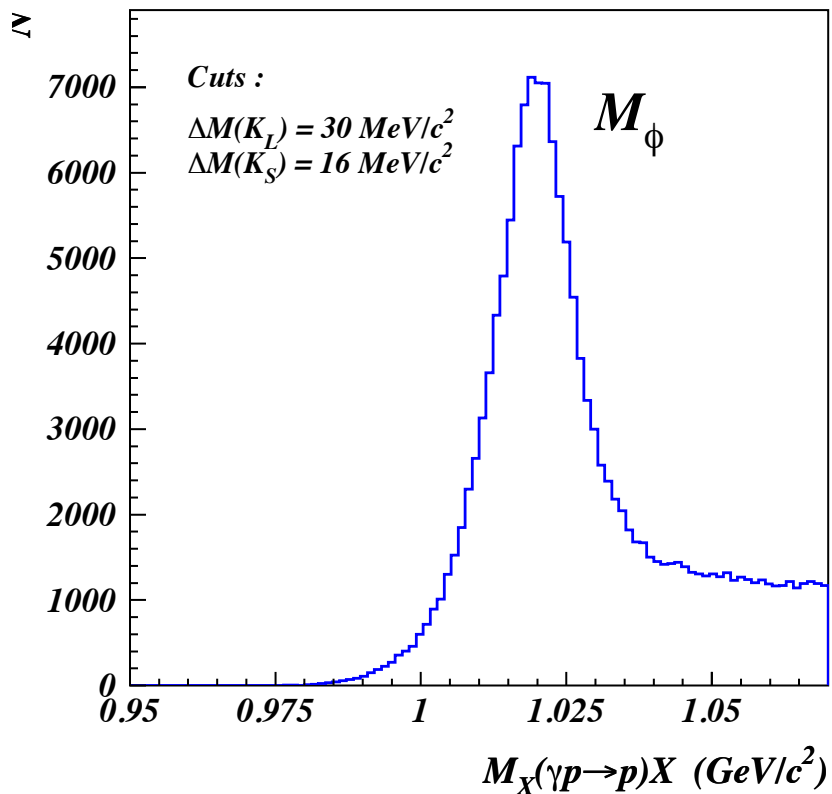


FIG. 32. Invariant mass of K_SK_L with cuts: $\Delta M(K_S) = 16 \text{ MeV}/c^2$ and $\Delta M(K_L) = 30 \text{ MeV}/c^2$.

3.7 BACKGROUND SEPARATION

From Fig.32 we see that even after all the cuts were applied to clean the 'bad' events, there is still some background left. There is almost no background in the left side, but there is high background in the right side of the ϕ peak. For the cross section measurements we need only the ϕ events. For the measurements the ϕ mesons signal was selected as $M(\phi) = 1.02 \pm 0.02 GeV/c^2$. The background was selected from the right sideband of the mass distribution with an equal size interval as for the signal: $M(\phi) = 1/2 * N(1.06 \pm 0.02(GeV/c^2))$. Only the half of the events in the selected background interval are considered, because there is very negligible background on the left side of the peak. The selection of 1/2 coefficient was an approximate choice. This uncertainty was taken care of with systematic errors calculation, using several different possible coefficients. This will be described in the section describing the systematic error determination.

3.8 ACCEPTANCE CORRECTION AND NORMALIZATION

3.8.1 Monte Carlo generator

Some of the particles fly to dead regions of the detector and it is not possible to detect them. Also, during the cooking some events can be lost. There can be several reasons why some events are not getting accounted. To correct the data for these inefficiencies, the data must be normalized with acceptance. To obtain the acceptance for this analysis were used ϕ meson Monte Carlo generator, CLAS GSIM and RECSIS packages. The Monte Carlo generator is based on data and was created using several iterations method. The cross section is generated as

$$f(e) \frac{\beta e^{\beta(t-t_{min})}}{1 - e^{\beta(t-t_{min})}} [(1 - \rho_{00}) + (3\rho_{00} - 1) \cos^2 \Theta] \quad (59)$$

where $\rho_{00}=0.11817$, $\alpha=3.4$.

As initial energy distribution, the K^+K^- energy distribution was taken from D.Tedeshchi's analysis for the charged channel ϕ meson photoproduction. [38]

The energy distribution was then fit with the following function:

$$f(x) = Ae^{-0.5\frac{(x-B)^2}{B^2}} + D + Ex + Fx^2 + Gx^3 \quad (60)$$

A,B,C,D,E,F,G parameters and ρ_{00} were varied to make the Monte Carlo fit the data. The same was done for the t_ϕ distribution.

Generator and CLAS GSIM and RECSIS packages were used several times to obtain good agreement between the generator and the data (see the scheme 33).



FIG. 33.

3.8.2 Acceptance

To obtain the acceptances for the current analysis, first events were uniformly generated in space with the Monte Carlo generator. Then the generated events were processed through GSIM, which is based on GEANT and simulates the CLAS detector. The software imitates the particle motion into the detector and simulates detection signals. GSIM imitates some processes affecting the particles in detector, like the energy losses of the particles in the detector, any possible particle decays and scattering effects on the particle motion in the CLAS detector. Finally, RECSIS reconstruction program was used to cook GSIM output, like experimental data was cooked. Some cuts and corrections were applied to the reconstructed events:

- Energy loss momentum corrections,
- Fiducial cuts (cut on unefficient regions of the detector, dead scintillator paddles cuts),
- Vertex cut (to eliminate the contamination from the target walls)

The fiducial cuts were based on efficiency calculation. The regions that had efficiency lower than 40% were eliminated to obtain the acceptance. The same cut was applied to data. To calculate the systematic errors we applied different efficiency cuts. This will be described in the section 4.3

The acceptance was calculated as

$$\text{Acceptance} = \frac{\text{Reconstructed events (with corrections and cuts)}}{\text{Generated events}} \quad (61)$$

The acceptances for each $t - t_{min}$ bin and different photon energy ranges are plotted in Fig.34,35. The acceptances were also obtained to normalize the ϕ meson decay angular distributions. The acceptances for different $\cos\theta$ bins and different photon energy regions were obtained for the Helicity frame (Fig.36,37) and for the Gottfried-Jackson frame (Fig.38,39). The acceptances for the azimuthal angle Φ distributions are plotted on Fig.40 for the Helicity frame and on Fig.41 for the Gottfried-Jackson frame.

To eliminate the bin migration problems, the number of energy bins and $t - t_{min}$ bins to calculate the acceptances for the cross section $t - t_{min}$ distributions were chosen to be twice the number of bins used for the data. For $\cos\Theta$ distributions the number of energy bins was also taken two times greater than the number of bins for the data, and the number of angle bins was the same as for the data. For azimuthal angle Φ distributions the number of energy bins and angle bins were the same for acceptances and for data.

	a	b	c
proton	-0.005	0	0.007
$\pi^+(\pi^-)$	- 0.000074568	0.003272231	0

TABLE II. Coefficients for energy loss momentum corrections for MC.

3.8.3 Energy Loss Momentum Corrections (for Monte Carlo)

As the particles are charged (p , π^+ , π^-), they interact electromagnetically with the material during their flight. Because of the interactions they lose a part of their energy, thus the momentum also changes. To account for this losses we must apply energy loss momentum corrections to the momenta of the reconstructed particles. To find the momentum correction functions for the particles, the $\frac{P_g - P_r}{P_r}$ versus P_r was plotted for each particle. Here P_g and P_r are the momenta of the generated and reconstructed particles, respectively. Fig.42(a),(b) and (c) show the momenta for proton, π^+ and π^- before applying the corrections. As the following step, the histograms for each particle were sliced into 30,40 momentum regions of P_r . For every region the $\frac{P_g - P_r}{P_r}$ distribution was fitted with Gauss function of three parameters (Fig.43,44,45). The mean values from the fits were plotted as function of P_r and fitted with a function $f = a + \frac{b}{P_r} + \frac{c}{P_r^2}$. On Fig.42(a),(b) and (c) the red points correspond to the mean values of $\frac{P_g - P_r}{P_r}$, and the green lines are the fits. The following a,b and c parameter values were obtained from the fits for each particle:

The reconstructed momenta after the corrections were

$$P_f = p_1 \times \left[1 + a + \frac{c}{p_1^2} \right], \quad \text{for the proton} \quad (62)$$

where $p_1 = p_i + 0.01$

$$P_f = p_i \times \left[1 + a + \frac{b}{p_i} \right], \quad \text{for pions} \quad (63)$$

where p_i is the initial reconstructed particle momentum without correction, and p_f is the momentum after the correction. Fig.42(d),(e) and (f) show the histograms

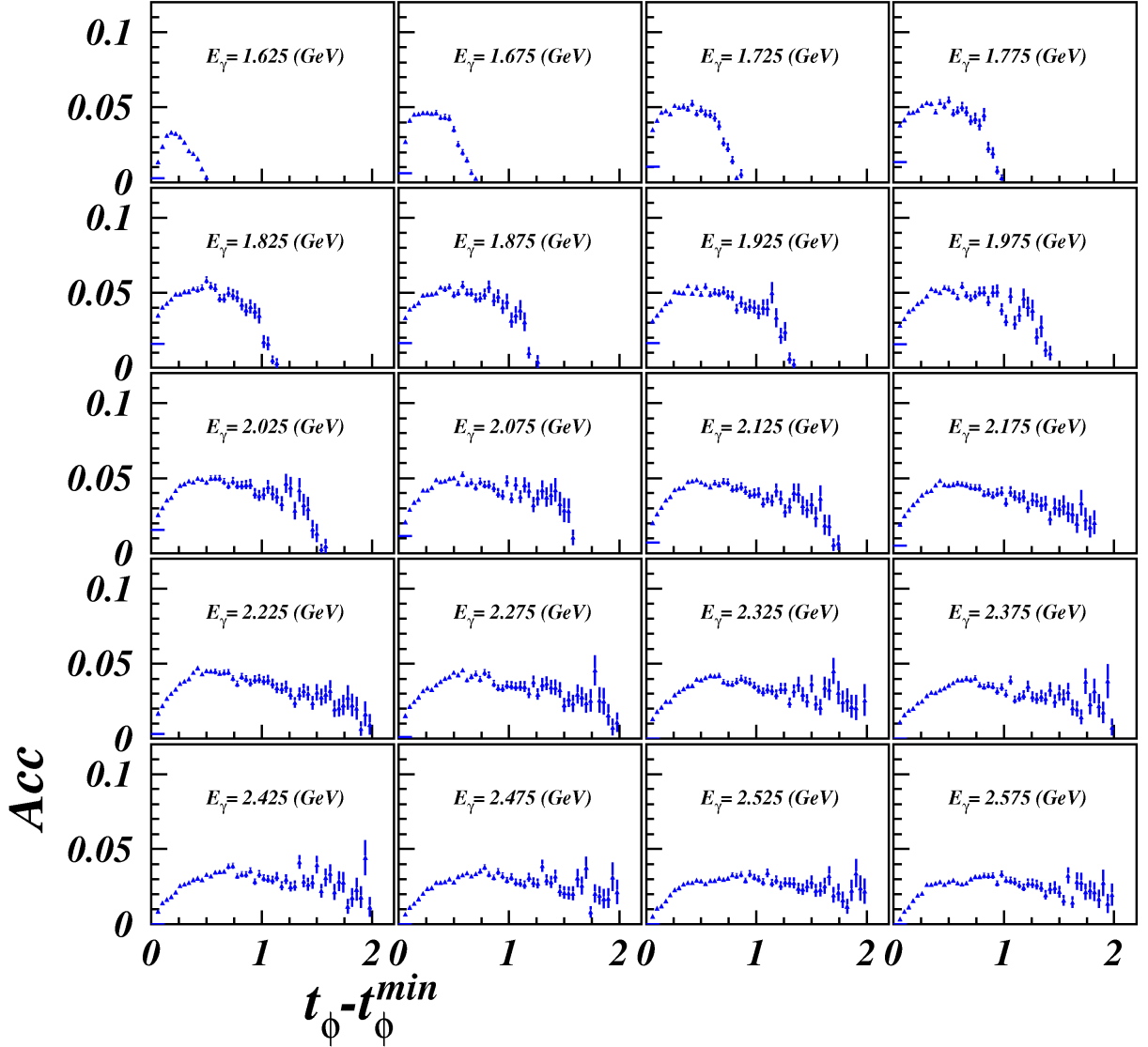


FIG. 34. Calculated acceptances for different $t - t_{min}$ bins and different photon energy regions.

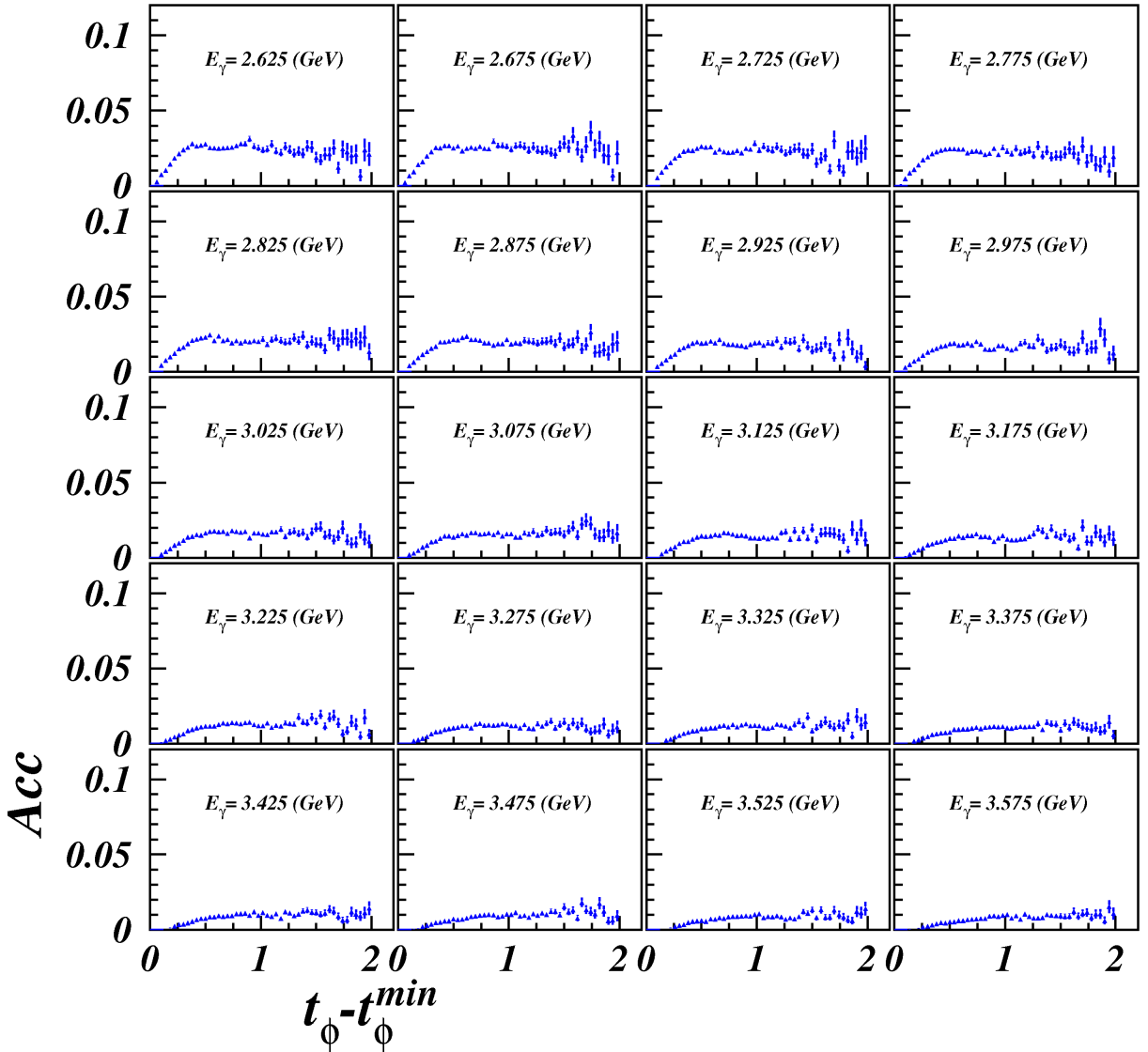


FIG. 35. Calculated acceptances for different $t - t_{min}$ bins and different photon energy regions.

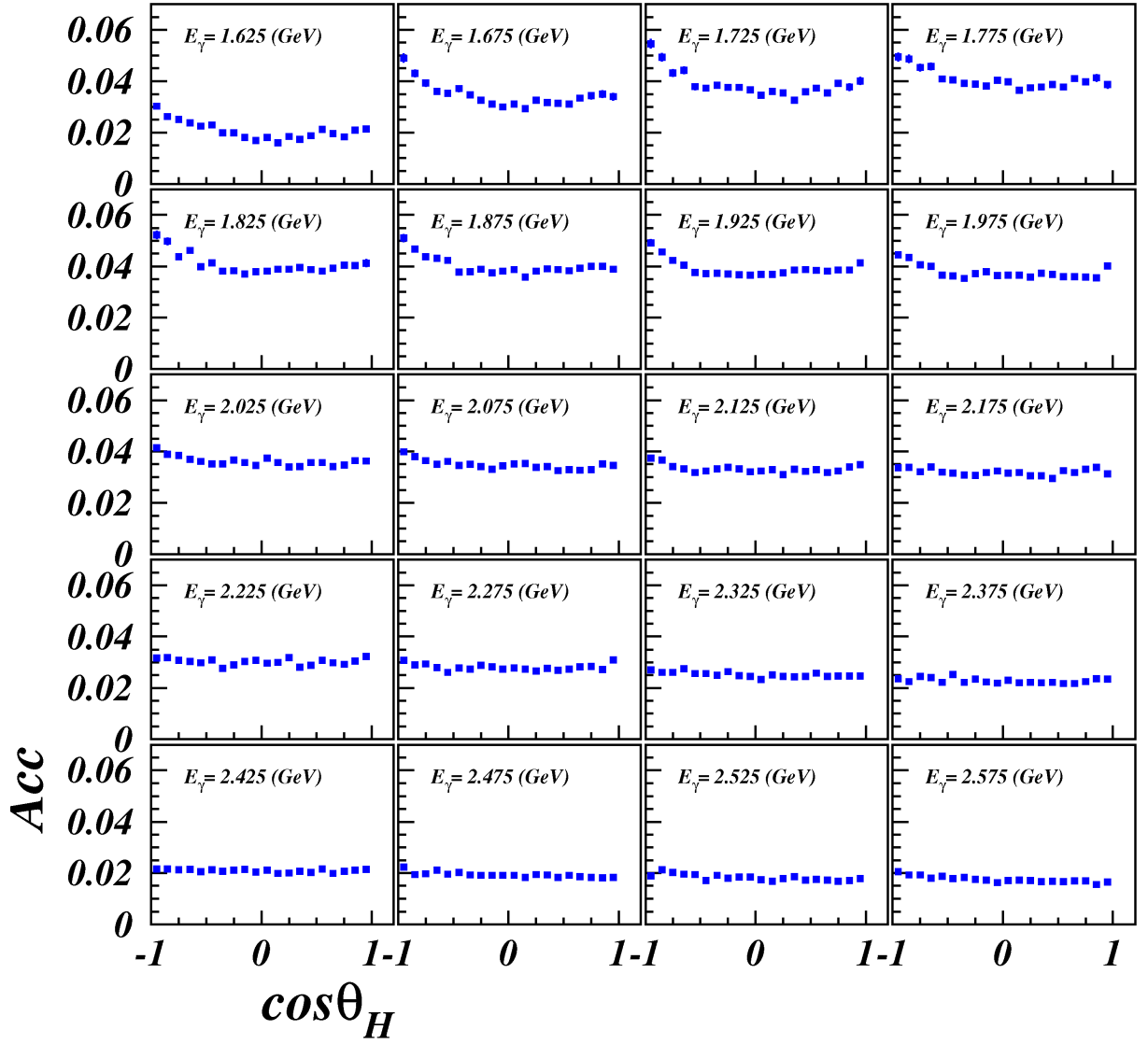


FIG. 36. Calculated acceptances for different $\cos\Theta$ bins in Helicity frame and different photon energy regions.

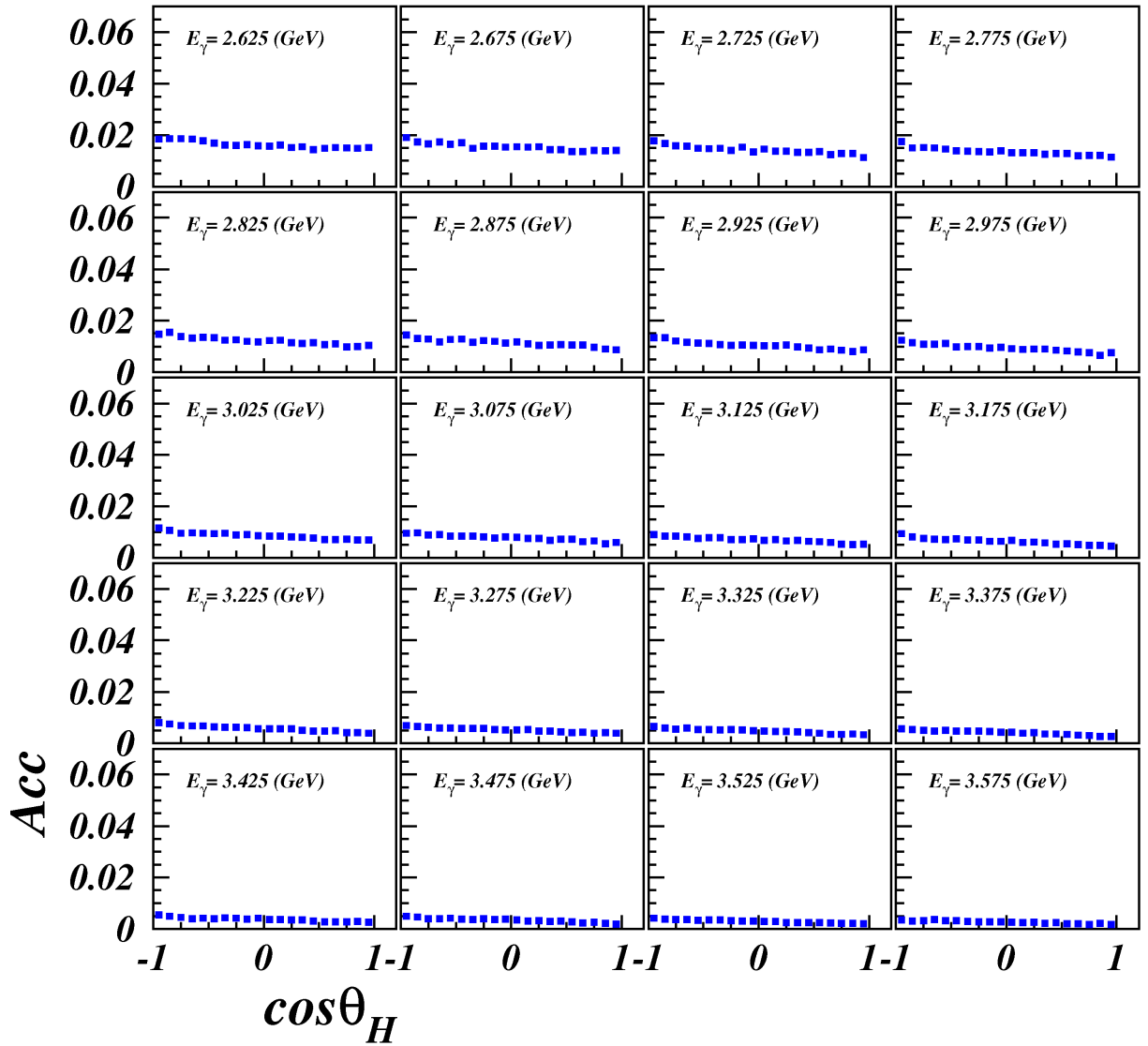


FIG. 37. Calculated acceptances for different $\cos\Theta$ bins in Helicity frame and different photon energy regions.

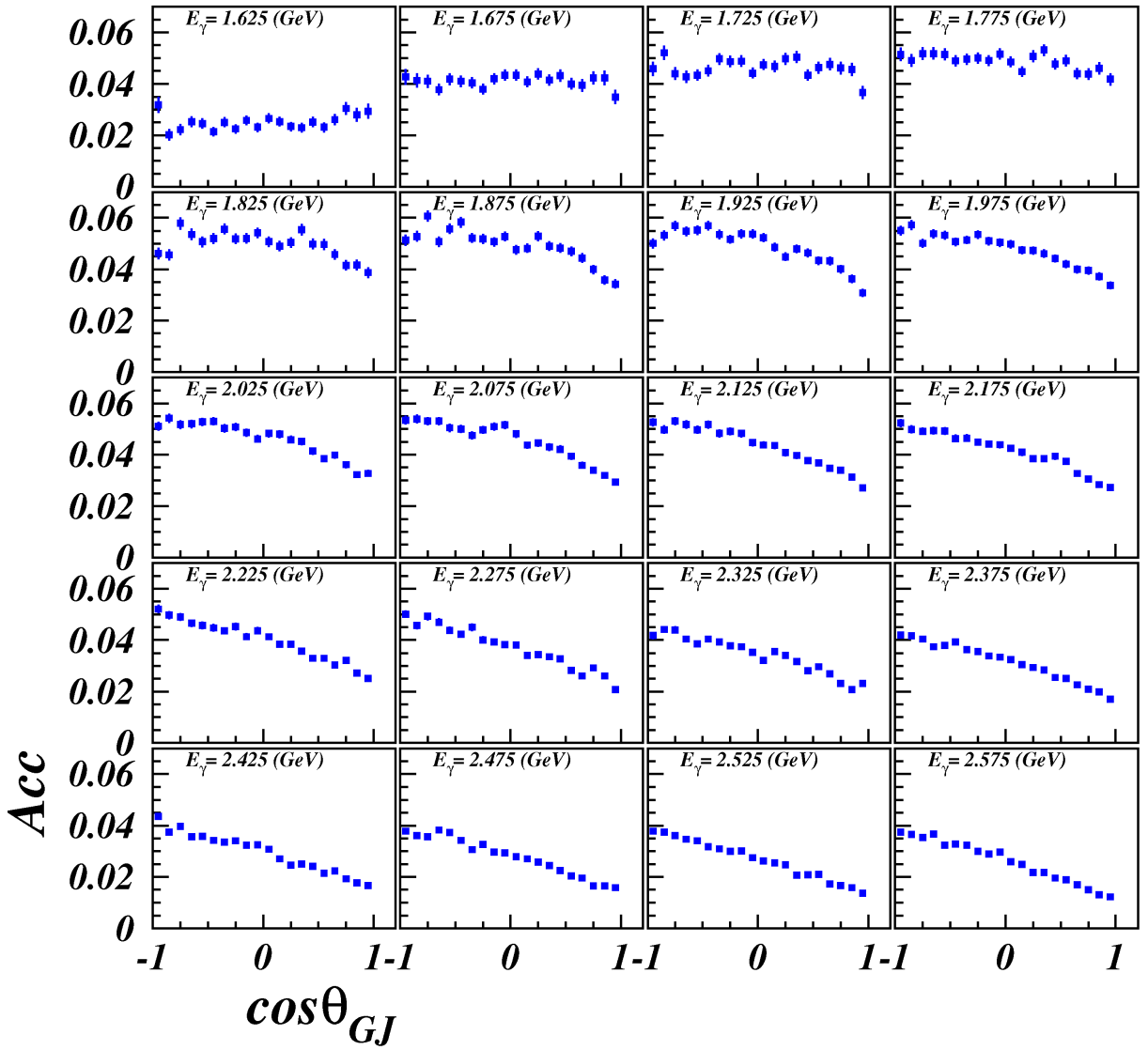


FIG. 38. Calculated acceptances for different $\cos\Theta$ bins in Gottfried-Jackson frame and different photon energy regions.

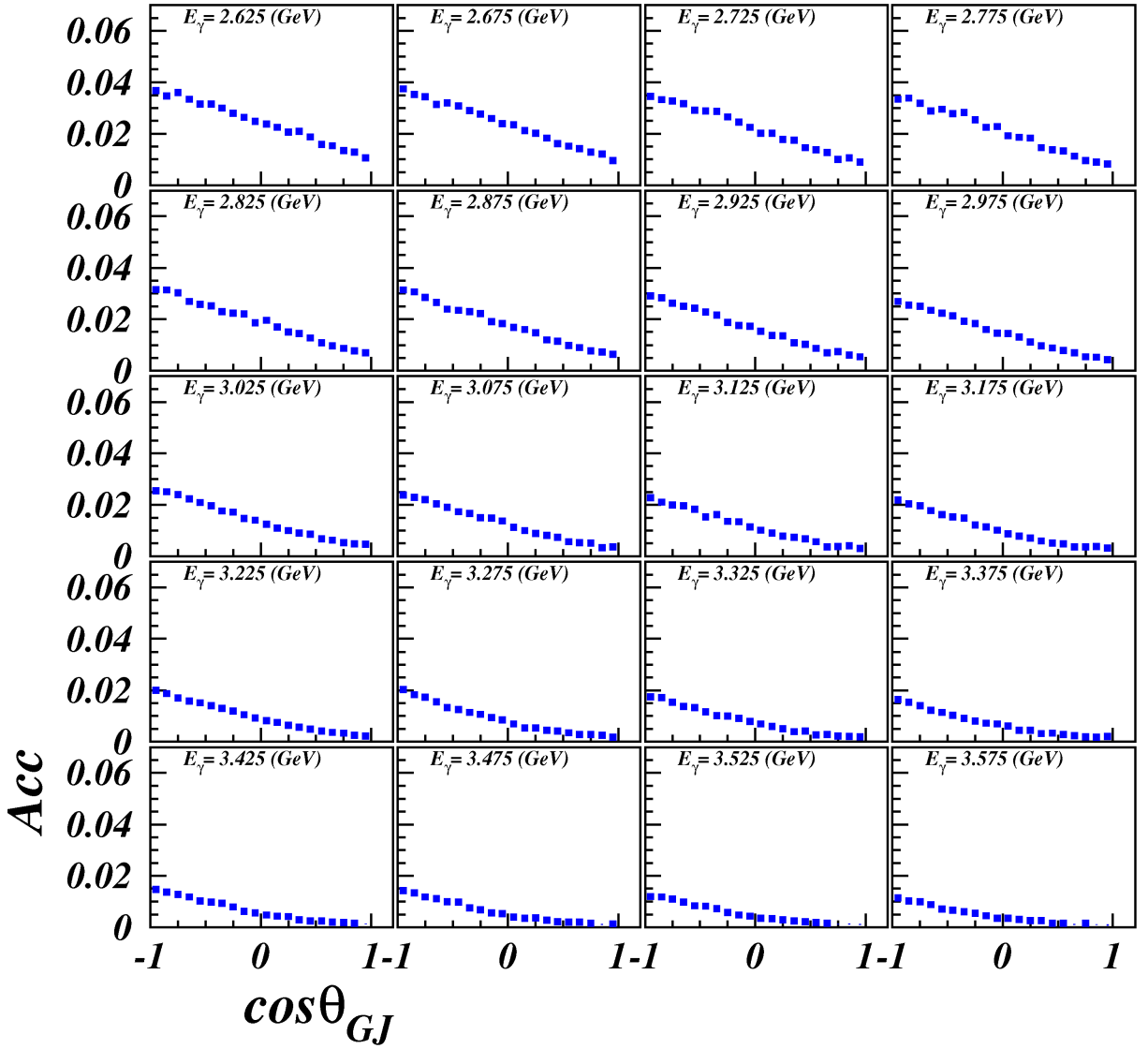


FIG. 39. Calculated acceptances for different $\cos\Theta$ bins in Gottfried-Jackson frame and different photon energy regions.

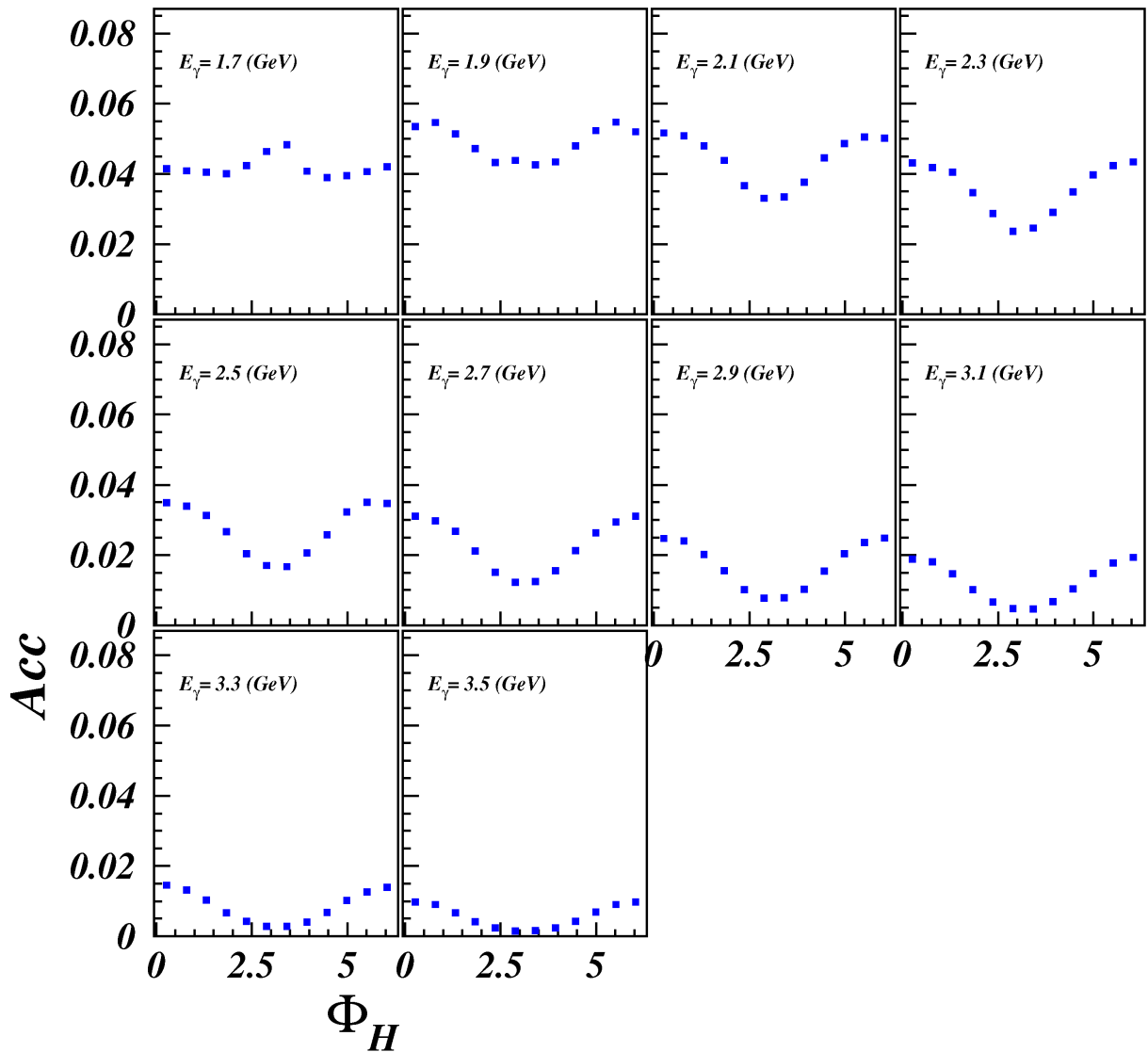


FIG. 40. Calculated acceptances for different azimuthal angle Φ bins in Helicity frame and different photon energy regions.

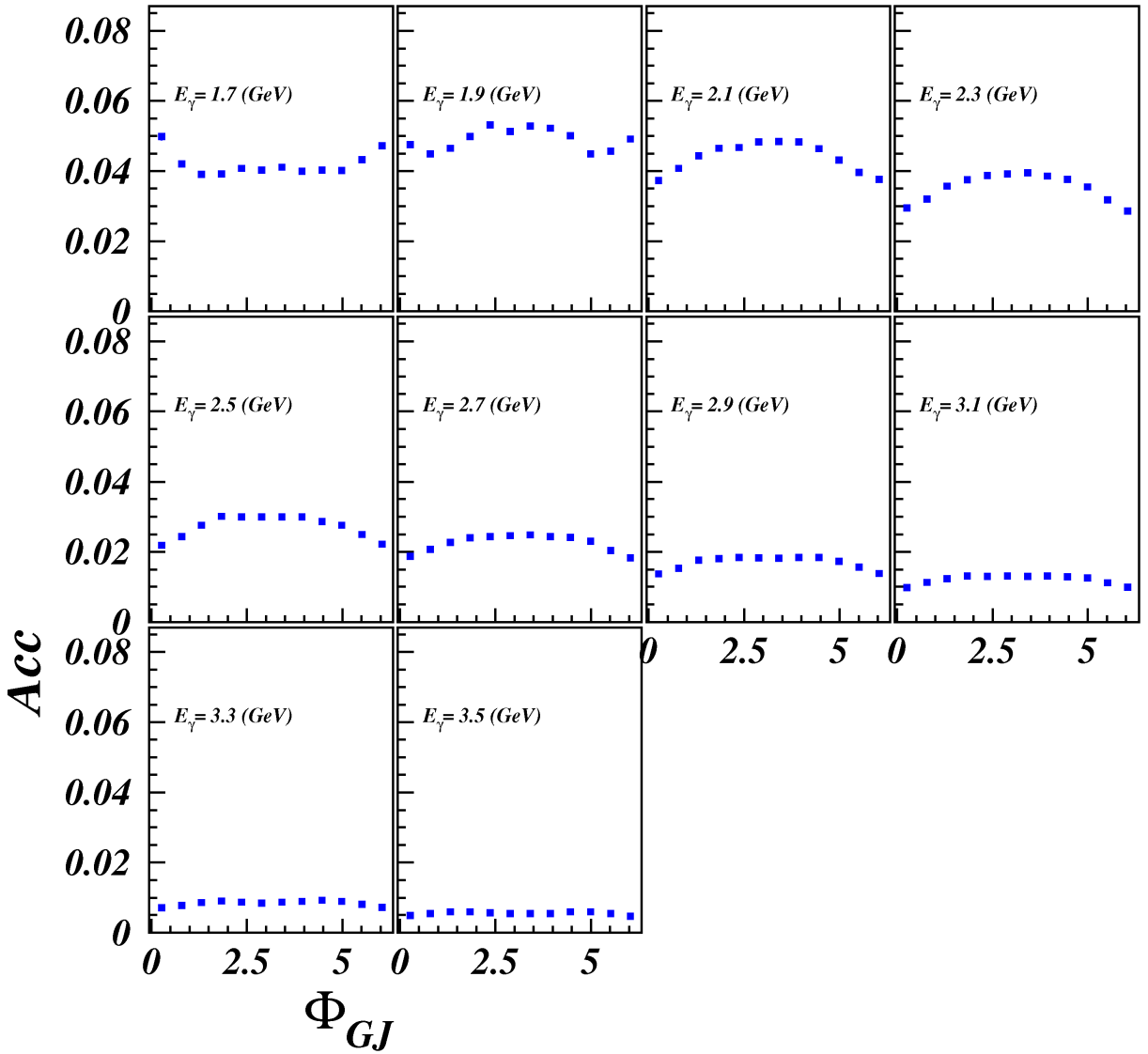


FIG. 41. Calculated acceptances for different azimuthal angle Φ bins in Gottfried–Jackson frame and different photon energy regions.

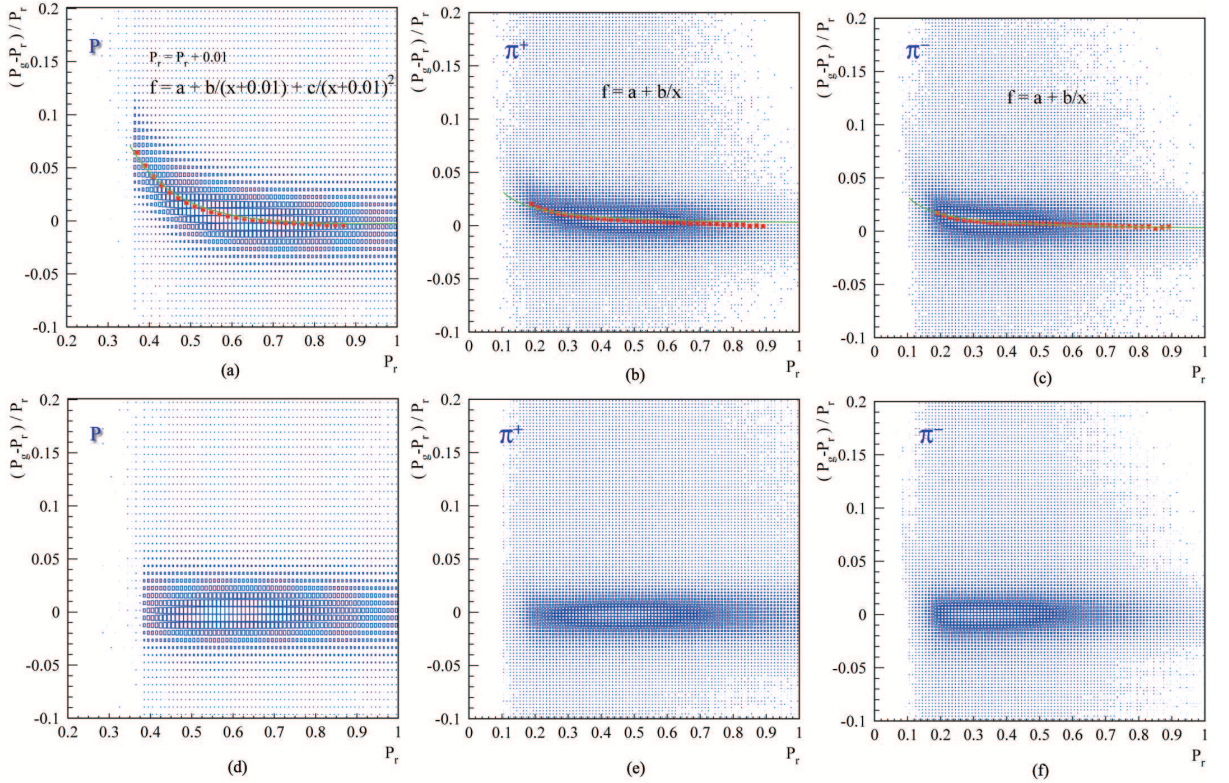


FIG. 42. $\frac{P_g - P_r}{P_r}$ versus P_r histograms for protons, π^+ and π^- mesons. (a),(b) and (c) histograms correspond to momenta dependencies before the corrections. (d),(e) and (f) are the histograms after applying the momentum corrections.

for the $\frac{P_g - P_r}{P_r}$ and P_r dependences after the corrections were applied to the momenta of the reconstructed particles.

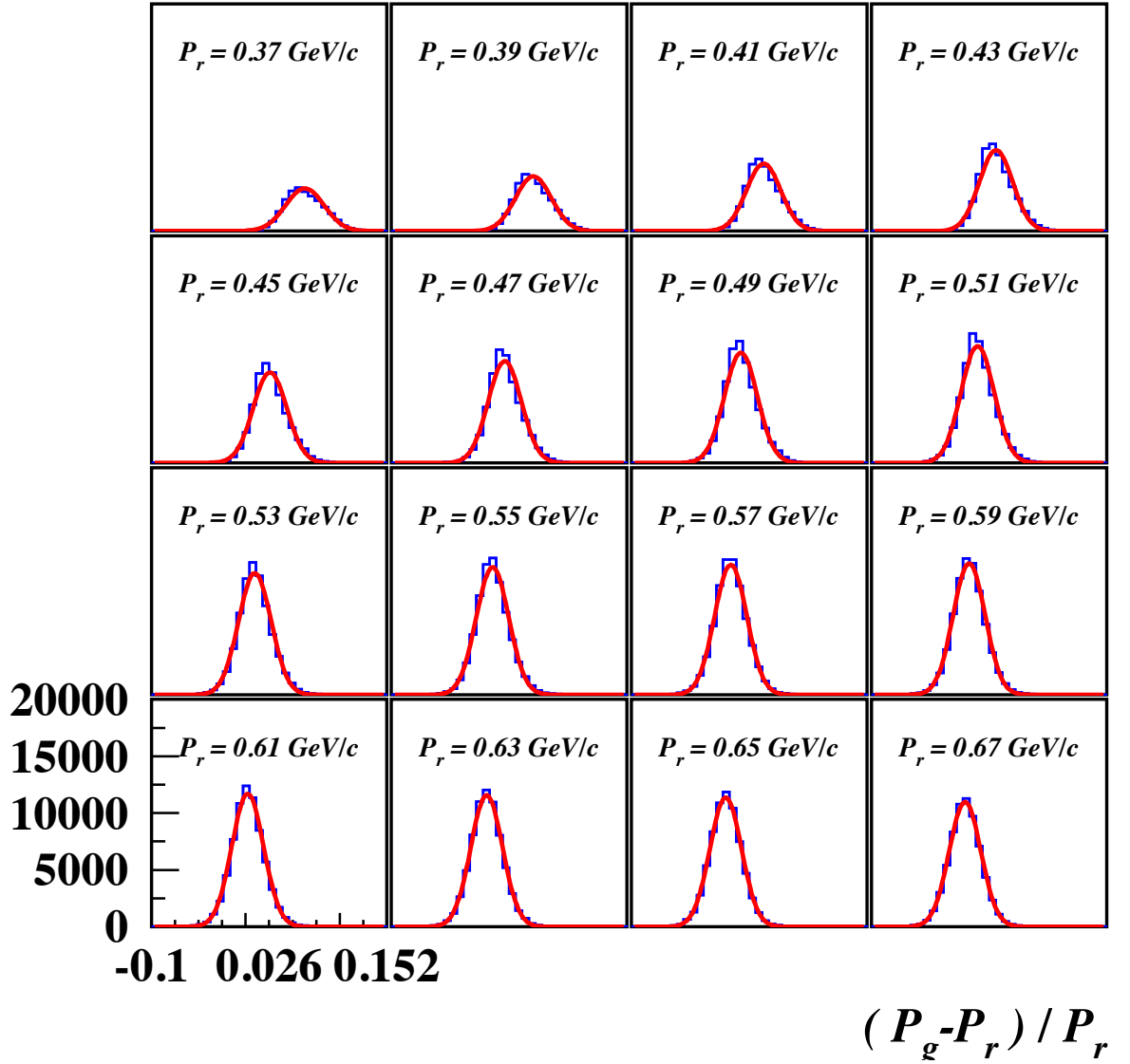


FIG. 43. Fits for protons' $P_g - P_r / P_r$ distributions in different P_r intervals by Gaussian function.

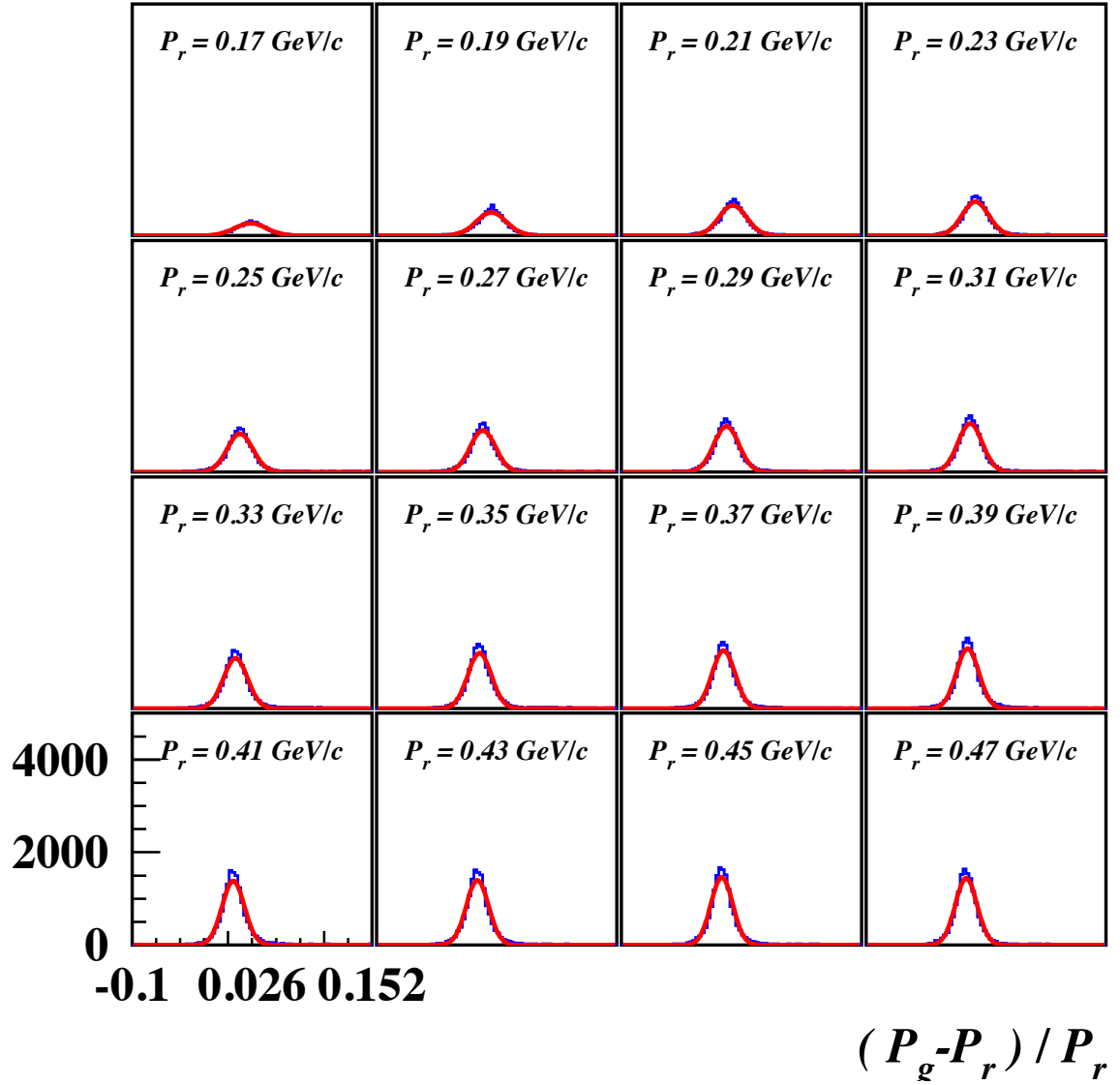


FIG. 44. Fits for π^+ mesons' $P_g - P_r/P_r$ distributions in different P_r intervals by Gaussian function.

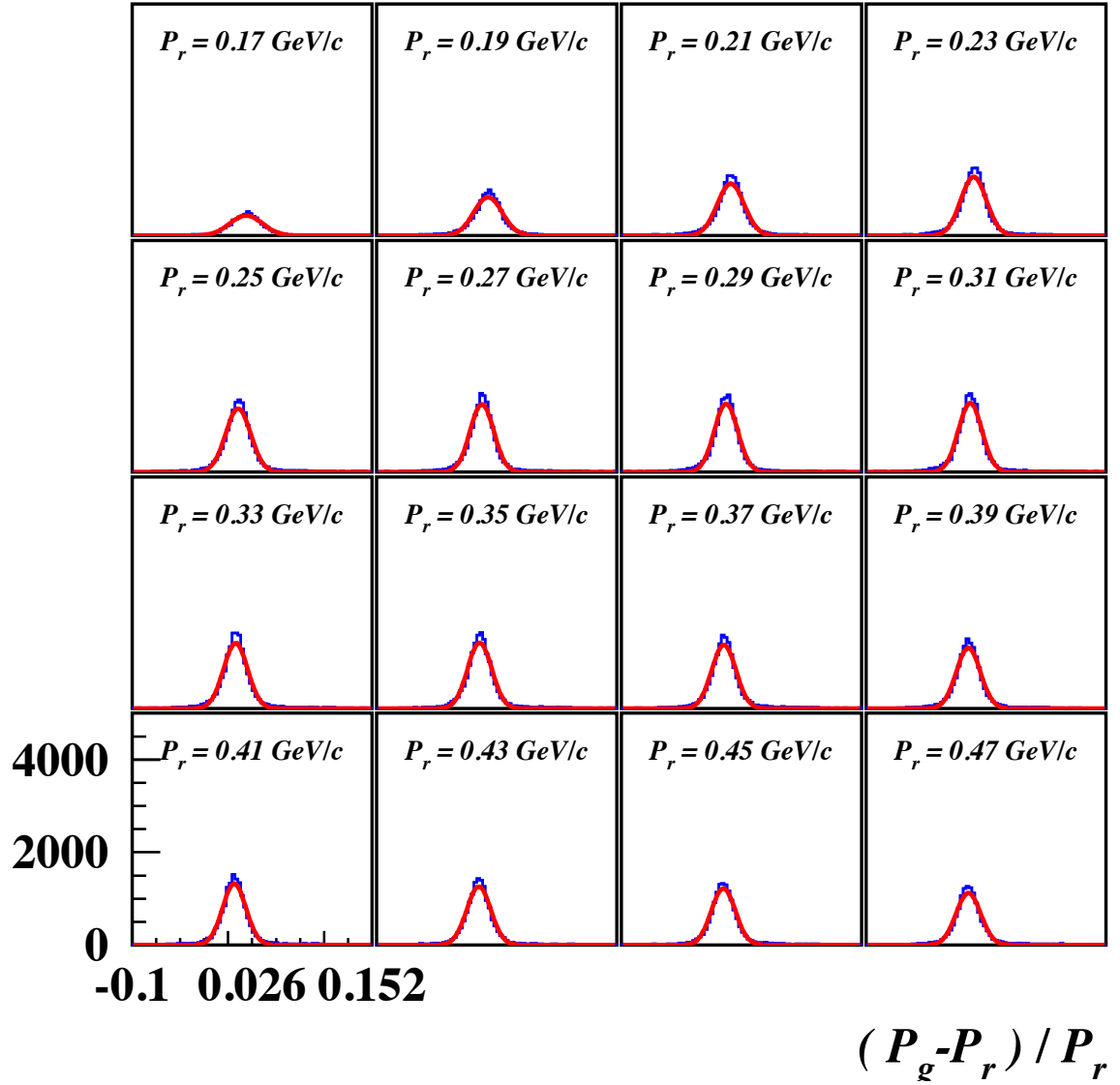


FIG. 45. Fits for π^- mesons' $P_g - P_r/P_r$ distributions in different P_r intervals by Gaussian function

Parameter	Value
a_1	$-2.89 \times 10^{-5} g/cm^3 K^2$
a_2	$1.0 \times 10^{-7} g/cm^3 mbar$
a_3	$8.249 \times 10^{-2} g/cm^3$

TABLE III. The parameter values, used to calculate liquid hydrogen target density [46].

3.8.4 Target Density

To measure the cross sections we must know the density of the target used in the experiment. For the g11 experiment liquid hydrogen target was used, the density of which can be obtained from the following expression

$$\rho = a_1 T^2 + a_2 P + a_3 \quad (64)$$

where T is the temperature, P is the pressure and the values of a_1, a_2, a_3 parameters are given in Table 3.8.4

The average target density for all g11 runs used in this analyses was approximately $0.0718 \frac{g}{cm^3}$, with variance $\sigma^2 \approx 0.678 \times 10^{-8} \frac{g^2}{cm^6}$. The relative fluctuations of the density were about 0.1%.

3.8.5 Normalization to Flux

The photon flux for the experiment was obtained using 'gflux' package of CLAS ([47]). The photon flux for each tagger T-counter and for each g11 run were obtained using the rates at which the electrons hit the given T-counter in fixed time interval. The number of the electrons hitting the T-counter was obtained taking into account the detector live time. Then the T-counter flux was used to obtain the flux for different photon energy bins ([48],[49]). There was observed some current dependence of the yeild normalization. Genova group derived a correction fitting the dependence with a line. The correction at 65 nA was 1.187. A possible explanation of the reason

for such a problem suggested by CMU group was the inaccurate estimate of DAQ dead time. The events associated to beam trips were excluded from the analysis ([50]). In Fig. 46 the photon flux is plotted as a function of photon beam energy for 50 MeV energy bins.

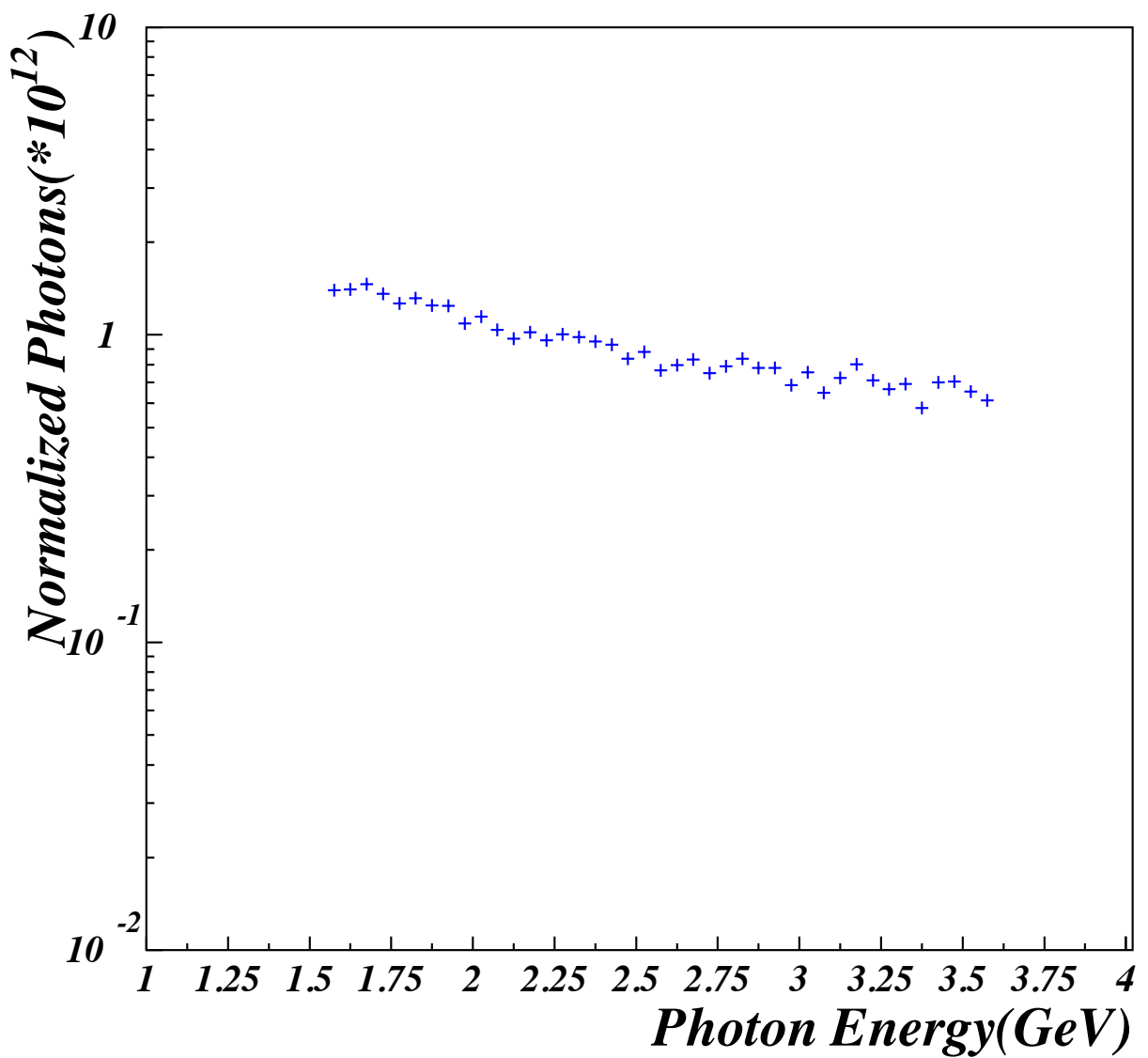


FIG. 46. Photon flux as a function of photon beam energy.

CHAPTER 4

PHYSICS RESULTS

The purpose of this analysis is to measure the differential cross sections and spin observables of ϕ meson photoproduction in 'Neutral' decay mode $\gamma + p \rightarrow p' + K_S + K_L$. In this chapter the preliminary results of the analysis will be described and compared with previous results obtained for the 'Charged' decay channel of ϕ meson $\gamma + p \rightarrow p' + K^+ + K^-$.

4.1 DIFFERENTIAL CROSS SECTIONS

In this section we present the preliminary results for the differential cross sections. In nuclear physics, the *cross section* is defined as the probability that the particular interaction will take place between particles. The differential cross section values were obtained for different $t - t_{min}$ bins and for 100 MeV photon energy bins in photon energy range 1.6-3.6 GeV. For the measurement was used the following expression for the differential cross section

$$\frac{d\sigma}{dt} = \left(\frac{A_{target}}{\mathcal{F}(E_\gamma) \rho_{target} L_{target} N_A} \right) \times \frac{\mathcal{Y}(E_\gamma, t^\phi - t_{min}^\phi)}{\Delta(t^\phi - t_{min}^\phi) \eta(E_\gamma, t^\phi - t_{min}^\phi) \mathcal{E}} \frac{1}{BR(\gamma p \rightarrow p' K_S K_L)}$$

Here N_{target} , ρ_{target} and L_{target} are the atomic weight, density and the length of the target, respectively. N_A is the Avogadro number and $\mathcal{F}(E_\gamma)$ is the total number of the photons incident on target in given photon energy bin. $\Delta(t^\phi - t_{min}^\phi)$ is the $t^\phi - t_{min}^\phi$ bin size, which was selected to be 0.08. $BR \approx 0.34$ is the branching ratio of the ϕ meson production in Neutral channel. $\mathcal{Y}(E_\gamma, t^{phi} - t_{min}^{phi})$ is the data signal yield in given photon energy and $t^\phi - t_{min}^\phi$ bin , after the background subtraction (

see 3.7). $\eta(E_\gamma, t^\phi - t_{min}^\phi)$ is the acceptance in $(E_\gamma, t^\phi - t_{min}^\phi)$ bin (see 3.8.2) and \mathcal{E} is the efficiency for every data event in the given bin (3.3).

There was a cut applied to acceptance to be $\eta(E_\gamma, t^\phi - t_{min}^\phi) < 0.001$.

Fig.47 shows the preliminary results for the $|t - t_{min}|$ dependence of differential cross section $d\sigma/dt$ for 100 MeV wide photon energy bins in energy range 1.6-3.6 GeV. At lower values of the four momentum transfer the cross section drops exponentially with $|t - t_{min}|$. This is expected by the ruling Pomeron exchange mechanism of ϕ meson photoproduction in this regime. At higher values of t there is observed some local increase and drop in differential cross section that distorts the exponential behavior. This might be because of N/N^* exchange contributions in the cross section. We did not include the data for the first bin of very low t , because of problems related to GSIM to describe this forward angle region of the detector.

Fig.48 presents the preliminary results for the differential cross section $d\sigma/d\cos\theta_{c.m.}$ plotted as a function of $\cos\theta_{c.m.}$, where $\theta_{c.m.}$ is the ϕ meson polar angle in center-of-mass system of $\gamma p \rightarrow \phi p$. The results are plotted for 100 MeV photon energy bins in 1.6-3.6 GeV range. The bin size of x axis is 0.1.

Fig.49 and 50 show the \sqrt{s} dependence of the differential cross section $d\sigma/dt$ in different $\cos\theta_{c.m.}^\phi$ bins. First, $d\sigma/dt$ was measured at different photon energies E_γ (for 50 MeV wide bins of E_γ in 1.6-3.6 GeV energy range), then the result was plotted as a function of s, converting E_γ into \sqrt{s} with $s = M_p^2 + 2M_pE_\gamma$ relation ($M_p = 0.93828$ is the proton mass). The cross sections were measured using the following relation:

$$\frac{d\sigma}{dt} = \frac{1}{2} \left(\frac{1}{E_\gamma |\vec{p}_\phi|} \right)_{c.m.} \left(\frac{d\sigma}{d\cos\theta_{c.m.}^\phi} \right) \quad (65)$$

The results for the forward angles or low t region may not be reliable because GSIM does not describe this region well.

Fitting the $|t - t_{min}|$ dependence of the differential cross section $d\sigma/dt$ with an exponential function of $Ae^{-\beta|t-t_{min}|}$ from the differential cross section at $t = t_{min}$ point (fig. 51(a)) and the β slopes of the $|t - t_{min}|$ distributions (fig. 51(b)) were measured for 100 MeV wide energy bins in 1.6-3.6 GeV range. The differential cross section still has some local structure at about 1.8-2.4 GeV as the one observed in 'Charged' decay mode, although in this case the peak is smaller. The slope also has

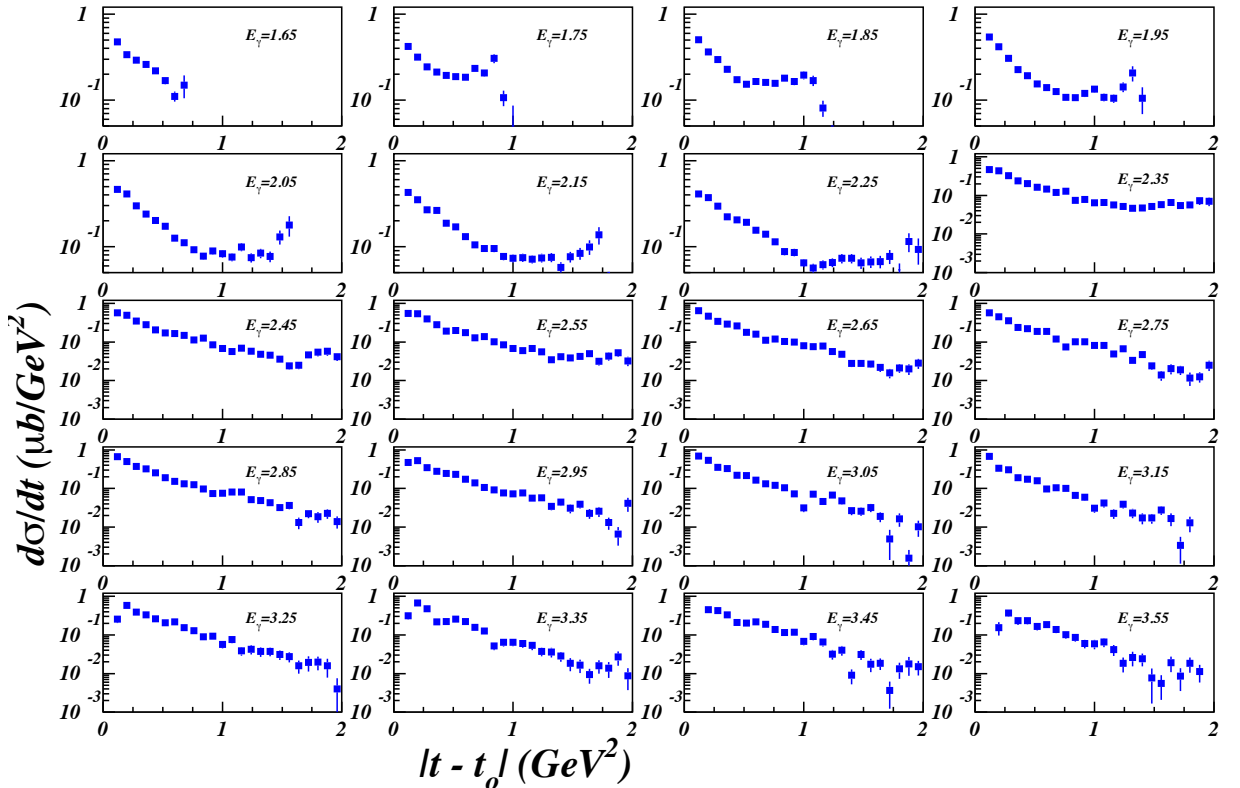


FIG. 47. The $|t - t_{min}|$ dependence of the ϕ meson differential cross section $d\sigma/dt$ in different photon beam energy bins of 1.6-3.6 GeV energy range.

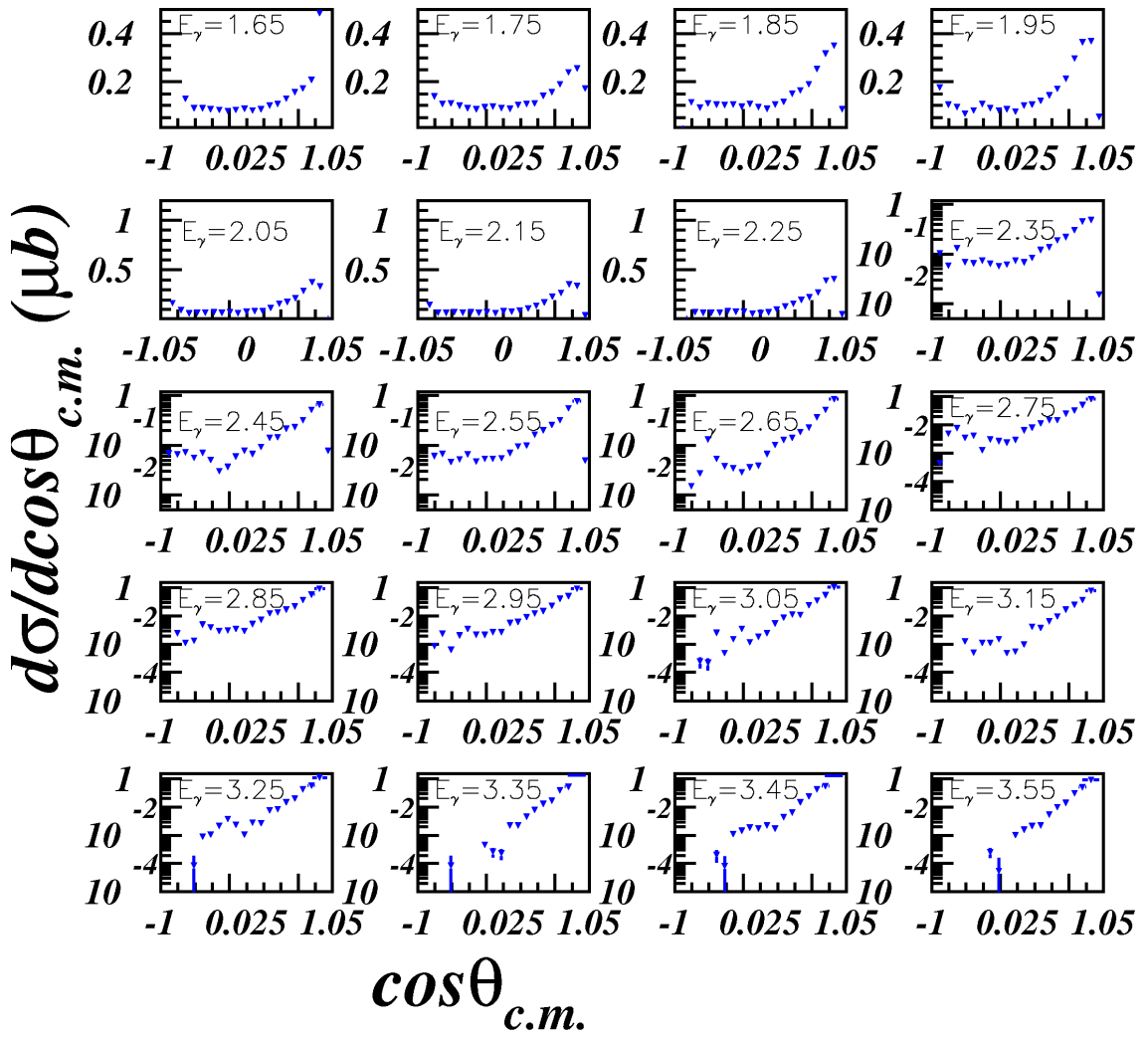


FIG. 48. The $\cos\theta_{c.m.}^\phi$ dependence of the ϕ meson differential cross section $d\sigma/d\cos\theta_{c.m.}$ for different photon beam energy bins of 1.6-3.6 GeV energy range.

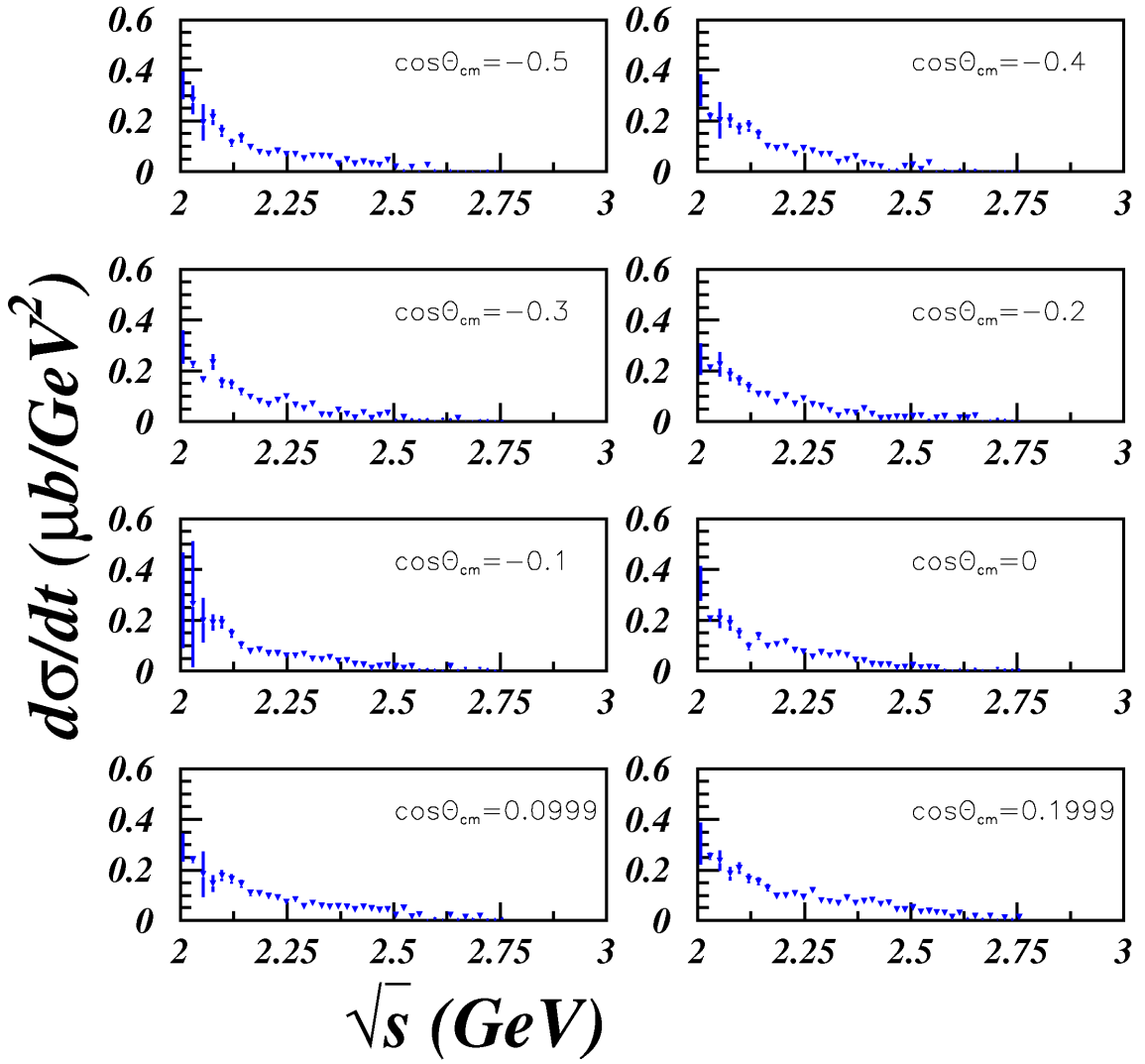


FIG. 49. The \sqrt{s} dependence of the ϕ meson differential cross section $d\sigma/dt$ in different $\cos\theta_{c.m.}$ bins for $-0.55 < \cos\theta_{c.m.} < 0.25$ range.

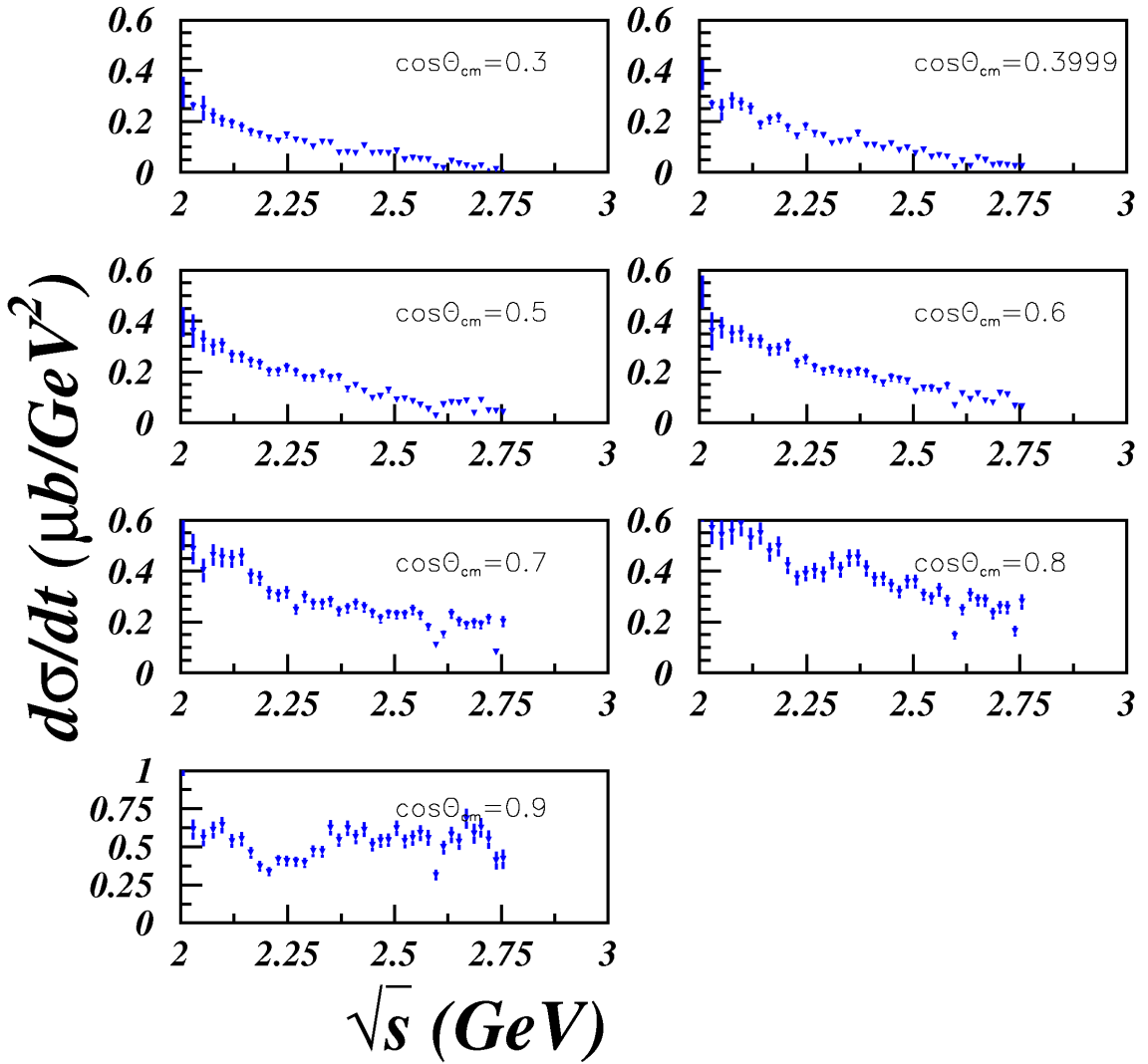


FIG. 50. The \sqrt{s} dependence of the ϕ meson differential cross section $d\sigma/dt$ in different $\cos\theta_{c.m.}$ bins for $0.25 < \cos\theta_{c.m.} < 0.95$ range.

some local enhancement in the energy range of 1.6-2.3 GeV. These results strongly depend on the fit region of $t - t_{min}$ distribution of the cross section. The higher t regions, where the cross sections increase and deviate from exponential behavior, were not included in fits.

All presented cross section results were measured with a 40% efficiency cut. The uncertainty in results following from this cut was included in systematic errors that were calculated using a set of various efficiency cuts(see 4.3).

4.2 ANGULAR DISTRIBUTION FUNCTIONS AND SPIN OBSERVABLES

For unpolarized beam the $\phi \rightarrow K_S K_L$ decay angular distribution in the rest frame of ϕ meson is described as a function of polar(Θ) and azimuthal(Φ) angles by equation (17). Below we present the decay angular distribution of $\phi(1020)$ meson in polar and azimuthal angles and spin-density matrix element ρ^0 measured for Neutral decay channel of ϕ in two frames - Helicity and Gottfried-Jackson (see 2.2).

Fig. 52 shows the decay angular distribution of ϕ as a function of polar angle Θ in Helicity frame for 100 MeV wide photon energy bins. The binning size of the x axis is 0.1. The decay has quadratic dependence on $\cos\Theta$ function in all bins.

Fig. 53 describes the decay angular distribution of ϕ as a function of polar angle Θ in Gottfried-Jackson frame with a cut $-0.2 < t + |t|_{min}$. The bin sizes are kept the same as for the Helicity frame. The green points in 2.2-2.4 GeV energy interval are the results of LEPS collaboration (SPring-8) analysis [2]. The current analysis distribution is much different from the LEPS result in the two bins. The $\cos^2\Theta$ dependence of the decay distribution at lower energies bends towards the backward angles as the energy grows. This could be an artificial effect coming from the frame rotations (from Helicity to GJ), or this might be due to the possible interference of S and P waves or signal-background interference.

Fig. 54 and 55 show the ϕ meson decay distributions in azimuthal angle Φ in Helicity and GJ frames. In both cases $-0.2 < t + |t|_{min}$ cut was applied on four

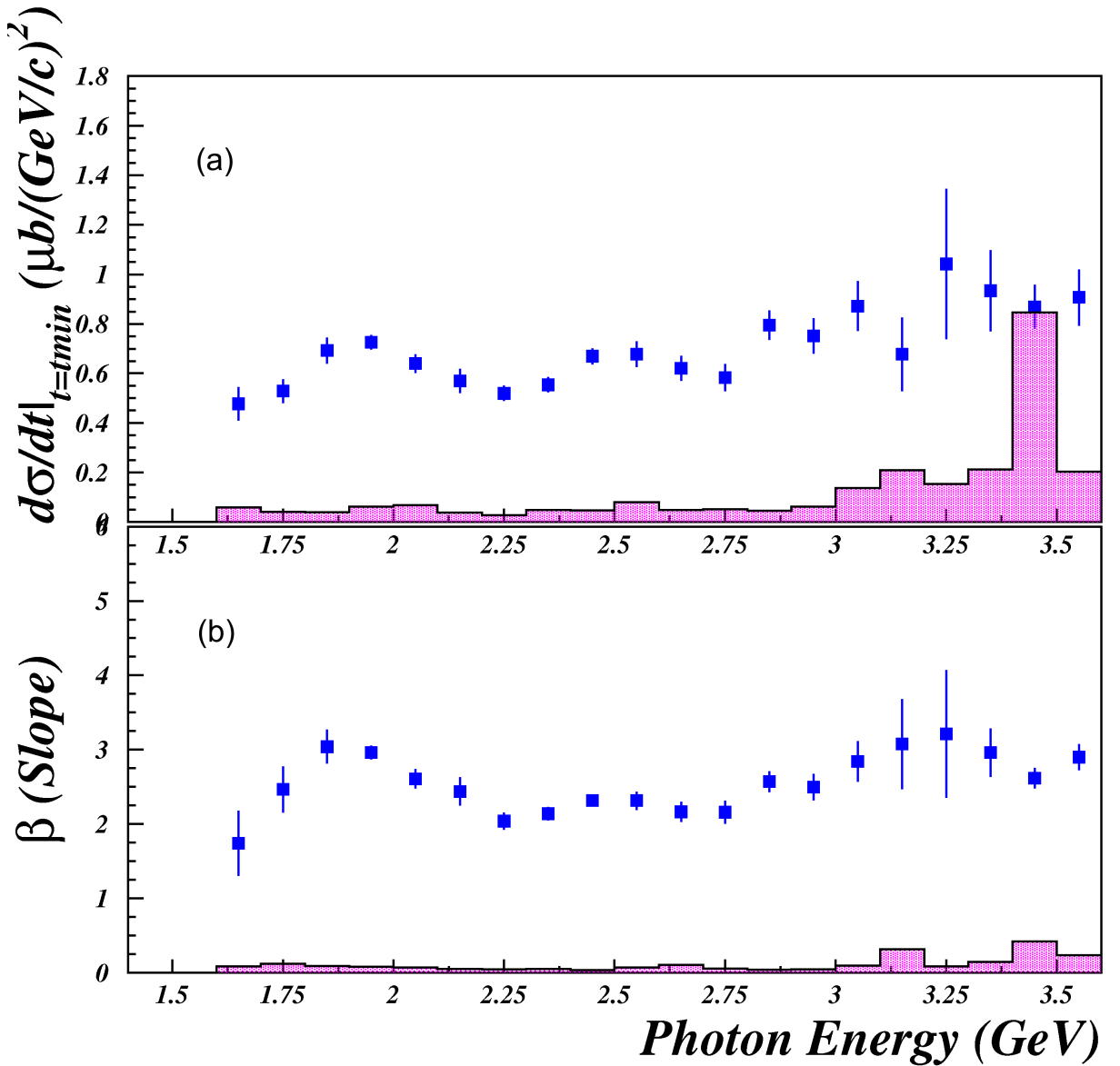


FIG. 51. Differential cross section $d\sigma/dt$ at $t = t_{min}$ (a) and ϕ meson photoproduction slope β (b) for the Neutral decay channel plotted as functions of photon beam energy E_γ in 1.6-3.6 GeV energy range. The error bars represent the statistical errors, errors of the flux calculation, efficiency error at 40% efficiency cut, acceptance errors. The systematic errors are included as dashed pink regions at horizontal axis.

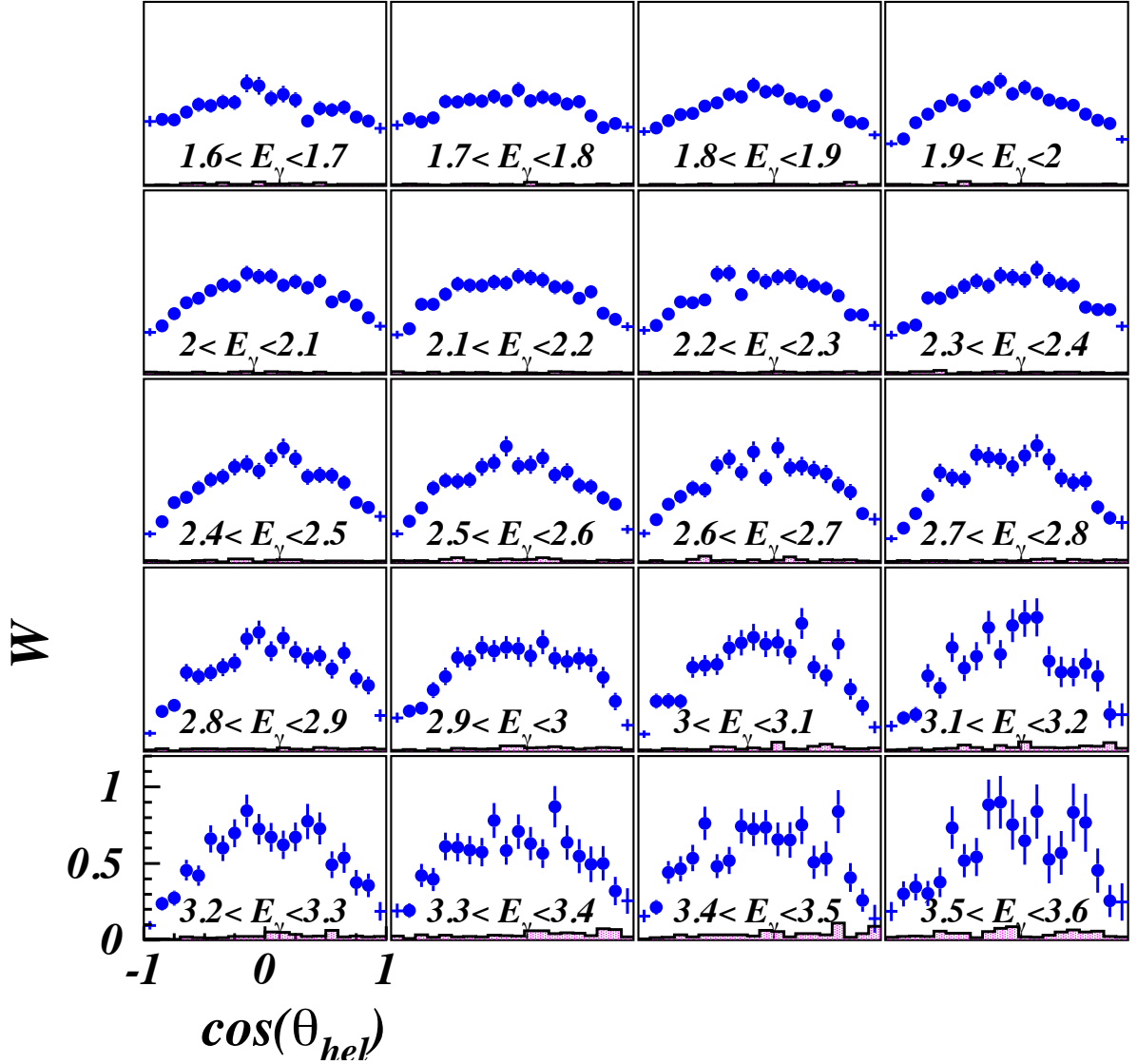


FIG. 52. The decay distribution of ϕ meson as a function of polar angle Θ in Helicity frame for the 'neutral' decay channel of $\phi(1020)$ meson.

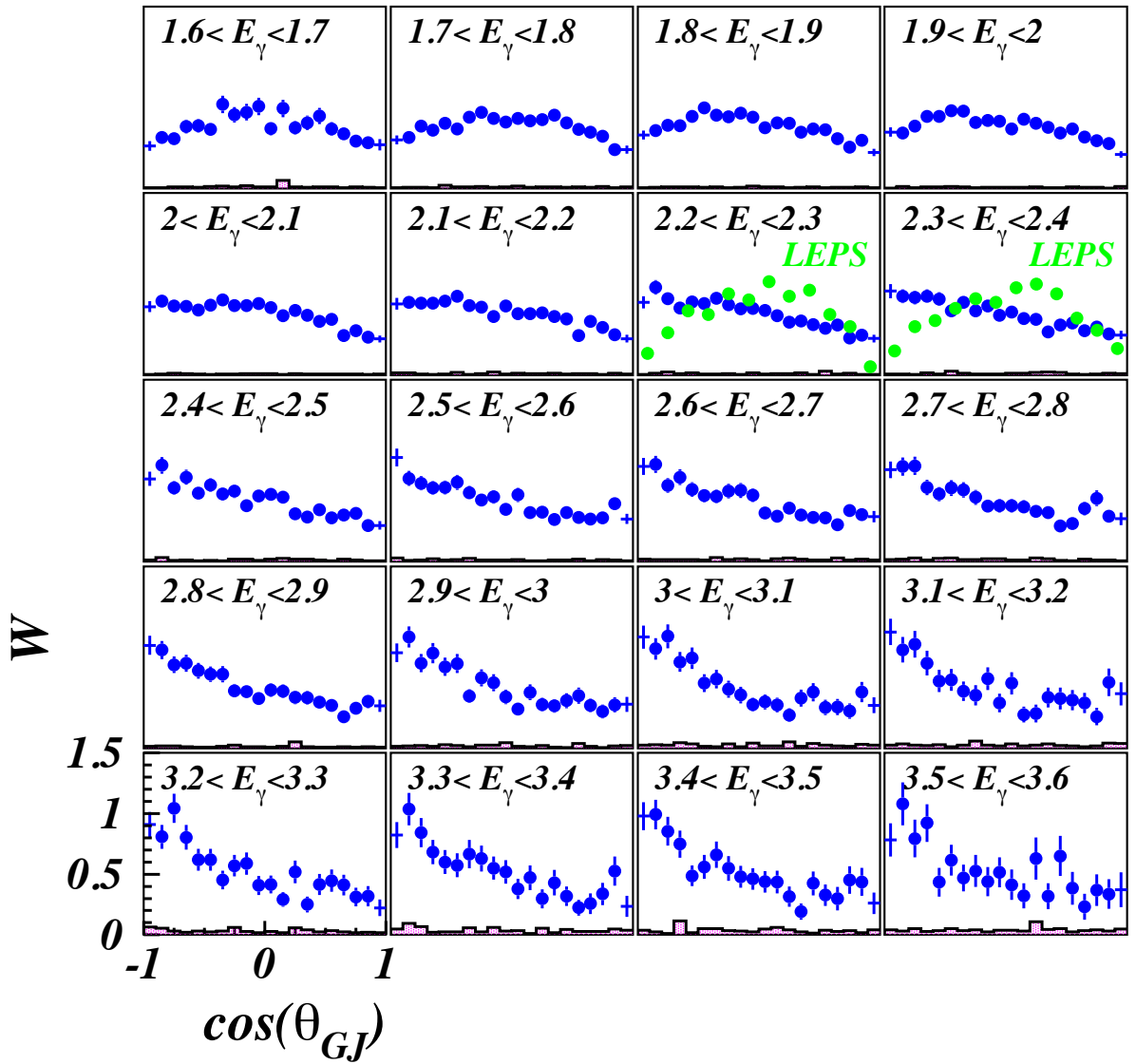


FIG. 53. The decay distribution of ϕ meson as a function of polar angle Θ in Gotfri-d Jackson frame for the 'neutral' decay channel of $\phi(1020)$ meson.

momentum transfer. The distributions are measured for 200 MeV wide energy bins in 1.6-3.6 GeV photon energy interval. The Φ angle is converted to radians and the x axis has 12 bins in (0-6.3) interval. In fig.55 the green points in two energy bins correspond to LEPS results for the charged decay channel of ϕ [2]. There is agreement between the distributions measured by LEPS and the current analysis result for this energy interval.

The spin-density matrix element components ρ_{00}^0 and ρ_{1-1}^0 were measured for different photon energies from the fits of polar and azimuthal angle dependence parts of decay distributions. For Helicity frame ρ_{00}^0 was obtained fitting figure 52 distributions with $a[1 - b + (3b - 1)x^2]$ function and ρ_{1-1}^0 was extracted fitting the decay distributions in azimuthal angle (fig. 54) with function $a(1 - 2b \cos 2x)$ (see fig. 56). To be able to extract the ρ_{00}^0 in GJ frame we had to modify the fit function for the Helicity frame adding a linear term. In GJ frame the ρ_{00}^0 was measured fitting fig. 53 distributions with $a[1 - b + (3b - 1)x^2 + cx]$ function. The ρ_{1-1}^0 component in GJ frame was measured fitting fig.55 distributions with the same function as for the Helicity frame. Figure 57 shows this analysis results for ρ_{00}^0 and ρ_{1-1}^0 as functions of photon beam energy E_γ in GJ frame. In both frames the ρ_{00}^0 components are much higher than the ρ_{1-1}^0 components, which is expected by theory (see fig. 13 in 2.5.2).

4.3 SYSTEMATIC UNCERTAINTIES

In every analysis some systematic errors exist due to some cuts, corrections, calibration, algorithms. This section describes which systematic errors were included and how they were estimated for the current analysis. Below is the list of estimated systematic errors and the description of how they were obtained.

- Systematic errors due to background separation. As described in (3.7) the background of the ϕ meson signal was selected as $M(\phi) = 1/2 * N(1.06 \pm 0.02(GeV/c^2))$. We selected the half of the background events in the selected interval because of uneven distribution of the background in the left and in

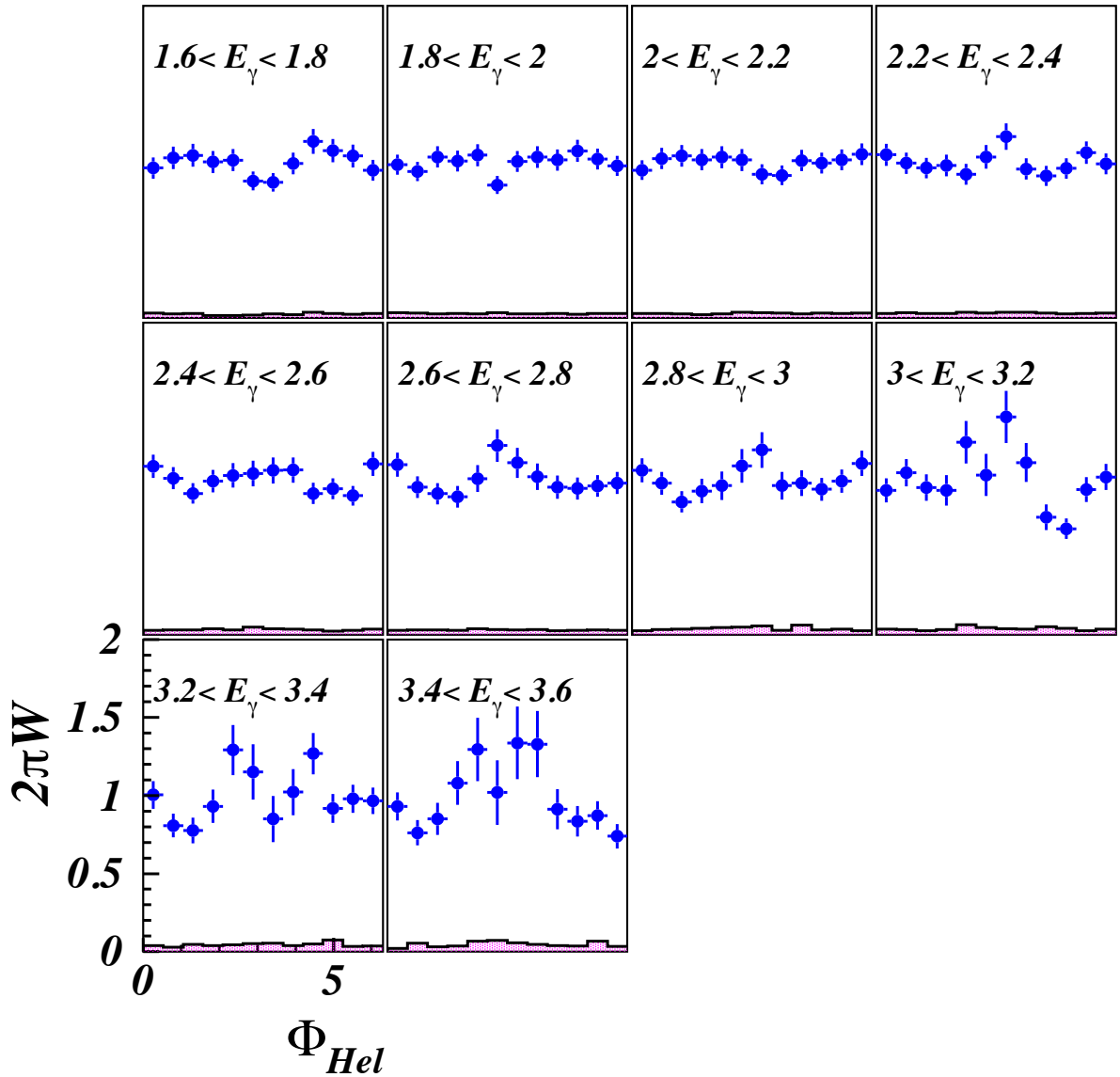


FIG. 54. The decay distribution of ϕ meson as a function of azimuthal angle Φ in Helicity frame for the 'neutral' decay channel of $\phi(1020)$ meson.

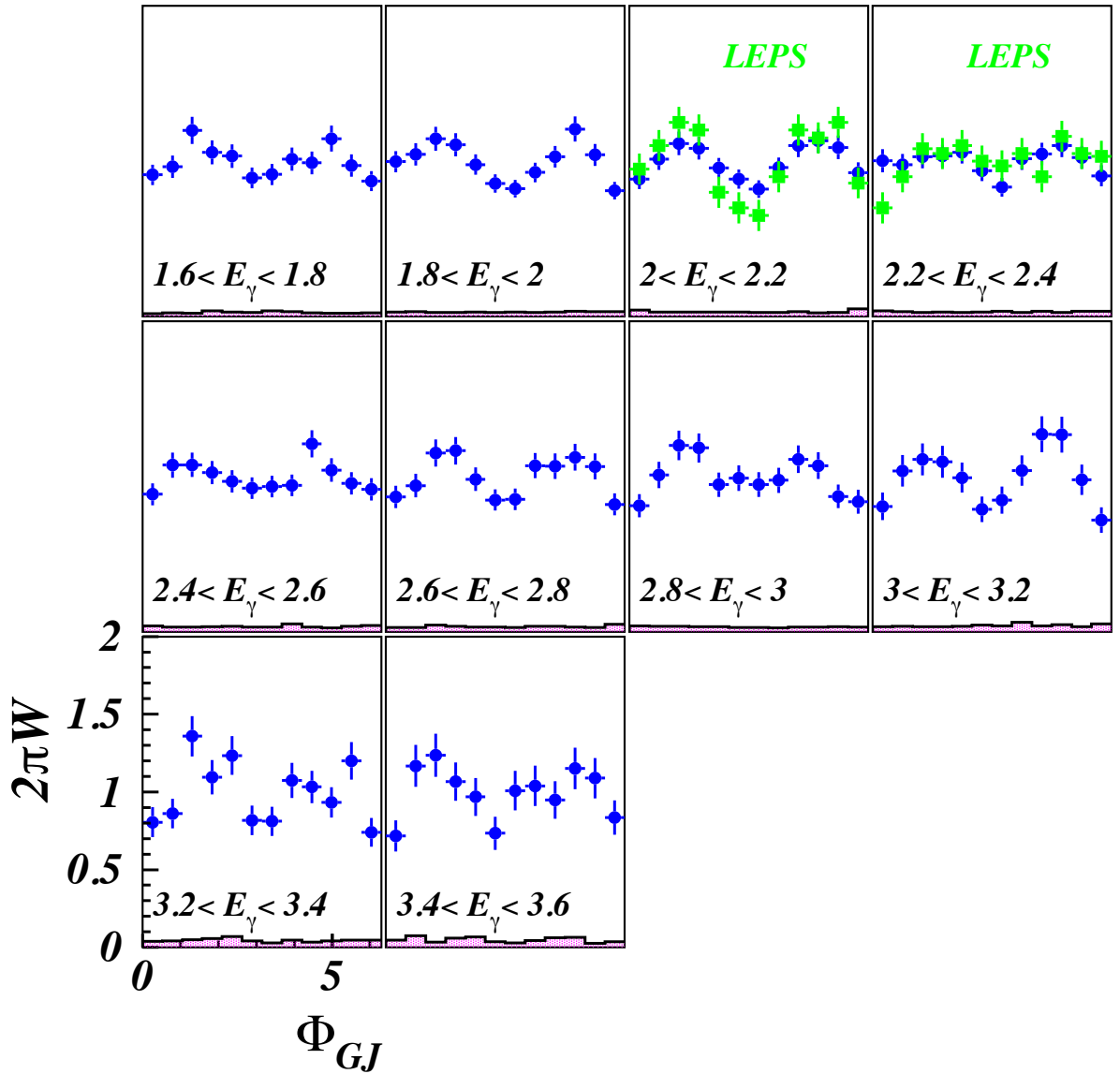


FIG. 55. The decay distribution of ϕ meson as a function of azimuthal angle Φ in Gottfried-Jackson frame for the 'neutral' decay channel of $\phi(1020)$ meson.

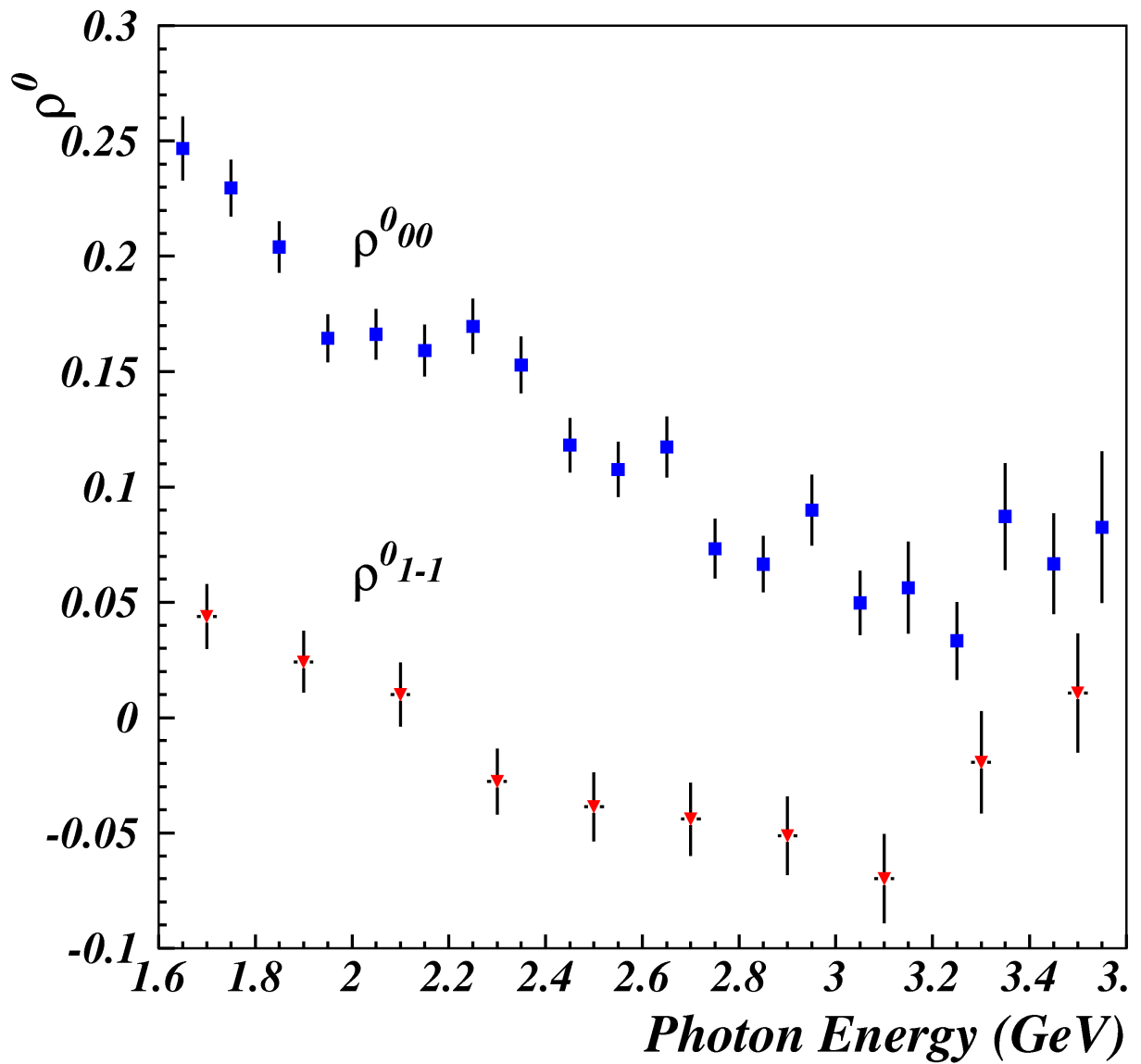


FIG. 56. Spin-density matrix element components ρ_{00}^0 (blue) and ρ_{1-1}^0 (red) for different photon beam energies in 1.6-3.6 GeV range in Helicity frame.

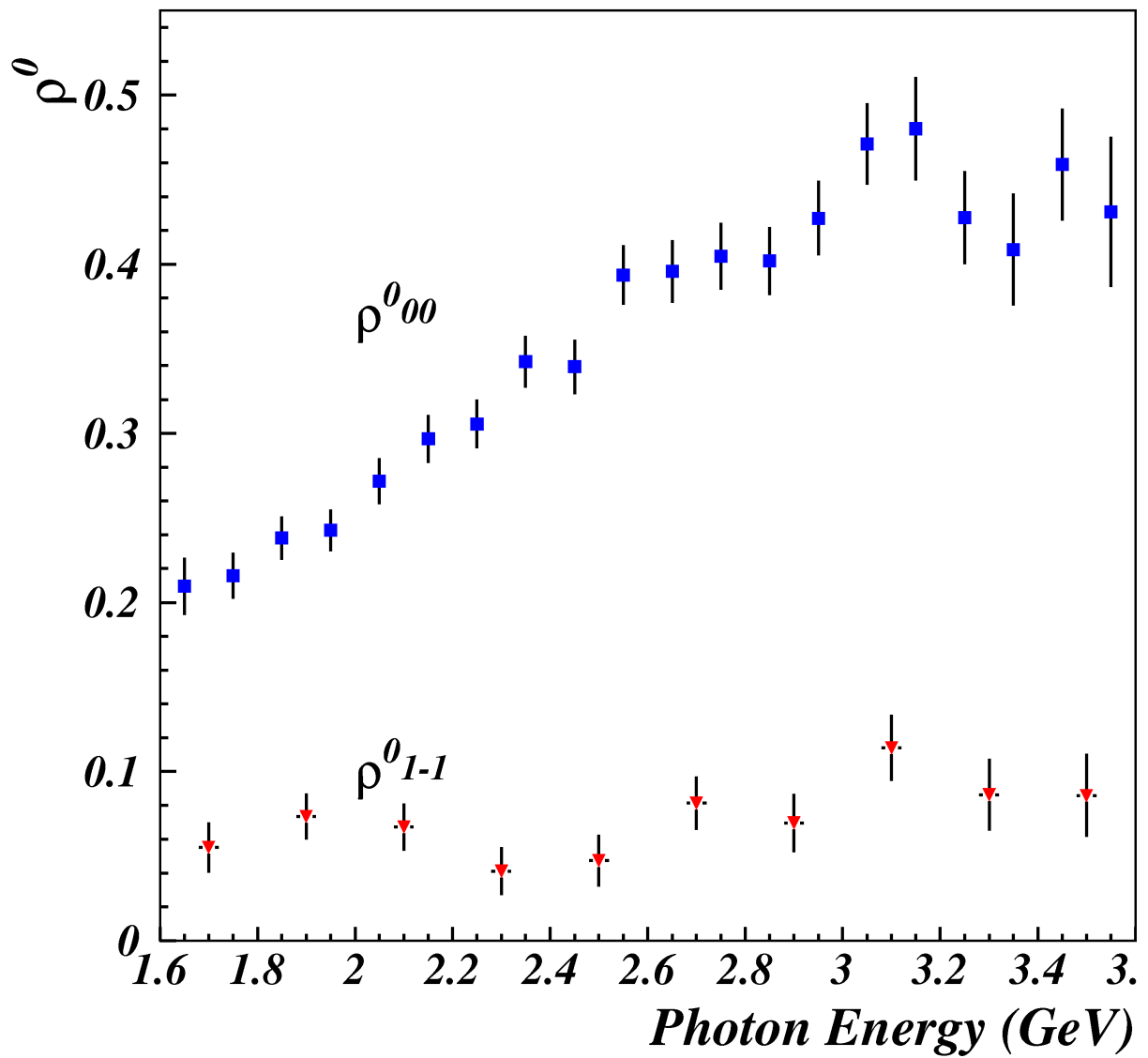


FIG. 57. Spin-density matrix element components ρ_{00}^0 (blue) and ρ_{1-1}^0 (red) for different photon beam energies in 1.6-3.6 GeV range in Gottfried-Jackson frame.

the right of the peak. The choice of 1/2 was arbitrary. The systematic uncertainty comming from this selection was estimated measuring the cross sections at 40% efficiency cut and 2cm vertex cut with a set of four various background selection coefficients : 1/2, 2/3, 3/4 and 3/5. Then the RMS of the values of the set was calculated. The systematic error due to this uncertainty is on the order of 1.3%.

- Systematic errors due to target proton vertex cut. To elimintate contamination from the aluminium walls of the targt, a 2 cm cut was applied to the initial proton vertex from the left and the right of the target (see 3.5). Uncertainty related to this cut was estimated with a set of various selections: 2 cm, 3cm, 4cm and no cut applied to both sides of the target proton vertex. The uncertainty coming from this cut was about 3.5%.
- Systematic errors due to particle detection efficiency cut.

To eliminate the bad regions of the detector with many dead wires a cut was applied to the detection efficiencies of the particles both in acceptance calculation and on actual data (see 3.4). The systematic uncertainty from this cut was calculated introducing a set of various efficiency lower limit cuts: 20%, 25%, 30%, 35%, 40% and 45%. The uncertainty is on the order of 5.7%.

Table 4.3 includes the list of the systematic uncertainties at 2.05 GeV beam energy estimated for this analysis.

Uncertainty source	Uncertainty at 2.05 GeV
Background selection cut	1.3%
Target proton vertex cut	3.5%
Particle detection efficiency	5.7%
Total	10.5%

TABLE IV. Summary of systematic errors.

4.4 SUMMARY

The 'Charged' decay channel of $\phi(1020)$ has been studied before. The results show some peak/dip structure in differential cross section in approximately 1.8-2.2 GeV photon energy range. In the 'Charged' decay mode there is a resonance $\Lambda(1520)$ which can be simultaneously produced with ϕ meson. The phase spaces of ϕ and Λ overlap in the same energy range where the local structure in differential cross sections was observed. The two coexisting resonances can interfere. This could be a possible reason for the observed behavior of the cross section. One way to check this is to measure the ϕ production cross section eliminating the coexisting $\Lambda(1520)$. Another check could be performed by studying the 'Neutral' decay mode of ϕ (there were no existing data for this channel), where there is no known strong coexisting resonance as the $\Lambda(1520)$ produced.

In this work we describe in a detail our analysis of $\phi(1020)$ meson photoproduction in its 'Neutral' decay mode $\gamma p \rightarrow \phi p \rightarrow p K_S K_l$ using data set of g11 experiment. We present preliminary results of differential cross sections versus different variables measured in this experiment. In particular, it includes results of the analysis for the ϕ decay angular distributions and spin-density matrix elements ρ_{00}^0 and ρ_{1-1}^0 in Helicity and Gottfried-Jackson frames. As we observed, in this mode the differential cross section $d\sigma/dt$ measured at $t = t_{min}$ point still shows a local peak/dip structure as it was observed in the 'Charged' mode, but the size of the peak and the slope of the t distribution is smaller for the Neutral mode in the energy range 1.7-2.4 GeV (fig. 51). The observation of enhancement in differential cross section of ϕ photoproduction in both decay modes could be caused by interference with simultaneous production of other resonance states leading to the same final state, or/and there might be also some other processes that influence the ϕ photoproduction cross section. Better understanding of the reason for the observed effect requires further studies.

There are very limited data available for the angular distributions of ϕ meson decay in the 'Charged' mode. The comparison of the existing data in photon energy range 2.0-2.4 GeV for 'Charged' mode and the current analysis results shows a good agreement for angular distributions in azimuthal angle Φ in Gottfried-Jackson frame

(fig. 55). Results of our analysis for the polar angle dependences of decay distributions in Gottfried-Jackson frame differ from the 'Charged' channel results (fig. 53). These differences have to be investigated further.

BIBLIOGRAPHY

- [1] J. Barth *et al* (SAPHIR Collaboration). *Low-energy photoproduction of Φ -mesons.* Eur. Phys. J. A **17**, 269 (2003).
- [2] T. Mibe *et al* (LEPS Collaboration). *Diffractive ϕ -meson photoproduction on the proton near threshold.* Phys. Rev. Lett. **95**, **182001** (2005).
- [3] D. P. Barber *et al.* *Forward and Wide Angle Elastic ϕ -Meson Photoproduction on Hydrogen Between 2.8 and 4.8 GeV.* Z. Phys. C **12**, 1 (1982).
- [4] J. Ballam *et al.* *Vector-Meson Production by Polarized Photons at 2.8, 4.7, and 9.3 GeV.* Phys. Rev. D **7**, 31503177 (1973).
- [5] H. J. Besch *et al.* *Photoproduction of ϕ Meson on Protons at 2.0 GeV.* Nucl Phys. B **70**, 257 (1974).
- [6] H.-J. Behrend *et al.* *Elastic and Inelastic ϕ Photoproduction.* Nucl. phys **B144**, 22-60 (1978).
- [7] E. Anciant *et al* (CLAS Collaboration). *Photoproduction of $\phi(1020)$ Meson on the Protons at Large momentum Transfer.* Phys. Rev. Lett. **85** 4682 (2000).
- [8] J. Breitweg *et al* (ZEUS Collaboration). *Measurement of diffractive photoproduction of vector mesons at large momentum transfer at HERA.* Eur. Phys. J. C **14**, 213-238 (2000).
- [9] Ya Azimov. J. Phys. G: Nucl. Part. Phys. **37** 023001 (2010) .
- [10] M. Amarian, D. Diakonov, M. Polyakov. Phys. Rev. D **78** 074003 (2008).
- [11] G. Gavalian.
- [12] A.I. Titov, T.-S.H. Lee, H. Toki, and O. Streltsova, Phys. Rev. C **60**, 035205 (1999).
- [13] A.I. Titov and T.-S.H. Lee, Phys. Rev. C **67**, 065205 (2003).

- [14] S. Okubo, Phys. Lett. **5**, 165 (1963); G. Zweig,CERN Report No. 8182/TH 401 and 8419/TH 412, 1964 (unpublished); J. Iizuka, Prog. Theor. Phys. Supp. **37/38**, 21 (1966); G. Alexander, H.J. Lipkin, and P. Scheck, Phys. Rev. Lett. **17**, 412 (1966).
- [15] R.A. Williams, Phys. Rev. C **57**, 223 (1998).
- [16] K. Schilling, K. Seyboth and G. Wolf, Nucl. Phys. **B15**, 397 (1970).
- [17] D.G. Cassel *et al.*, Phys. Rev. D **24**, 2787 (1981).
- [18] D.W.G.S. Leith, in *Electromagnetic Interactions of Hadrons*, edited by A. Donnachie and G. Shaw (Plenum Press, New York, 1978), Vol. 1, p. 345.
- [19] A. Donnachie and P.V. Landshoff, Phys. Lett. B **185**, 403 (1987); Nucl. Phys. **B244**, 322 (1984); *ibid.* **B267**, 690 (1986).
- [20] H. Suganuma, S. Sasaki, and H. Toki, Nucl. Phys. **B435**, 207 (1995).
- [21] J.-M. Laget and R. Mendez-Galain, Nucl. Phys. **B581**, 397 (1995).
- [22] M. Diehl, Eur. Phys. J. C6, 503 (1999).
- [23] F.E. Low, Phys. Rev. D **12**, 163 (1975); S. Nussinov, Phys. Rev. Lett. **34**, 1286 (1975).
- [24] J.R. Cudel, A. Donnachie and P.V. Landshoff, Nucl. Phys. **B322**, 55 (1989).
- [25] P.V. Landshoff and O. Nachtmann, Z. Phys. C **35**, 405 (1987).
- [26] A.I. Titov, Y. Oh S.N. Yang, and T. Morii, Phys. Rev. C **58**, 2429 (1998); Nucl. Phys. **A684**, 354 (2001).
- [27] Q. Zhao, J.P. Didalez, M. Guidal and E. Hourany, Nucl. Phys. A **684**, 351 (2001).
- [28] J.-M. Laget, Phys. Lett. B **489**, 3133 (2000).
- [29] N.I. Kochelev and V. Vento, Phys. Lett. B **515**, 375 (2001); hep-hp/0112292.
- [30] B. Friman and M. Soyeur, Nucl. Phys. **A600**, 477 (1996).

- [31] A.I. Titov, T.-S.H. Lee, Phys. Rev. C **66**, 015204 (2002).
- [32] T. Nakano and H. Toki, in *Proceedings of the International Workshop on Existing Physics and New Accelerator Facilities*, SPring-8, Hyogo, 1997 (World Scientific Singapore, 1998), p.48.
- [33] K. Hagiwara *et al.* [Particle Data Group Collabpration], Phys. Rev. D **A66**, 010001 (2002).
- [34] U.-G. Meissner, V. Mull, J. Speth, and J.W. Van Orden, Phys. Lett. B **408**, 381 (1997).
- [35] H.J. Besch, G. Hartmann, R. Kose, F. Krautschneider, W. Paul, and U. Trinks, Nucl. Phys. B**70**, 257 (1974).
- [36] The CLAS Collaboration, E. Anciant *et al.*, Phys. Rev. Lett. **85**, 4682 (2000).
- [37] M. Battaglieri *et al.* *Study of Pentaquark States in Photoproduction off Protons*. CLAS Experiment Proposal E-04-017.
- [38] David J. Tedeschi *et al*, Phi Meson Photoproduction with CLAS, CLAS Analysis Note (under review) (2008).
- [39] M. Ungaro, R. De Vita, L. Elouadrhiri, g11 data processing, CLAS-NOTE 2005-14.
- [40] V. Kubarovskiy.
- [41] E. Pasyuk, *The CLAS ELOSS Package*. Software available via the CLAS CVS repository under clas/packages/utilities/eloss.
- [42] W.-M. Yao *et al.* Review of Particle Physics. J. Phys. G **33**, 1 (2006).
- [43] S. Stepanyan. *Evidence for an Exotic Pentaquark Baryon State $\Theta^+(1530)$, in the $\gamma d \rightarrow pK^+K^-n$ reaction*. CLAS Analysis Note 2003-105.
- [44] M. Williams, Ph.D. Thesis, *Measurement of Differential Cross Sections and Spin Density Matrix Elements along with a Partial Wave Analysis for $\gamma p \rightarrow p\omega$ using CLAS at Jefferson Lab*, Carnegie Melon University (2007).

- [45] Z.A. Krahn, Ph.D Thesis, *Photoproduction of η and η' Mesons Using CLAS at JLAB*, Carnegie Melon University (2007).
- [46] R. Bradford and R.A. Schumacher. *Liquid Hydrogen Density in the G1C CLAS Cryotarget*. CLAS Note 2002-003.
- [47] J. Ball and E. pasyuk. *Photon Flux Determination Through Sampling of 'out-of-time' Hits with the Hall B Photon Tagger*. CLAS Note 2005-002.
- [48] R. De Vita, M. Battaglieri. *Analysis of ω production at 90° degrees in the g11 data set*. CLAS Analysis Note 2009-105 (2010).
- [49] R. De Vita. *Private Communication*.
- [50] /mss/clas/g11a/production/pass1/v1/trip.